Catarina Maria Martins Ferreira Couto de Sousa

Licenciatura em Ciências de Engenharia Biomédica

Electrohysterogram Signal Component Cataloging with Spectral and Time-Frequency Methods

Dissertation for a Master's Degree in Biomedical Engineering

Supervisor: Arnaldo Batista, FCT-UNL
Co-Supervisor: Fátima Serrano, FCM-UNL

FACULDADE DE CIÊNCIAS E TECNOLOGIA
UNIVERSIDADE NOVA DE LISBOA

October 2015

Copyright

Acknowledgments

To professor Arnaldo Batista, who not only was a great scientific advisor, but also a friend, with a boundless enthusiasm and dedication to this project, which I hope it carries on with great success. For him, a very special Thank You, because without his valuable assistance it would have been much more difficult.

To my co-supervisor Dr. Fatima Serrano not only for all the help provided with the tocograms but also for her contribution to this project: for being the interface between us and the Maternidade Alfredo da Costa, for all the helpful advices, remarks and for answering every medical doubt that arose.

To Dr. Graça Pinto and Dr. Neuza Mendes who were always available to answer every medical doubt, as well as for being part of the tocogram annotation process.

To all the doctors of Maternidade Alfredo da Costa who took their time to annotate the Tocogram, which was a valuable tool to this project: Dr. Fatima Serrano, Dr. Graça Pinto, Dr. Neuza Mendes, Dr. Sara Valadares and Dr. Rita Torres.

To professor Manuel Ortigueira for all his wise advices, when difficulties were encountered.

To Ásgeir Alexandersson and Brynjar Karlsson developers of the 16-electrode Electrohysterogram Database, which contains the signals used in this thesis.

To my parents, Luis Sousa and Teresa Sousa, my brother, Pedro Sousa, and grandmother Maria José Ferreira, for all the friendship and encouragement throughout this time.

To all my colleages and friends, especially Liliana Ribeiro and Sara Matos for all the friendship and great moments spent together.

Finally, to all students who have contributed to the development of the Uterine Explorer: Shirin Najdi, Daniela Godinho and also Catarina Hilario, Landislau Moreira, who developed the energy estimation modulus and Sara Russo, not only for her help in the referred modulus but also for providing the artifacts table (table 3.1, Chapter 3).

Abstract

The Electrohysterogram (EHG) is a new instrument for pregnancy monitoring. It measures the uterine muscle electrical signal, which is closely related with uterine contractions. The EHG is described as a viable alternative and a more precise instrument than the currently most widely used method for the description of uterine contractions: the external tocogram. The EHG has also been indicated as a promising tool in the assessment of preterm delivery risk. This work intends to contribute towards the EHG characterization through the inventory of its components which are:

- Contractions;
- Labor contractions;
- Alvarez waves;
- Fetal movements;
- Long Duration Low Frequency Waves;

The instruments used for cataloging were: Spectral Analysis, parametric and non-parametric, energy estimators, time-frequency methods and the tocogram annotated by expert physicians. The EHG and respective tocograms were obtained from the Icelandic 16-electrode Electrohysterogram Database. 288 components were classified. There is not a component database of this type available for consultation. The spectral analysis module and power estimation was added to Uterine Explorer, an EHG analysis software developed in FCT-UNL.

The importance of this component database is related to the need to improve the understanding of the EHG which is a relatively complex signal, as well as contributing towards the detection of preterm birth.

Preterm birth accounts for 10% of all births and is one of the most relevant obstetric conditions. Despite the technological and scientific advances in perinatal medicine, in developed countries, prematurity is the major cause of neonatal death. Although various risk factors such as previous preterm births, infection, uterine malformations, multiple gestation and short uterine cervix in second trimester, have been associated with this condition, its etiology remains unknown [1][2][3].

Keywords: Electrohysterogram; *Uterine Explorer*; EHG components database; Preterm birth

Resumo

O Electrohisterograma (EHG) é um instrumento novo para a monitorização da gravidez. Trata-se de um sinal elétrico com origem no músculo uterino que está intimamente associado às contrações uterinas, tendo sido descrito como uma alternativa viável e mais precisa ao instrumento atualmente mais usado na descrição das contrações uterinas: o tocograma. O EHG tem também sido indicado como um instrumento promissor na avaliação do risco de parto pré-termo. Neste trabalho, pretende-se contribuir para a caracterização do EHG através da inventariação das suas componentes que são:

- Contrações;
- Contrações de Parto;
- Ondas Alvarez;
- Movimentos Fetais;
- Ondas de baixa frequência e longa duração;

Os instrumentos de catalogação usados neste trabalho são: Analise Espetral paramétrica e não paramétrica, estimadores de Energia, métodos Tempo-Frequência e análise do tocograma anotado por especialistas. O EHG e respetivos tocogramas foram obtidos da *Icelandic 16-electrode Electrohysterogram Database*. Foram inventariadas 288 componentes. Não existe uma base de dados de componentes deste tipo disponível para consulta. O módulo de análise espetral e de estimação de energia foi adicionado ao *Uterine Explorer, um software* de análise do EHG desenvolvido na FCT-UNL.

A importância desta base de dados de componentes do EHG está relacionada com a necessidade de melhorar o entendimento do EHG que é um sinal relativamente complexo, bem como contribuir para a deteção do parto pré-termo.

O parto pré-termo, correspondente a uma taxa de 10% de todos os nascimentos, é uma das condições obstétricas mais relevantes. Apesar dos avanços tecnológicos e científicos na medicina perinatal, nos países desenvolvidos, a prematuridade é a principal causa de morte neonatal. Embora vários fatores de risco, tais como partos prematuros anteriores, infeções, malformações uterinas, gestação múltipla e colo uterino curto no segundo trimestre, têm sido associados a esta condição, a sua etiologia permanece desconhecida [1][2][3].

Palavras-Chave: Electrohisterograma; *Uterine Explorer*; Base de dados de componentes do EHG; Parto pré-termo;

Contents

List of Figures

List of Tables

Acronyms

EHG	Electrohysterogram
TOCO	External Tocogram
IUPC	Intrauterine Pressure Catheter
CHR	Corticotripin Releasing Hormone
ICLCs	Interstitial Cajal-like Cells
NO	Nitric Oxide
LAHF	*Low Amplitude High Frequency*
LDBF	*Long Duration Low Frequency*
FWL	Fast Wave Low
FWH	Fast Wave High
ECG	Electrocardiogram
EMG	Electromyogram
HR	Heart Rate
SNR	Signal to Noise Ratio
STFT	Short-Time Fourier Transform
FT	Fourier Transform
WT	Wavelet Transform
CWT	Continuous Wavelet Transform
DWT	Discrete Wavelet Transform
WPD	Wavelet Packet Decomposition
WVD	Wigner-Ville Distribution
RID	Reduced Interference Distributions
CWD	Choi-Williams Distribution
ED	Exponential Distribution
DFT	Discrete Fourier Transform
FFT	Fast Fourier Transform
PSD	Power Spectrum Density
WOSA	Welch Overlapped Segmented Average
ENBW	Effective Noise-Equivalent Bandwidth
PS	Power Spectrum
LSD	Linear Spectral Density
LS	Linear Spectra

AR	Autoregressive
MA	Moving Average
ARMA	Autoregressive Moving Average
RMS	Root Mean Square
TE	Teager Energy
PAPR	Peak-to-Average Power Ratio
MAC	Maternidade Alfredo da Costa
BUA	Basal Uterine Activity
UI	Uterine Irritability
LAC	Low Amplitude Contraction
HAC	High Amplitude Contraction
FM	Fetal Movement
AIC	Akaike's Information Criterion
FPE	Final Prediction Error
ELC	Early Labor Contractions
LLC	Late Labor Contractions

Chapter 1

Introduction

Preterm birth occurs when the baby is born with less than 37 weeks of gestation, remaining a major problem in obstetrics. Children born before term present a high risk of mortality as well as health problems, such as hearing and visual problems, learning disabilities, chronic lung disease and cerebral palsy [4][5].

About 10% of newborns worldwide are preterm infants, which is about 15 million newborns each year. It is a global problem as the rates for preterm infants are 12% in lower income countries and 9% in higher income countries [5].

Between 2001 and 2009 the rate of preterm birth in Portugal suffered a relative increase of 54.2%. In the period 2004-2009, the highest value of this indicator was recorded in 2007 (9.1 %), slightly decreasing from that year [6].

According to Roberts et al. [7] certain factors such as prior preterm delivery, multifetal gestation and significant uterine and cervical anomalies are high risk factors that place subjects in risk of preterm delivery. Another important factor is uterine irritability, usually painful uterine contractions, frequent, without any demonstrable cervical change in effacement or dilatation. [8]

To lower the preterm rate the patients determined to be at risk for early delivery should be monitored. Thus, necessary treatment can be administrated in women with true labor, and unnecessary interventions in women who are simply having pre term contractions, but are not in true labor, is avoided [9].

Nowadays, the most used device for pregnancy monitoring is the external tocogram, noninvasive technique, which measures the mechanical contractions with a transducer attached to the subject's abdomen. [10] However, the only information provided by the tocogram which can be considered reliable is the number of detected contractions. Thus, it is useful mainly to control the labor progress. It is also influenced by parameters such as body mass index, artifacts (respiratory or maternal movements) [11]. Another technique, more reliable, is the internal tocogram, also known as intrauterine pressure catheter (IUPC) which provides more reliable information on uterine contractions. However, it is invasive and therefore excluded as a routine diagnostic tool [12].

More recently, the Electrohysterogram (EHG) is the noninvasive measurement technique which provides information on uterine contraction during pregnancy and labor by measuring the electrical activity responsible for the mechanical response, obtained with the tocogram. Proving to be a more accurate method than internal and external tocography as they are only limited to the mechanical attributes of the uterine contraction activity, whereas this technique provides more complete information, describing also electrophysiological properties of the uterus [12].

Currently, the EHG is mostly used as a research tool. However, there is EHG equipment approved by the American Food and Drug administration such as the EUM-100 Pro, OB-Tools, the latest system from Monica, the Monica AN24 and finally the SureCALL® Labor Monitor® from SureCALL®, thus allowing for these devices to be used in hospitals and clinics in the United States of America. However, its presence in the clinical settings is still very limited, since it is still considered a research tool. These systems are supposed to provide alternative information to the tocogram. The basic idea is to obtain uterine contraction information via the EHG. It is claimed that these new methods can reduce false positive and negative rate regarding uterine contractions and pregnancy monitoring for labor, thus leading to better pregnancy surveillance and medical decision. However, these devices do not take in account that the EHG is made up different components with different clinical significances.

This work has the purpose of obtaining the following components from the EHG to build up a database:

- Alvarez waves, also known as uterine irritability.
- Long Duration Low Frequency (LDBF) waves.
- Fetal Movements.
- Labor Contractions
- Braxton-Hicks Contractions.

As such, the components will be isolated and characterized in both time and frequency domains. As well as other parameters such as Root Mean Square, Time-Averaged Power, Teager operator and Crest Factor. A component database will therefore be constructed to contribute for the development for preterm birth detection algorithms. The motivation for this work has been the lack of such database, despite the general consensus in that the EHG components are the master players for any preterm risk evaluation algorithm. It is out of the scope of this work the development of such algorithm or a statistical study. The idea is to provide the user community with an EHG component database that, besides having the separated events, also has their time and frequency characterization, which are features that are commonly used for this purpose. A great deal of the time spent in this work has been on the code development of the spectral and estimators, besides the database construction.

All the generated code has been included in the *Uterine Explorer* software tool which has a modular architecture. This tool has been developed in the FCT-UNL since 2013. The *Uterine Explorer* was lacking a spectral analysis modulus and this has been setup with this work, as well as extensive code debugging and testing.

1.1 State Of The Art

In the 50's the following uterine contractibility events: Alvarez waves, Braxton Hicks and Contractions, were detected by methods of intrauterine pressure measurement.

Alvarez and Caldeyro [13] studied uterine contractility in more than 180 women by inserting into the bladder a catheter connected to a water nanometer, since the presence of fluid in the bladder makes possible the recording of variations in abdominal pressure. The authors identified two kinds of contractions during pregnancy: rhythmical contractions of low intensity, later called Alvarez waves, and nonrhythmical contractions of higher intensity, the Braxton Hicks.

Csapo and Sauvage [14] developed clinical trials in a total of 96 pregnant subjects. A recording catheter with a microballon attached was inserted into the space between the fetal membranes and the uterine wall. The intrauterine pressure tracings were analyzed: high frequency low amplitude, irregular shape cycles interrupted by low frequency, high amplitude cycles (Braxton-Hicks contractions) were found, in first stage labor, smooth and quadratic contractions took place.

The first EHG signal ever reported in the literature was measured in 1931 as the deflection of a galvanometric needle during a uterine contraction [9][15]. Later on, Larks [16] acquired the EHG signal by placing electrodes on the uterus of 293 subjects in labor and studied its waveforms.

As depicted on the chronology on Figure 1.1, in the 90's and 00's some work was done by some authors towards the identification of the uterine events on the EHG.

Marque et al. [17] identified contractions, Alvarez and fetal movements on the EHG signal of 17 women, 9 of whom were hospitalized for premature delivery treats, marking Alvarez and contractions. The remaining 8 subjects identified the fetal movements. The events were marked by subjects whose event identification appeared reliable in view of the prior knowledge of the signal and uterine physiology.

Later, the same author [18] collected the EHG signal from 83 subjects and identified the following events: contractions and fetal movements. The events were marked as contraction when the subject felt a contraction and fetal movement, when the subject felt a fetus motion.

Khalil et al. [19][20][21] classified the events present on the EHG into the following categories: Fetus motions, Alvarez waves, uterine contractions and Long Duration Low Frequency waves using an algorithm for detection-classification-labelling based on the Dynamic

Cumulative Sum, Neural Networks and Wavelet Packet Decomposition which resulted in more than 80% of the events well detected and classified. An example, of this wave classification can be seen on Figure 1.2 and Figure 1.3. In these papers it is mentioned that an event database was constructed by experts, however it is not disclosed the criteria and parameters used by the experts to classify the EHG components. Moreover, this is the only report regarding the existence of a component database. This database is not currently available in the public domain.

As such, the aim of this thesis is to characterize the many features of the EHG signal, disclosing them in a dictionary of EHG events.

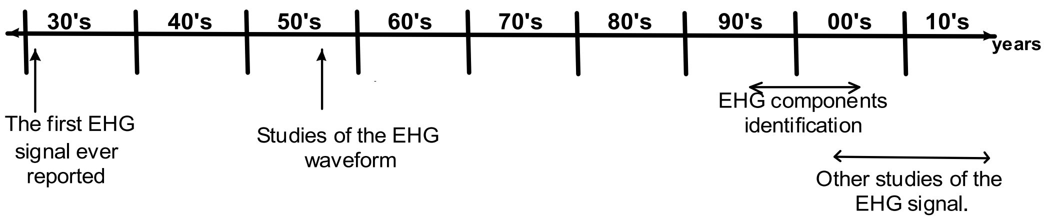

Figure 1.1 - Cronology regarding the EHG signal study

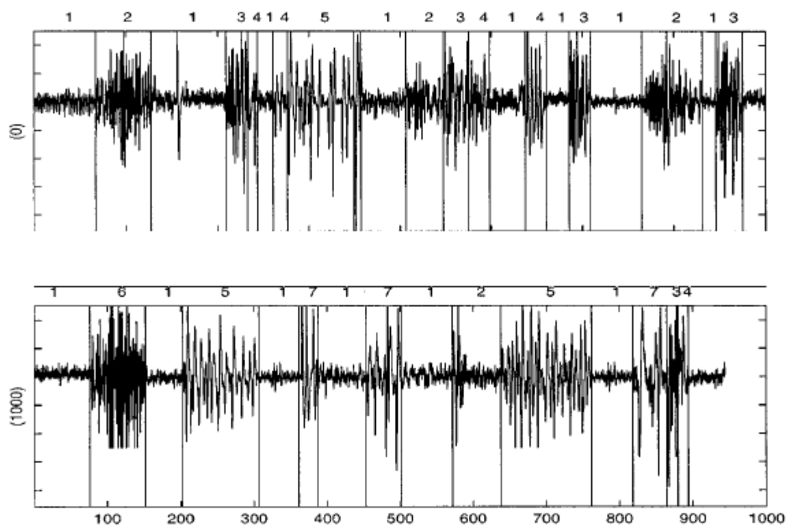

Figure 1.2 - First automatic detection and classification in the Electrohysterogram. 1: Backgroung activity, 2 and 6: contractions, 4 and 7: fetus motions, 5: LDBF waves and 3: Alvarez waves [from.[20]]

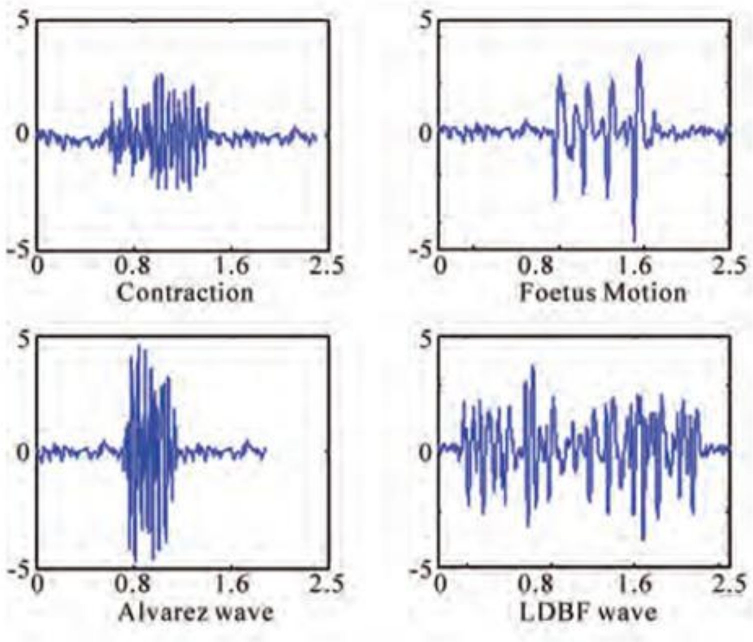

Figure 1.3 - Samples of various events appearing in the uterine EMG recordings. X axis: minutes, Y axis Amplitude scale in arbitrary units [from.[22]]

1.2 Thesis Organization

The outline of the thesis is as follows:

- **Chapter 1** - Brief introduction of the theme, the work already done, state of the art, as well as the thesis structure.

- **Chapter 2** – Brief description of the anatomical and physiological aspects of pregnancy and birth.

- **Chapter 3** - More detailed description of the events to be identified in the Electrohysterogram. It also contains a description about the Electrohysterogram and its comparison with the currently used methods for uterine contraction monitoring, as well as its signal and the database where it was extracted.

- **Chapter 4** - Describes the theoretical aspects of each Time-Frequency Analysis technique.

- **Chapter 5** - Theoretical basis of both parametric and nonparametric methods of Spectral Analysis, as well as the following tools used to characterize the EHG signal: Energy, Power, Root Mean Square, Teager operator and Crest Factor.

- **Chapter 6** - Methodology.

- **Chapter 7** - Results.

- **Chapter 8** – Conclusions, achievements and guidelines for future work.

Chapter 2

Theoretical Basis for Uterine Electrical and Physiological Activity

The uterus is an organ of the female reproductive system responsible for the development of the embryo and fetus during pregnancy, until labor when the fetus is expelled to the outside world. Uterine contractions are triggered by electrical activity and are present throughout pregnancy, especially upon parturition, when they are more intense.

As such, in this chapter it will be discussed the anatomical and physiological aspects of the pregnant uterus. More precisely, a brief introduction about the uterine anatomy, followed by a more detailed explanation about physiological aspects of the pregnancy contractions and the steps of parturition that lead to a successfully expel of the fetus.

2.1 Uterine Anatomy

The uterus is a hollow, muscular organ that is shaped like an inverted pear. It is located above the vagina, above and behind the bladder and in front of the rectum. It is about 7 cm long and 5 cm wide (at the widest point).

The uterus is divided in three parts: the fundus and the body, which are separated by the entrance of the two Fallopian tubes, and finally the cervix (Figure 2.1) [23][24].

The uterine wall is composed of three distinct layers:

- **Endometrium**, the inner layer, which lines the lumem of the organ. This layer thickens in preparation for the implantation of a fertilized egg upon its arrival in the uterus.

- An intermediate layer, the **myometrium**, is the thickest layer of the uterus. It is composed of longitudinal and circular layers of smooth muscle. During pregnancy the myometrium increases both by hypertrophy of the existing cells and by multiplication of the cell number. Upon parturition, coordinated contractions of the smooth muscle cells in the myometrium are responsible to expel the fetus out of the uterus. After delivery, the myometrium contracts to expel the placenta.

- Finally an external layer, the **perimetrium**, is a multilayered membrane that lines the abdominal cavity and supports and covers the organs [9].

Figure 2.1 - Anatomic structure of the non-pregnant uterus [from.[23]]

The uterus grows dramatically during pregnancy as it enlarges by a factor of four to five, also increasing in weight from about 50 g at the beginning to 1kg at term. (Figure 2.2) [23][25][26]

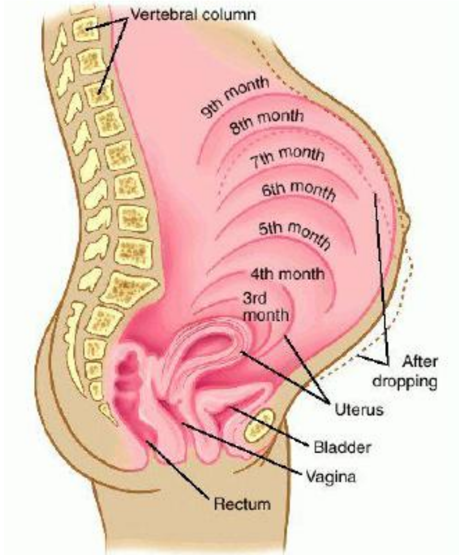

Figure 2.2 - Development of the uterus during pregnancy [from.[27]]

2.2 Uterine Physiology

2.2.1 Cell Excitability

The uterus is mostly a quiescent organ during most stages of pregnancy until labor when the fetus is expelled to the outside world [25][28].

Contractions lead to a decrease of the uterus volume and an increased pressure on the fetus, as depicted in the figure bellow (Figure 2.3), where it can be seen the direction of the contraction, towards the fetus.

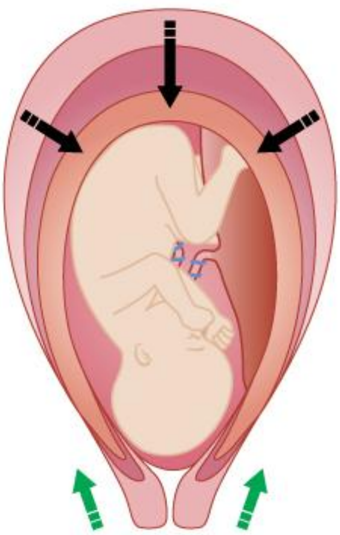

Figure 2.3 - Contraction direction towards the interior of the uterus augmenting the uterus pressure [from.[29]]

Those contractions are triggered by electrical activity in the form of action potentials whose duration and frequency determine the amplitude and strength of the contractile force of uterus smooth muscle cells.

The uterus smooth muscle cells are responsible for contractions, although intrinsic control (mechano-receptor) and extrinsic (sympathetic and parasympathetic system) are present. Also, the organization of the uterine muscle is an important factor for its contractility. [9]

As such, the uterine smooth muscle cells, myocites, are densely packed within a bundle. Bundles are contiguous within a fasciculus, forming myocytes via communicating bridges (Figure 2.4) [30].

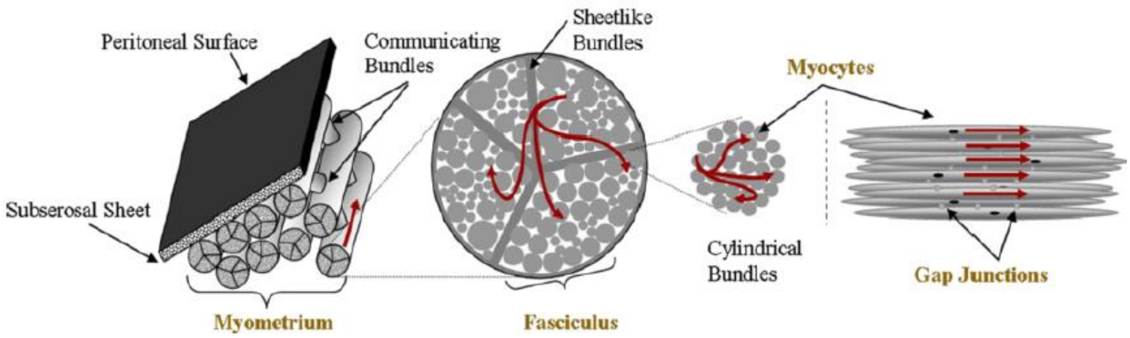

Figure 2.4 - Diagram of microanatomy of pregnant human myometrium. Red line represent current flows [from.[30]]

The contractile mechanism of myometrial cells involves the sliding of actin and myosin filaments over each other. The relationship between this mechanical effect (actin and myosin interaction) and electrical excitation (appearance of action potential) is called excitation-contraction coupling [23][31]. Thus, myosin heads tilt ad drag the actin filaments along a small distance (10-12 nm), a process called crossbridge cycling, which can be seen in Figure 2.5 [23].

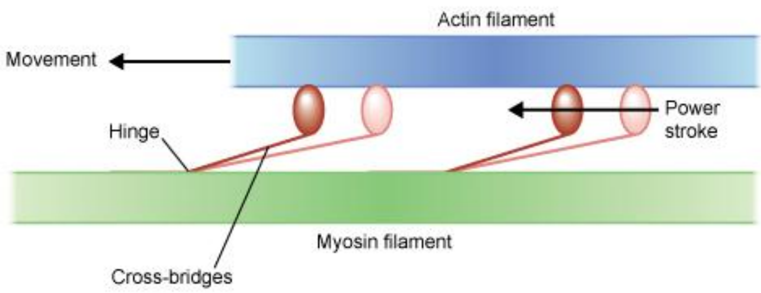

Figure 2.5 - Crossbridge cycling [from.[29]]

So far, the efforts to fully understand the origin of uterine contractions remain inconclusive [28].

The sequence of contraction and relaxation of the myometrium results from the cyclic depolarization and repolarization of the muscle-cell membranes [25].

As such, the action potential, Figure 2.6, is related to abrupt variations of cell permeability to calcium, potassium and chloride ions. When their concentration change, the cell membrane becomes hyperpolarized (resting potential more negative) or depolarized (resting potential more positive). As soon as the resting potential reaches a threshold, action potentials are generated and thus a contraction. It is difficult to have an absolute value of resting potential of the smooth muscle cells because it fluctuates in a sinusoidal manner, in pregnant women the resting potential varies from -65 to -80mV and the action potential lasts for about 100 ms [31].

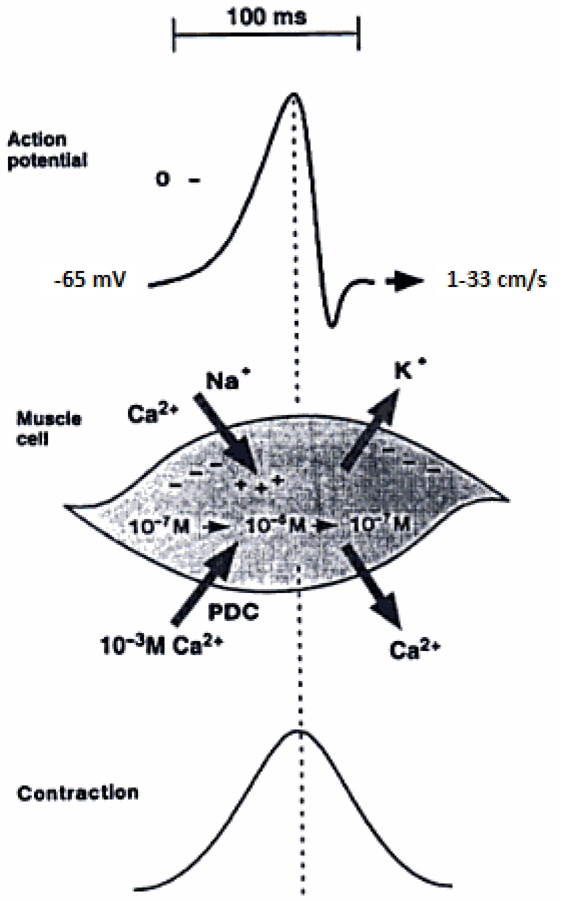

Figure 2.6 - Diagram to show the changes in membrane potential (top), influx and efflux of ions (middle) and mechanical event (contraction, bottom) during passage of an action potential over a single myometrial cell. (PDC = potential dependent chanel) [from.[32]]

2.2.2 Propagation of the Uterine Electrical Activity

Uterine activity propagates in all directions but ultimately spreads from the fundus towards the cervix as electrical activity moves through the gap junctions (Figure 2.7). The muscle contraction is intense in the fundus, weak in the lower uterine segment and essentially absent in the cervix.

The placenta seems to alter the direction of the activity propagation. In fact, there is an inhibition of the propagation from the cells from the non-placental region to the placental ones, but not the reverse [9].

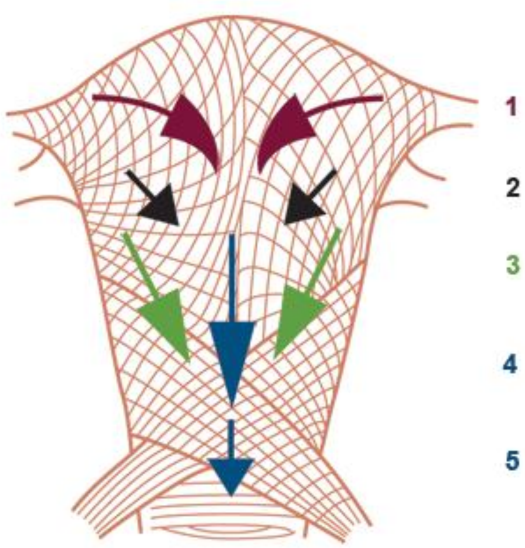

Figure 2.7 - Propagation of contractions in the uterine muscle (from 1 to 5) [from.[33]]

Gap Junctions, Figure 2.8, are channels of low electrical resistance providing intracellular communication by allowing ions, metabolites and second messengers to travel from one cell to another. The action potentials are thus propagated between cells throughout gap junctions. Also, they play an important role in the contractility of myometric muscle during labor [23][25][28][31].

As shown in Figure 2.8, increased gap junctions interactions results in improved propagation of electrical impulses, increased conduction velocity and coordinated contraction of the myometrium.

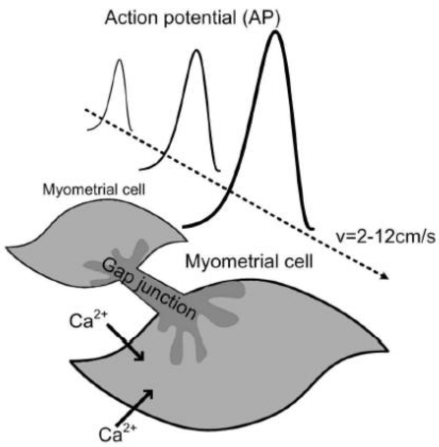

Figure 2.8 - Schematic representation of the cell-to-cell electrical coupling due to the formation of gap junctions [from. [23]]

The number and size of gap junctions increase during gestation, especially in late pregnancy or during labor when they reach approximately 1000 per cell. In a non-pregnant myometrium it is very rare or even impossible to find gap junctions as they decline 24 hours after the delivery [23].

Throughout most of the pregnancy, and in all species studied, these cell-to-cell channels or contacts are few, indicating poor coupling and decrease electrical conductance, which favors quiescence of the muscle and the maintenance of pregnancy. At term, however, the number of cell junctions increases and they form an electrical syncytium required for effective contractions [25].

The formation of gap junctions is related to the secretion of hormones. The estrogen, secreted towards the end of pregnancy, stimulates the synthesis of connexins, proteins that can be found in cell membranes, align to create Gap Junctions.

As seen in Figure 2.9, each opening contains multiple channels; each channel consists of six connexins in the adjacent cell, aligned symmetrically in a hexametric structure.

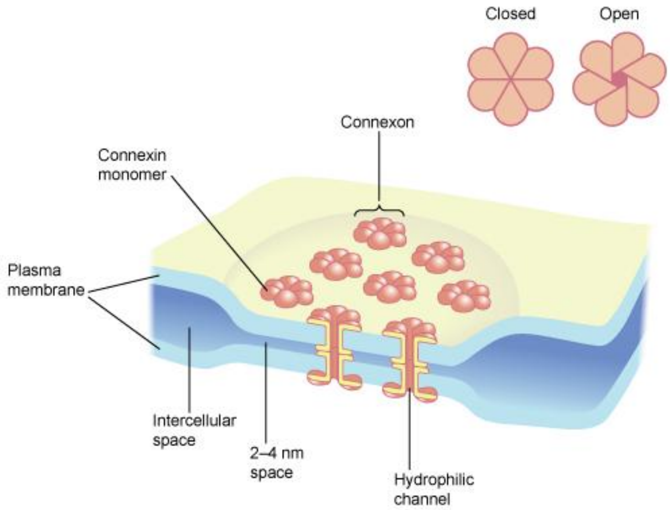

Figure 2.9 – Gap junctions formation: connexins alligned in a hexametric structure, forming the gap junctions with an adjacent cell [from.[34]]

In uterus it is believed that coupling between myocytes and connective tissues are responsible for the initiation of uterine spontaneous oscillations [23][28].

At the beginning of pregnancy progesterone secreted inhibits the uterine contractions (Figure 2.10).

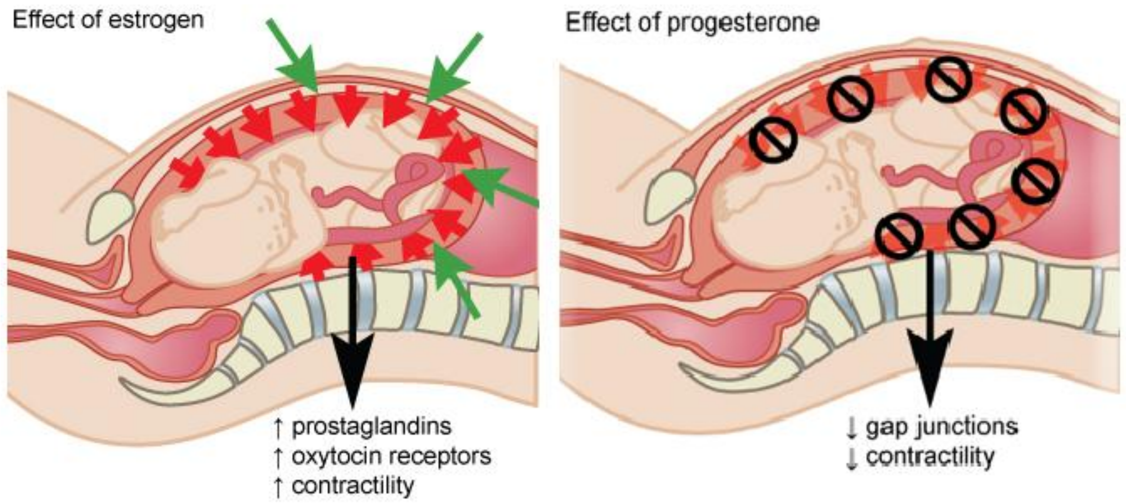

Figure 2.10 - Effect of progesterone and estrogen in uterine contractility: Estrogen secretion results in an increase in gap junctions and thus contractility; Progesterone inhibits uterine contractions, with a decrease in the gap junctions number[from.[34][35]]

Towards the end the secretion of estrogen overcomes the effect of progesterone, resulting in dramatically increase in the number of the gap junctions.

This is also thought to be due to another hormone – corticotripin releasing hormone (CRH), which functions as a clock establishing the time of birth. Women who have higher levels of CRH earlier in pregnancy are more likely to deliver prematurely [28].

What causes uterine contractions? More precisely, what causes the action potentials? That question still waits to be answered. Although, there are some theories:

- The first of all stated that myometrial cells can either be pacemaker or pacefollower. Pacemaker cells are capable of generating action potentials, as pacefollower are excited by the action potentials generated from a neighboring cell [31]. However, pacemaker cells have not been found in the uterus as myometrial cells do not oscillate spontaneously, when taken in isolation, a characteristic behavior of pacemaker cells [28].

- Another theory, states that spontaneous electrical behavior is an inherent property of uterine smooth muscles. Thus, uterine tissue is known to contain an abundance of electrically passive cells, such as Interstitial Cajal-like Cells (ICLCs), which are similar to Cajal Cells, pacemaker cells in the heart. As such it is believed that they may inhibit electrical activity in the uterus. It is known that uterine contractions propagate from the fundus towards the cervix during active labor, which suggests that although there may be not a specific type of individual pacemaker cells, there may be general pacemaker regions later in gestation [28][36].

- A more recent theory concerns the gap junctions, which increase dramatically close to term, resulting in stronger inter-cellular coupling. Plus, it has been observed that a chemical disruption of gap junctions immediately inhibits the oscillatory uterine contractions. Thus, it has been argued that this increased coupling can lead to spontaneous activity.

- Also, as close contact between ICLCs and smooth cells has been observed, another paradigm states that spontaneous oscillatory behavior could be initiated by the strong increase in coupling between non-oscillatory electrically active and passive cells of a pregnant uterus shortly before delivery [37].

2.2.3 Delivery and Interrelationship between the Uterus and Cervix

During delivery, the successfully expel of the fetus requires a coherent contraction of 100 billion smooth muscle cells [28].

The uterus contractions are strong enough to overcome any passive (or active) resistance to dilatation and delivery that the cervix may offer. This dynamical balance between the uterine and any cervical forces is critical in preterm labor, where the uterus is not well developed and consequently the labor is less efficient [38].

- Delivery starts with the onset of coordinated **uterine contractions**.

- There is a rupture of the **fetal membrane**.

- In labor the **cervix** starts to stretch or thin (efface) and open (dilate) in order to provide passage for the baby via the birth canal (vagina). As shown in the figure 2.11 the baby's head moves towards the pelvis, the head pushes against the cervix and causes the cervix to relax and efface. Throughout a woman's pregnancy, the cervix is closed and protected by a block of mucus. As soon as the cervix is effaced, the mucus block loosens and flows out of the vagina [36].

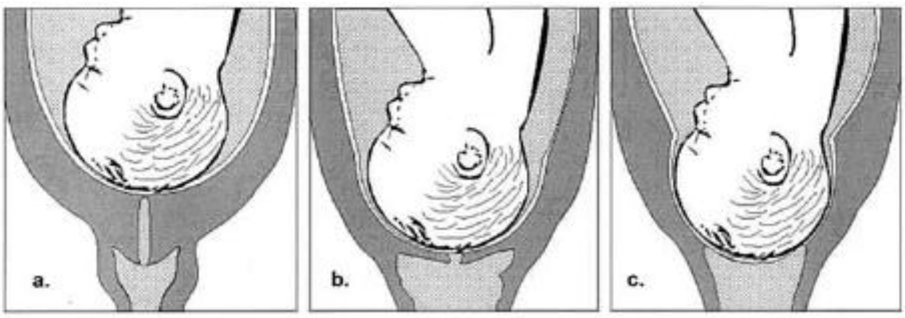

Figure 2.11 - Cervical ripening. A) Throughout pregnancy the cervix is rigid and closed. B) Beginning in midpregnancy the cervix softens resulting in a progressive shortening and gradual effacement nearing term, leading to cervical dilatation (C) [from.[2]]

Chapter 3

Pregnancy Monitoring

As depicted on Figure 3.1, there are sub-categories of birth, based on gestational age:

- **Extremely preterm (22-25 weeks)** - Children born on that period have a higher risk of mortality and morbidity. At 22 weeks of gestation the survival rate is the lowest, 0-10%, increasing from that point on. After the 24 weeks labor repressants, Tocolytics may be administrated, to avoid preterm labor.

- **Very preterm (26-32 weeks)** – Children born on that period have a higher survival rate (superior to 80%). Tocolytics, may be administrated

- **Late preterm (33-37 weeks)** – Children have a good chance of survival (higher than 90%). Tocolytics are not administrated after the 34 weeks as the risk of complication of tocolytics therapy may outweigh the benefits of prolonging the therapy for a short period of time. The prolonged use of tocolytics may increase the maternal-fetal risk without offering a clear benefit [39].

- **Term (38-42 weeks) –** Pregnancies last around 40 weeks from the last menstrual period [40]. From the 38 week, pregnancy is considered full-term.

- **Post-Term (43-46 weeks)** – Post-Term births have risks for both mother and fetus, including fetal malnutrition. After the 42nd week of gestation, the placenta, which supplies the baby with nutrients and oxygen from the mother, starts aging and will eventually fail. Furthermore, if the fetus passes its fecal matter, which normally only happens after birth, and breaths in it, the fetus could become sick with meconium aspiration syndrome. At this stage Oxytocin may be used to induce labor [41].

Miscarriage, also known as spontaneous abortion or pregnancy loss, is the natural death of an embryo (1-10 weeks) or fetus (after 11 weeks of gestation) before it is able to survive. The most common symptom of a miscarriage is vaginal bleeding. Risk factors for miscarriage are: previous miscarriages, exposure to tobacco smoke, obesity, diabetes, drug and alcohol use, age (risks begin to increase around the age of 30)[42].

As depicted on Figure 3.1, vaginal bleeding, if observed from the 1-24 weeks it may be a miscarriage. After that period it may be Antpartum Haemorrhage bleeding from the birth canal, which complicates 3-5% of pregnancies and is the leading cause of perinatal and maternal mortality worldwide [43].

To avoid pregnancy complications, the external tocogram and the intrauterine pressure catheter are the most used methods among clinicians for pregnancy monitoring, measuring mechanical contractions. However, more recently the Electrohysterogram measures the electrical activity, noninvasively, directly from the abdominal surface, promising to be a more accurate method than the currently used on clinical practice.

The aim of this thesis is the identification of the following events on the Electrohysterogram: Braxton Hicks, Alvarez contractions, Fetal Movements and Long Duration Low Frequency waves. As such, this chapter gives a more detailed description of the events to be identified in the Electrohysterogram. It also contains a description about the Electrohysterogram and its comparison with the external tocogram and intrauterine pressure catheter, as well as its signal and the database where it was extracted.

3.1 Uterine Contractions

The following events are present, or can be present, during pregnancy:

- **Contractions** – Before the thirty six weeks of gestation, contractions that do not cause effacement or dilatation of the cervix are the **Braxton Hicks** contractions. They can be characterized as having high amplitude and low occurrence rate (one every 3 to 4 hours). From the thirty six weeks of gestation contractions increase in frequency and strength up until the end of pregnancy. At parturition they propagate to the whole uterus in a short time (about 20 seconds): **labor contractions** [44][31]. First contractions can be felt at the earliest, 6 weeks of gestation and Braxton-Hicks appear at 20 weeks of gestation [26]. (Figure 3.1)

- **Alvarez waves** - Low-amplitude contractions with high occurrence rate (1-2 per minute). Primarily called Low Amplitude High Frequency (LAHF) waves, were first described by Alvarez and Caldeyro [13] as being asynchronic local contractions occurring randomly in different parts of the uterus, thus characterized as “uterine fibrillation”. At the time, low-amplitude-high frequency contractions were characterized as uterine irritability and given little importance. Nowadays it is believed that Alvarez waves lead to the development of more synchronous contractions of greater intensity and subsequently to preterm labor [45]. Thus, the identification of Alvarez waves is crucial to distinguish between term and pre term pregnancies. *Alvarez* waves appear frequently in records of women with multifetal gestations as they have a higher risk for preterm delivery [46]. They can be found in the first 30 weeks of gestation (Figure 3.1) [26].

- **Fetal Movements:** it may be disputed that this component is an artifact since it is related to the wellbeing of the fetus. It results from mechanical deformation of the abdomen due to the movements of the fetus. They have very low frequency content.

- **Long Duration Low Frequency (LDBF)-** These waves are associated with uterine hypertonus, i.e., a continuous contractile activity of the uterus, without returning to a total relaxation of the muscle. This type of activity is dangerous for the fetus as if it can compress the vessels that supply blood to the placenta [18].

- **Leman waves -** Similar to contractions, with very low frequency, neglected in the detection process and poorly documented [47].

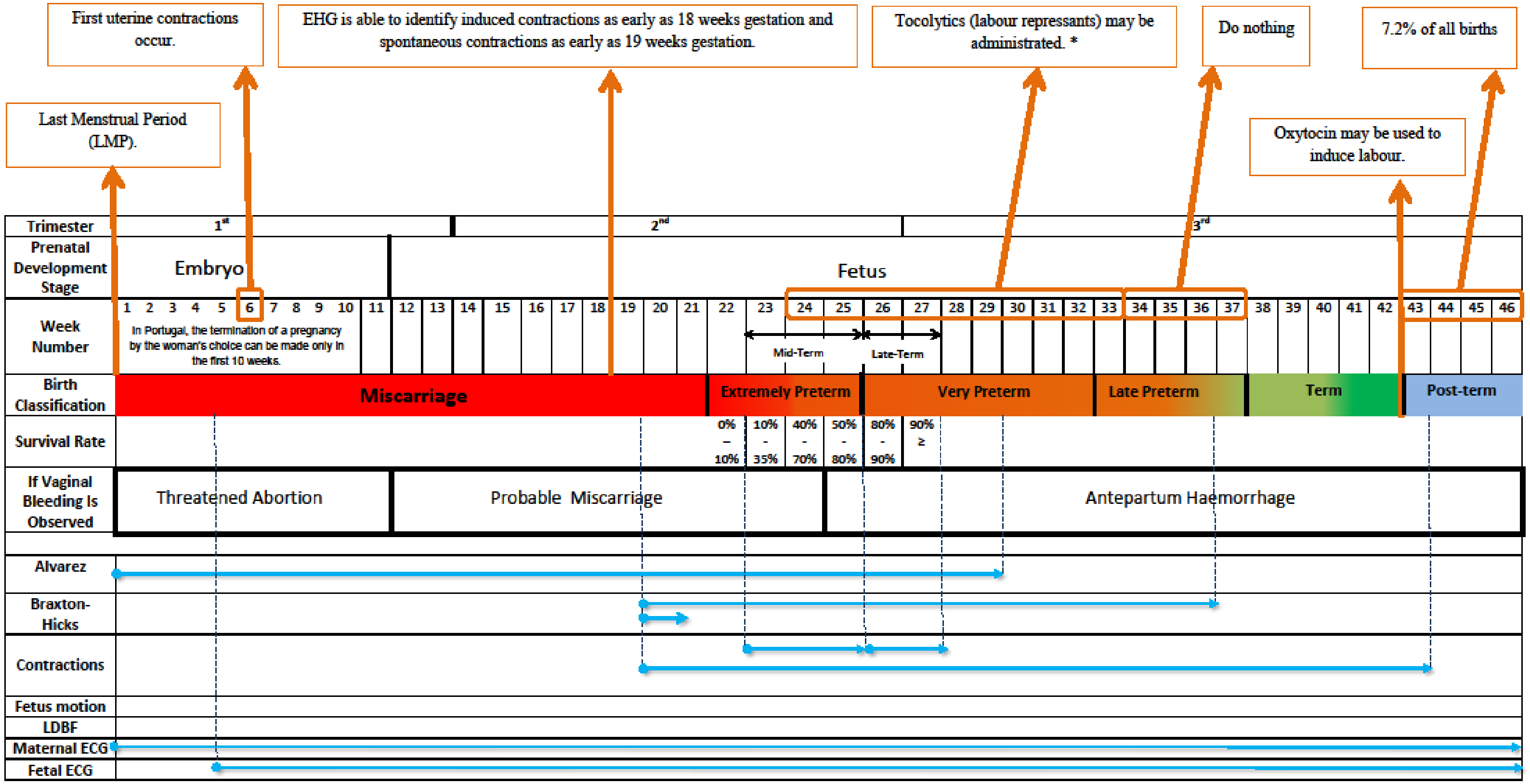

*Labour repressants (Tocolytics): These oxytocin antagonists delay delivery by 2-7 days, but carry side effects. To avoid respiratory distress syndrome in the fetus, glucocorticoids may be used to stimulate the production of surfactant in the lungs.

Figure 3.1 – Depiction of what happens throughout pregnacy: distribution of Alvarez waves, Braxton-Hicks, Contractions, Maternal and Fetal ECG, by gestational age and trimester of pregnancy. Survival rate of infants born preterm (Extremely Preterm and Very Preterm). Birth classification according to gestational week (Miscarriage, Extremelly very and late preterm, term and post-term).

3.2 Monitoring Uterine Contractions

3.2.1 Currently used methods

Currently the most used methods for evaluating uterine contractility include the External Tocograms (TOCO) or an Intrauterine Pressure Catheter (IUPC), which measure mechanical contractions.

Mechanical contractions are a result of the electrical signal propagation. As such, a muscle fiber is stimulated with an electrical pulse, responding with a twitch, thus exerting pressure on the abdominal wall, which is measured by both TOCO and IUPC [10][48].

- The **TOCO** measures the pressure with a tensometric transducer attached to the subject's abdomen and held in place by a stretch belt. This method has low accuracy and sensibility [10]. It is also influenced by the fetus movements within the uterine cavity, and maternal parameters such as body mass index, artifacts (respiratory or maternal movements) and by the elastic strap tension used to fasten the tocogram. Therefore, the TOCO must be constantly recalibrated and re-positioned correctly [11]. The TOCO is usually part of a device called cardiotocograph, which combines TOCO with a Doppler ultrasound device which is used to measure the fetal heart rate [49].

- **IUPC** is a more reliable tool as it is placed in the amniotic space during labor. It measures the fetal heart rate through an electronic transducer connected directly to the fetal scalp. However, is invasive, potential for infection, and there is a need for rupturing the membranes, being most applied in the cases where labor has been diagnose clinically. The IUPC records variations in the overall pressure, unlike the TOCO which records variations in local pressure [11][50][51].

External monitoring (TOCO) and internal monitoring (IUPC) are depicted in the figure bellow, Figure 3.2.

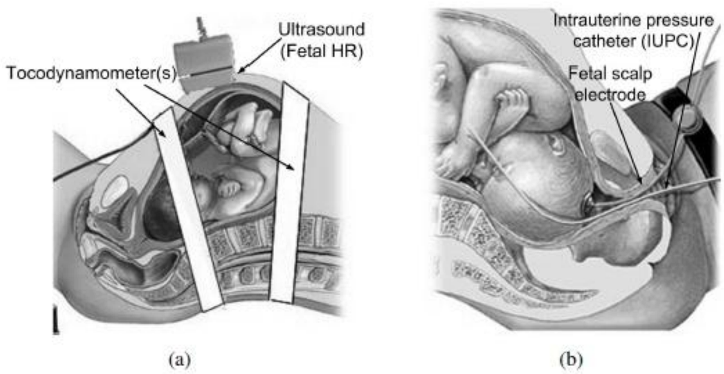

Figure 3.2 – Methods used in clinical practice: (a) External monitoring (TOCO) and (b) internal monitoring (IUPC) [from.[23]]

The methods described above are the most used methods in clinical practice regarding uterine contraction monitoring. In the next section, the Electrohysterogram will be introduced as an emerging alternative technology that may prove to be more accurate method for deducing contractions efficiently.

3.2.2 Electrohysterogram

The Electrohysterogram (EHG) measures the signal, noninvasively acquired, directly from the abdominal surface. Typically, the electrodes are placed near the navel close to the midline, where subcutaneous tissue is thinnest, being a good conduction path from the myometrium to the surface.

The electrical signal can also be acquired directly from the uterus with needle electrodes placed on the abdomen, which has the advantage of providing direct data from the uterus. However, it is invasive [51].

The EHG signal consists of intermittent burst of spike action-potentials that start earlier than the corresponding contraction. As such, single spikes can initiate contractions, but multiple, higher frequency, coordinated spikes are needed for forceful and maintained contractions. Electrical activity in the myometrium is low and uncoordinated during the early stages of pregnancy, but intense and synchronized as delivery approaches. Therefore, EHG can be useful for objective and reliable evaluations in the changes in the electrical pattern of the myometrium when delivery approaches, being able to identify between true and false labor, as seen in Figure 3.3 [11][50]. The frequency, amplitude and duration of contractions are determined, respectively, by the frequency of the bursts, the total number of myometrial cells that are activated simultaneously, and the duration of each burst [52].

In contrast, contractions measured with the TOCO can be large or small and can occur a large number of contractions per unit of time, regardless of whether the subject is in labor or not [51]. Furthermore, there is not a standard placement for the TOCO transducer and some uterine contractions can be missed [53]. Compared to the EHG, the TOCO provides mechanical information, whereas the EHG gives critical information about the firing rate and number of action potentials involved during contraction [51].

However, unlike the TOCO, EHG has a difficult visual interpretation because of its complex structure. Although bursts of action potentials can be recognized visually, their quantitative parameters concerning both time and frequency can only be determined by the use of a computer-aided system [54]. Furthermore, the EHG signal contains not only uterine activity but also a series of physiological interferences such as maternal and fetal electrocardiograms, abdominal muscle activity, baseline fluctuations and motion artifacts, as it will be further explained in more detail on section 3.2.4 [55].

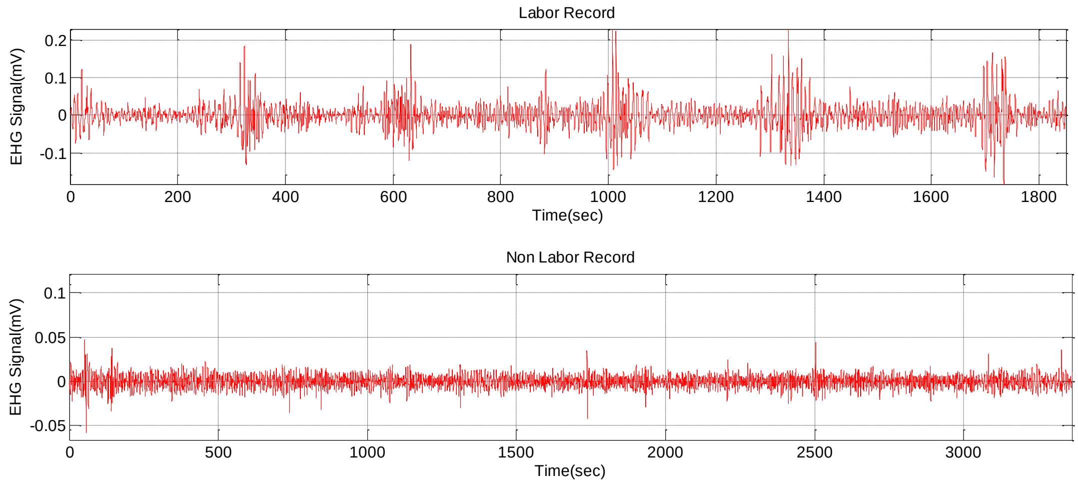

Figure 3.3 – Non labor vs labor contractions on the EHG: Contraction electrical burts, as measured by the EHG, are generally higher in amplitude and show higher action potential frequencies during labor than during non-labor.

The EHG signal analyzed in this thesis belongs to the Icelandic 16-Electrode EHG database, published on PhysioNet [56]. The signals were acquired between 2008 and 2010 in Iceland at Landspitali University Hospital, Akureyri Hospital and the Akureyri Primary Health Care Center. This database will be called Iceland Database from this point on.

Each participant was measured multiple times during pregnancy, resulting in a total of 122 recordings from 45 pregnant women in the third trimester of pregnancy (122 recordings) and during labor (10 recordings). Of the 45 participants, 32 were EHG recorded more than once during the same pregnancy and the highest number of recordings for a participant was seven. The lowest gestational age was twenty nine weeks and five days and the highest gestational age was forty one weeks and five days. The average recording duration was 61 minutes, for pregnancy and 36 minutes during labor.

To acquire the EHG signal sixteen electrodes were placed on the abdominal wall as well as a tocogram, which can be seen on Figure 3.4 [49] (interelectrode distance: 2.1 cm) The electrode numbering scheme is depicted on Figure 3.5, where it can be seen that the third vertical line of electrodes (electrodes 9 to 12) are placed on the median axis of the uterus and the 10^{th}-11^{th} pair of electrodes were placed half way between the uterine fundus and pubic symphysis. Finally, the reference electrodes were placed on each hip of the woman.

Figure 3.4 - The recording setup of the Iceland Database [from. [49]]

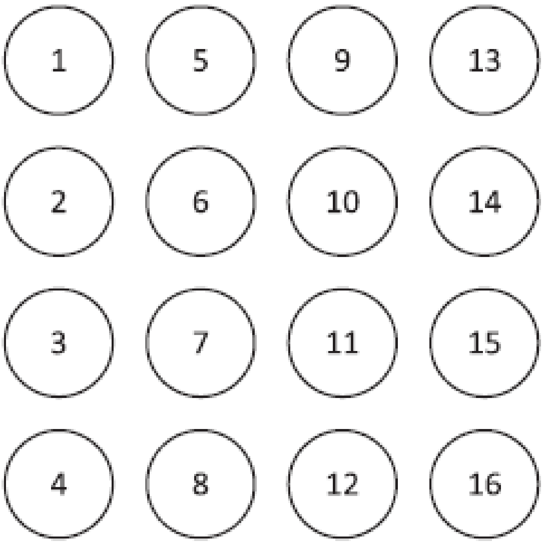

Figure 3.5 - Electrode numbering scheme [from. [49]]

The database includes simultaneously recorded TOCO's, obstetric information on participants (ID number, age, body mass index, gestational age of recordings and delivery, placental position, gravidity, parity, history of cesarian section, eventual mode of delivery) and annotations of the following events by the participant:

- C – Contraction – the participant feels a contraction or there is a very likely contraction on the TOCO (not always used when there is an obvious contraction on the TOCO.)
- (c) – Possible contraction – When there is not a very likely contraction but the participant has pressure sensation or a contraction is suspected on the TOCO.
- Pm – Participant movement.

- Pos – Participant change position.
- Fm – Fetal movement.
- Em – Equipment manipulation – When electrodes are pressed more firmly on the abdomen.

Further information about the recording and subject (Figure 3.6) was provided: In the first line there is information about the record name (Ice020_L_1of1), number of signals (16), sampling frequency (200) and number of samples per signal (770000). The lines that follow are signal specification lines containing, in the case of the first line: record name (Ice020_L_1of1.dat), format (16), ADC gain (131.068), units (mV), ADC resolution (15), ADC zero (0), Initial value (0), checksum (1533), block size (0) and description (1).

Also, under #info there is information regarding age, gestational age at recording and delivery, comments, among other things

```
Ice020_L_1of1 16 200 770000
Ice020_L_1of1.dat 16 131.068/mV 15 0 0 -1533 0 1
Ice020_L_1of1.dat 16 131.068/mV 15 0 0 -26190 0 10
Ice020_L_1of1.dat 16 131.068/mV 15 0 0 1362 0 11
Ice020_L_1of1.dat 16 131.068/mV 15 0 0 -23794 0 12
Ice020_L_1of1.dat 16 131.068/mV 15 0 0 -6349 0 13
Ice020_L_1of1.dat 16 131.068/mV 15 0 0 24336 0 14
Ice020_L_1of1.dat 16 131.068/mV 15 0 0 -8349 0 15
Ice020_L_1of1.dat 16 131.068/mV 15 0 0 -17046 0 16
Ice020_L_1of1.dat 16 131.068/mV 15 0 0 -13332 0 2
Ice020_L_1of1.dat 16 131.068/mV 15 0 0 -12322 0 3
Ice020_L_1of1.dat 16 131.068/mV 15 0 0 -15400 0 4
Ice020_L_1of1.dat 16 131.068/mV 15 0 0 -31514 0 5
Ice020_L_1of1.dat 16 131.068/mV 15 0 0 -17468 0 6
Ice020_L_1of1.dat 16 131.068/mV 15 0 0 25722 0 7
Ice020_L_1of1.dat 16 131.068/mV 15 0 0 -20572 0 8
Ice020_L_1of1.dat 16 131.068/mV 15 0 0 -17506 0 9

#Info:
#ID:Ice020
#Record type:Labour
#Record number:1/1
#Age(years):24
#BMI before pregnancy:20.9
#BMI at recording:27.2
#Gravidity:1
#Parity:0
#Previous caesarean:No
#Placental position:Posterior/Lateral left
#Gestational age at recording(w/d):41/5
#Gestational age at delivery:41/5
#Type of delivery:Vaginal
#Synthetic oxytocin use in labour:Yes
#Epidural during labour:Yes
#Comments for recording:
#Participant lay on left side in beginning of recording.
#Received epidural 2 hours 20 minutes before beginning of the recording.
Received another
#dose around 40 minutes into recording.
#Started to receive synthetic oxytocin (10ml/hour) around 40 minutes into
recording. Increased
#to 20ml/hour around 50 minutes into recording and 30ml/hour around 60
minutes
#into recording.
#Researcher was only in room for the first 23 minutes of recording.
#Baby born 8 hours and 30 minutes after beginning of recording.
```

Figure 3.6 – Comments on the regarding the fifht record done on subject 20

After acquiring the signal an anti-aliasing filter with cut-off frequency of 100Hz was used but no high pass filter. The signal sampling rate was 200 Hz and was digitized to 16 bits [49].

3.2.3 Contractions on the EHG Signal

The EHG signal is composed by two types of waves: a Slow Wave and a Fast Wave, being the last the more relevant signal as it seems to be directly related with cellular activity and thus responsible for mechanical activity. The uterine events, Braxton Hicks, Alvarez contractions, fetal movements, etc, are expected to be on that frequency range [57].

The **Slow Wave**, or abdominal, is associated with skin stretching and has no further electrical source [57]. There are some disagreements regarding its frequency range: 0.005–0.03 Hz [57], 0.014 - 0.033 Hz [31] and 0.03 - 0.1 Hz [58][59]. (Figure 3.7).

Fast waves contain information about the muscle activity and can be subdivided into two domains [57]:

- Low frequency band (0.1 - 0.6 Hz [57], 0.1 - 1.2 Hz [18][60], < 0.2 Hz [31], 0.2 – 0.45 Hz [5][20]), **Fast Wave Low** (FWL), always present during both pregnancy and parturition contractions.

- High frequency band (0.2 - 3 Hz [31], 0.6 - 3 Hz [57], 0.8 - 3Hz [5][20], 1.2 - 4.7 Hz [18][60]), **Fast Wave High** (FWH), associated with efficient parturition contractions.

The frequency range of the slow and fast waves as well as the already mentioned uterine contractions Braxton Hicks, Alvarez contractions, fetal movements, etc, is depicted in a scheme in Figure 3.7:

- The **Alvarez** frequency band is typically 0.2 Hz to 1 Hz [22], or as according to the results obtained by Marque et al. [17] 0 – 1 Hz.
- **LDBF** frequency band is [0-1] Hz [22].
- **Contraction** frequency band differs according to the gestational age: As reported by [22] at midterm the frequency of contractions is less than 0.2 Hz and at late term, is greater than 0.5 Hz.
- **Fetus movements** frequency is less than 0.5 Hz [22].

In Figure 3.7 there are also the frequency bands of the following artifacts: respiration, fetal and maternal electrocardiogram, which will be explained in more detail in the next section.

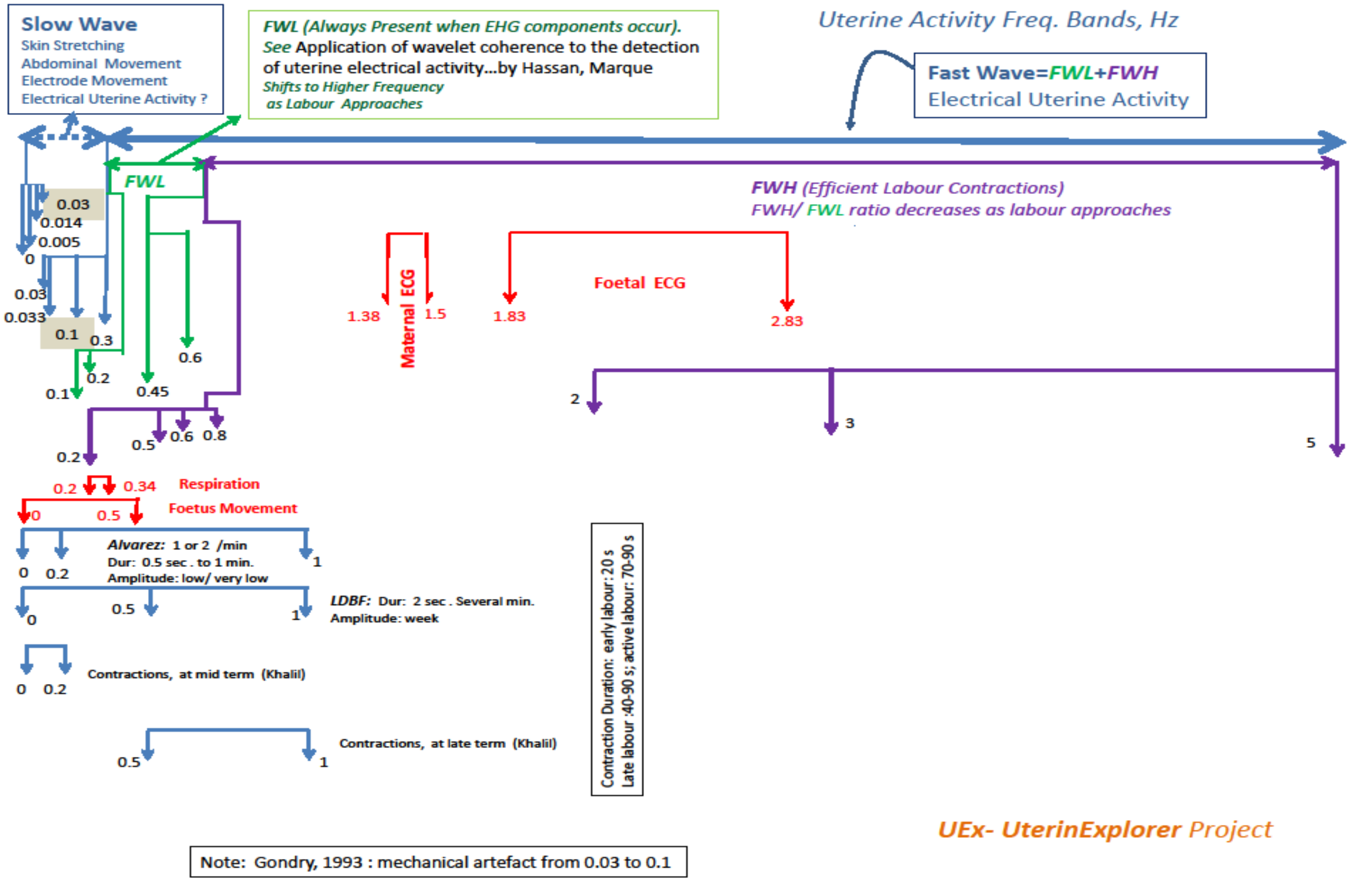

Figure 3.7 - Frequency distribution of components and artifacts on the EHG signal according to the literature: Alvarez, Contractions, LDBF, Fetus Motion as well as the interferences: respiration, fetal and maternal ECG

3.2.4 Artifacts on the EHG Signal

The EHG signal contains noise from numerous different sources that do not contribute to an understanding of the EHG [44]. Those sources can be a set of physiological interferences such as the mother's electrocardiogram (ECG), the abdominal electromyogram (EMG) and respiration as well as different motion artifacts [23][55].

- The **abdominal EMG** is the electrical signal due to voluntary contractions of the abdominal skeletal muscles, having a frequency component of about 30 Hz [23]. After low-pass filtering the noise, the EMG activity is negligible [61].

- The **respiration** artifact is mainly distributed between 0.20 and 0.34 Hz [55]. It usually happens during a large period of time and does not suffer large variations in amplitude by contrast to uterine electrical activity, and therefore it would not be detected as possible contraction [55]. Respiration can be removed with a with a high-pass filter with cut-off frequency at 0.34 Hz [61]. This interference is located in the "uterine-dominant" range, from 0.34 to 1.00 Hz, thus there is an interest on its removal from the EHG signal.

- **ECG components** are typically found above 1.0 Hz [62]. The minimum frequency content of the ECG corresponds to the minimum value of the instantaneous heart rate (HR). For example, a minimum ECG frequency content of 1 Hz corresponds to a HR of 60 beat per minute [61]. There are two types of ECG components: the maternal ECG and the fetal ECG, however the last one is typically much smaller than the maternal ECG, being barely detected by the EHG electrodes, hence is not a concern. As for the maternal ECG interference, it can be partially canceled by the use of bipolar electrodes [55] or by a low-pass filtering with the stop band lower frequency of the filter set at a minimum value of the instantaneous mother's HR determined during each recording [61].

It has been shown that EHG components distribute its energy from 0.1 – 5 Hz, thus not having any significant frequency component outside this frequency band [23][55]. In order to exclude the artifacts and other unwanted components, most authors study the changes occurring in the spectral region from 0.34 to 1.00 Hz, the so called "uterine-dominant" range [62][55][63][64][65][66][67].

According to [62], although large uterine components have been observed in the lower frequency range (<0.34 Hz), it is unclear whether they exhibit detectable changes useful for subject classification or prediction.

To suppress the signal disturbances the band-pass Butterworth filter is often chosen due to its maximum flat band-pass characteristics [68]. As such, in Figure 3.8 it is depicted a scheme of the lower and upper cut-off frequencies of the pass-band Butterworth filters used in the literature, with its localization regarding the EHG signal artifacts: respiration, maternal and fetal ECG, abdominal EMG.

As seen in Figure 3.8, some authors [23][69] suppress the unwanted artifacts with a band-pass Butterworth filter with cut-off frequencies at 0.1 and 0.8 Hz. In this case, the electrodes were located bellow the umbilicus, thus reducing the respiration interference.

In [70][71] the signal is filtered with a band-pass Butterworth filter with cut-off frequencies at 0.3 and 0.8 Hz, thus avoiding the respiration artifact and both fetal and maternal ECG.

Most authors [68][72][73] filter the signal with a 0.34-1 Hz band-pass Butterworth filter to which remove the unwanted artifacts.

In [44] an upper frequency limit of 1 Hz and a lower frequency limit of 0.1 Hz were chosen. With this frequency band the signal is still contaminated with respiration and motion artifacts. As such, it was implemented afterwards a cascade filter of a low-pass and high-pass Butterworth filter.

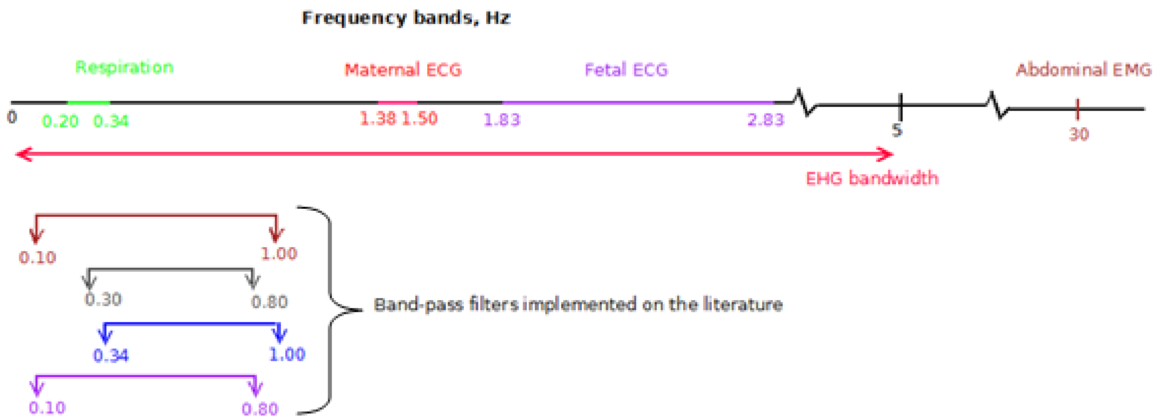

Figure 3.8 - Band-pass Butterworth filter frequency bands implemented on the literature [44][23][68][69][70][71][72][73]

The EHG has most of its energy in the frequency band of 0.1 to 1.5 Hz and many sources of noise have their main frequency components close to the frequency of the signal, which is the case of both maternal and fetal ECG as well as respiration, thus a classical filter cannot be used [23][55].

The following artifacts: Abdominal EMG, respiration and ECG components are the artifacts mentioned on the literature that can contaminate the EHG signal [44][23][68][69][70][71][72][73]. There are some other electrical signals: Stomach, Intestine, Colon, Bladder, Anus and Rectum (Table 3.1), which are not mentioned as a source of contamination of the EHG and, some of those, are in the uterine frequency band. However, it is not known if they are artifacts of the EHG.

Table 3.1 – Possible sources of EHG contamination: Stomach, Intestine, Colon, Bladder, Anus and Rectum [74][75][76][77][78][79]

Organ	Frequency Band
Stomach	0.033 – 0.07 Hz [74]
Tachygastria	0.063 – 0.15 Hz [74]
Bradygastria	0.0083 – 0.038 Hz [74]
Intestine:	
• **Duodenum**	0.18 – 0.25 Hz [75]
• **Jejunum**	0.15 – 0.18 Hz [75]
• **Ileum**	0.13 – 0.17 Hz [75]
Colon:	
• **Cecum**	0.042 – 0.067 Hz [76]
• **Ascending Colon**	0.033 – 0.15 Hz [77] and 0.15 – 0.22 Hz [76]
• **Sigmoid Colon**	0.1 – 0.17 Hz [76]
Bladder	0.07 – 1 Hz [78]
Anorectal:	
• **Rectum**	0.083 Hz [79]
• **Dentate line**	0.33 Hz [79]
• **Anorectal Junction**	0.225 Hz [79]
• **Anal Sphincter**	0.31 – 0.55 Hz [79]

3.2.5 Bipolar Signals vs Monopolar Signals

The bipolar signals are created by the differentiation between neighboring channels, thus rejecting the part of the signal that is common on both electrodes, keeping only the part that is dissimilar between the two electrodes (common noise rejection) [9].

Bipolar and specially monopolar EHG recordings capture interference from other physiological signals, such as abdominal muscle electrical activity, the electrocardiogram, respiratory movements, electrode-skin contact potential fluctuation, and movement artifacts from both mother and fetus [11]. The noise in monopolar EHG is non stationary and usually of high amplitude when compared to the signal of interest, being difficult to denoise, as classical filtering will remove also the interest signal. Furthermore, due to being corrupted with so much noise monopolar signals have a low signal to noise ratio (SNR).

However, monopolar signals provide better spatial resolution and do not bias the measured propagation directions, as bipolar methods do.

As for the bipolar signals, they are less noisy compared to the monopolar ones and have a higher SNR and for that reason most authors chose bipolar signal over monopolar [9].

Nevertheless, a bipolar signal is still a noisy signal, despite being relatively easy to filter, for instance Wavelet filtering is successful in removing maternal and fetal ECG as well as stationary electric noises.

The main disadvantages of bipolar signals are:

- It is likely that important information gets lost with the common rejection mode, due to the low frequency content of the signal that may induce a large wave length, and thus a common part of this lower activity recorded by both electrodes.
- Lower spatial resolution as it has fewer signals compared to the monopolar signals, thus reducing the spatial resolution.
- The computation of the bipolar signals, which is the difference between two neighbor electrodes, may create an external bias which affects the analysis of correlation between signals and specially when analyzing the direction of the correlation (causality) of the relationship between signals [9].
- This differentiation of signals is also known to affect the frequency content as, compared to the monopolar electrode, the bipolar electrode act as a high pass filter [9][80].

To compare monopolar and bipolar signals the spectrum and time-frequency representation of an EHG signal was performed on MATLAB, figures and conclusions are below:

Figure 3.9, top plot, shows the Power Spectrum of both unipolar channel 1 (blue) and bipolar channel 1-channel 2 (red). The middle plot is the bipolar channel 1- channel 2 and finally the unipolar channel 2.

As it can be seen both respiration (0.25Hz) and the maternal ECG (1.27Hz), present in both unipolar channel 1 and channel 2 were significantly reduced in the bipolar channel, which is clearly an advantage. Furthermore, the slow wave band (0-0.003Hz) is magnified in the bipolar channel, which is not an advantage since this is not relevant for the EHG classification. In the overall it is observed a power decrease of roughly 5 dB.

The time-frequency representation (explained in more detail on chapter 4), Figure 3.10, shows the maternal ECG quite visible on unipolar configurations (top and bottom) but practically inexistent on the bipolar channel (middle). The price paid for this artifact removal is represented on the ellipsis where it can be seen that the contraction energy is substantially decreased since it existed in both unipolar channels, which is undesirable. The same thing happens for the fetal movement, represented by the triangle.

In the central plot there is the Wavelet time marginal for both bipolar signal (green) and the unipolar signal (blue). It can be seen that the blue line (unipolar signal) better detects the multiple contraction events on the EHG signal.

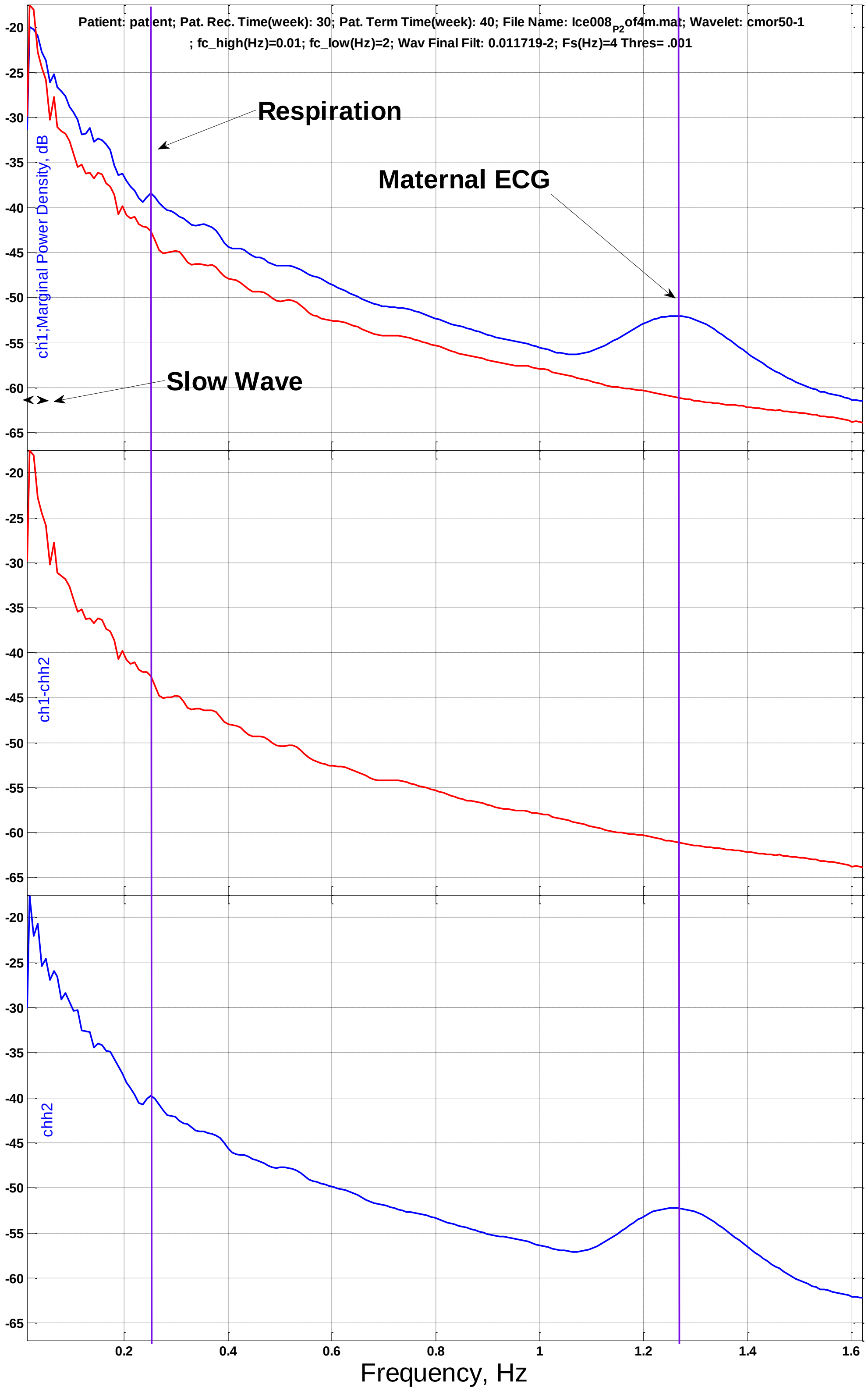

Figure 3.9 - Power Spectrum of an EHG signal: unipolar channel 1(blue, top plot), bipolar channel 1-channel 2 (red, top plot and middle plot) and unipolar channel 2 (bottom plot). Maternal ECG and respiration artifacts, present on both unipolar channels are reduced in the bipolar channel. However, the slow wave band is magnified in the bipolar channel.

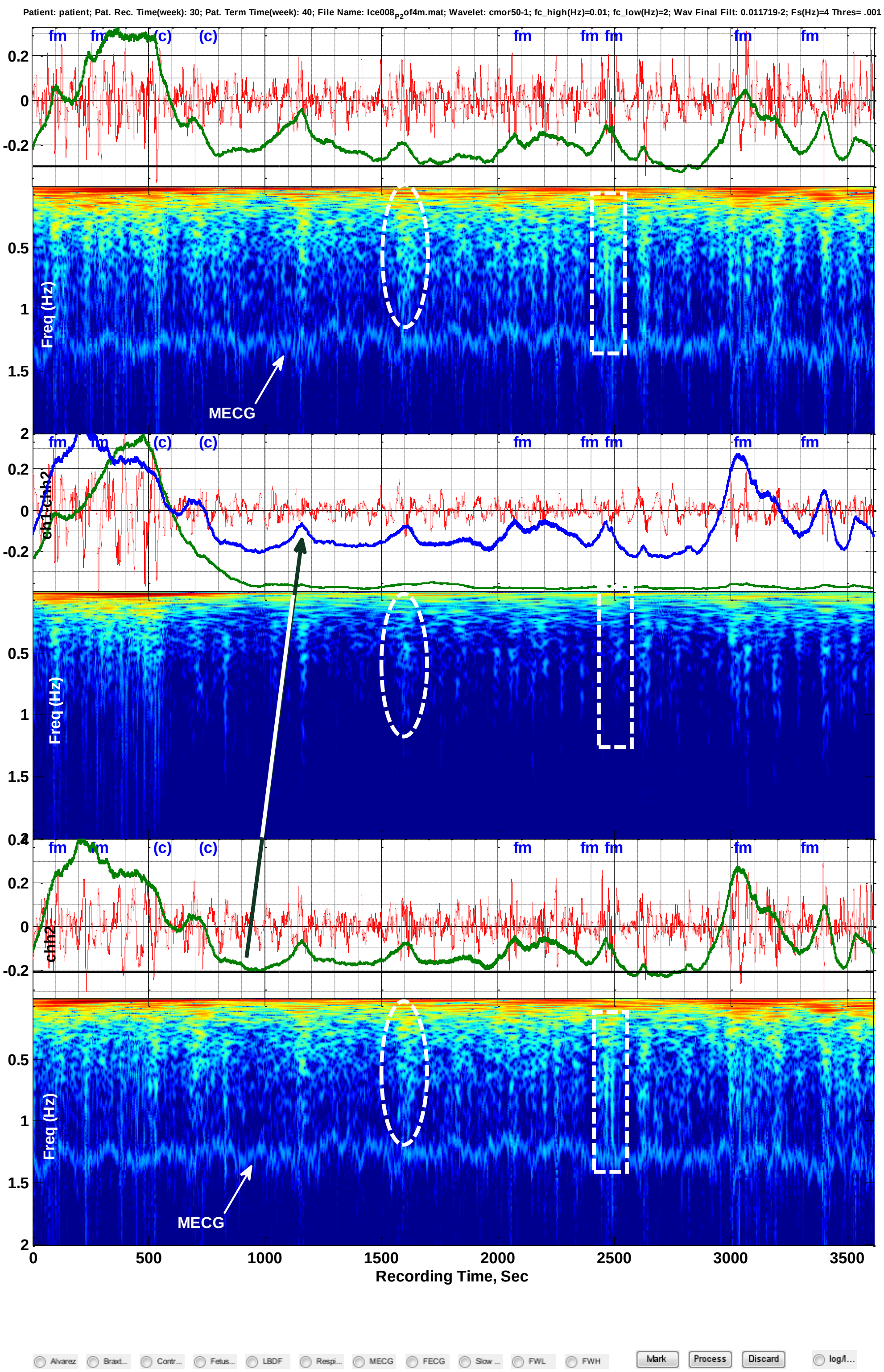

Figure 3.10 - Time-Frequency reprentation of an EHG signal: EHG signal (red, top plot) with respective Wavelet time marginal (green, top plot) and Scalogram for the following channels: channel 1 (first plot), channel 1-channel 2 (middle plot) and channel 2 (bottom plot). In the middle plot there is the Wavelet time marginal of both bipolar channel (green) and unipolar channel 2 (blue). The maternal ECG is reduced in the bipolar channel. There is a contraction (ellypsis) and fetal movement (rectangle) on both unipolar channels, whose energy is significantly reduced in the bipolar channel.

Chapter 4

Time-Frequency Analysis

Time-Frequency analysis maps the signal in both time and frequency domain simultaneously. It requires linear techniques: Short-Time Fourier Transform, Wavelet Transform and the Bilinear Techniques: Wigner-Ville, Choi-Williams, Spectrogram and Scalogram.

The main difference between linear and bilinear methods is that the linear transforms are invertible, whereas the bilinear form is irreversible as the original time waveform cannot be restored from the time-dependent spectrum. Moreover, the linear methods are fast and have an easy formulation and implementation but do not have enough resolution for many applications. On the other hand, bilinear methods have better resolution in the time-frequency domain although they show, in general, cross-term interference that masks the auto-terms [81].

There are two main groups of signals: deterministic and stochastic (Figure 4.1). Deterministic signals can be exactly described mathematically or graphically. Real-world signals, such as the EHG signal, are never deterministic. There are always some unknown and unpredictable mechanisms, noise, parameters variation that render it nondeterministic.

The EHG signal belongs to the stochastic class. Those signals cannot be expressed exactly; they only can be expressed in terms of probabilities.

Stochastic signals can also be subdivided into stationary or nonstationary. Stationary stochastic processes are processes whose statistics do not change in time. However, The EHG signal is nonstationary. As such, one must therefore use nonstationary processing methods (such as, for example, the Wavelet transformation) which are relatively complex or cut the signals into short duration segments in such a way that each can be considered stationary [82].

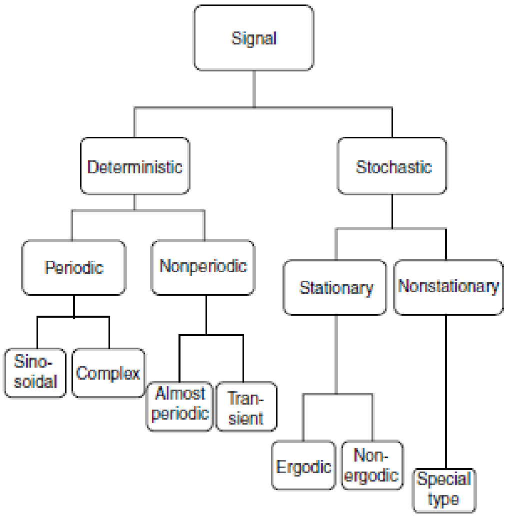

Figure 4.1 - Classification of signals according to characteristics [from.[82]]

In this chapter there is a brief explanation of the theoretical aspects of each time-frequency analysis technique.

4.1 Time-Frequency Analysis vs Spectrum Analysis

Spectrum Analysis techniques rely on the presumption that properties, e.g., frequency content, of the signal changes slowly with time. When that is not the case, the time-frequency representation of the signal has advantages. The EHG signal is a non-stationary signal therefore time-frequency analysis is required.

The following example shows the need for time and frequency analysis. In Figure 4.2 there are two non-stationary signals and its correspondent Periodogram spectra, i.e., the squared absolute values of the Fourier transforms. The chirp signal and the impulse signal have very different appearances in time, Figure 4.2 a) and b). However, the Periodogram spectra is exactly the same.

With the use of time-frequency analysis, in this case Spectrograms, these differences become clear, Figure 4.3 a) and b), where red color indicates high power and blue color, low power [83].

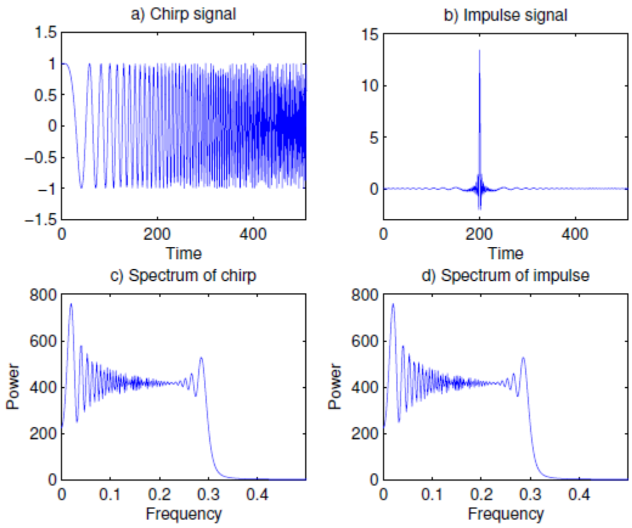

Figure 4.2 - Two different signals with the same spectral estimates but different appearance in time [from.[83]]

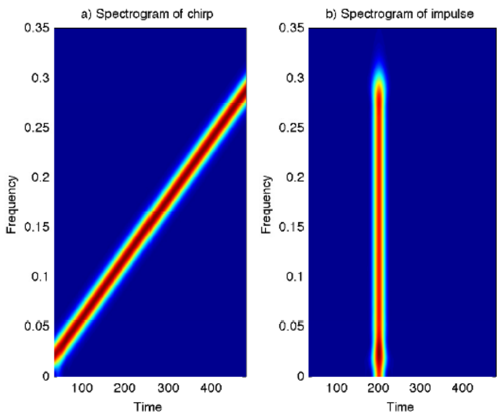

Figure 4.3 - Spectrograms of the chirp and impulse signals (Red color: high power, blue color: low power) [from.[83]]

Time-Frequency analysis requires:

- Linear techniques:
  - ✓ Short-Time Fourier Transform
  - ✓ Wavelet Transform
- Bilinear Techniques, which contains the
  - ✓ Cohen's class (Wigner-Ville, Choi-Williams, Spectogram, Scalogram)
  - ✓ Affine Distribution.

In this chapter the following techniques will be compared: Short-Time Fourier Transform, Wavelet Transform, Wigner-Ville and Choi-Williams. The mentioned techniques perform an analysis both in time and frequency domain:

- **Analysis in time domain** – How the signal amplitude varies with time.
- **Analysis in frequency domain** – allows determining the existence of different frequency components in the signal, as well as information on the amplitude of these components.

4.2 Linear Techniques

Linear techniques decompose the signal into elementary components, the atoms, well localized in time and in frequency. Two well know examples of such decompositions are the Wavelet Transform and Fourier Transform [84].

4.2.1 Short-Time Fourier Transform

Fourier analysis expands a function in terms of sinusoids (or complex exponentials), revealing all frequency components present in a function. However, Fourier analysis cannot simultaneously provide time and frequency localization and is not useful for analyzing time-variant, non stationary signals, which is the case of the EHG signal [85].

The Short-Time Fourier Transform (STFT) is a technique based on the Fourier Transform (FT) to analyze non stationary signals. As illustrated in Figure 4.4, the STFT employs a sliding window function g(t) that is centered at time τ . For each window, a time-localized FT is performed on the signal x(t) within the window. Subsequently, the window is moved by τ along the time line, and another FT is performed. Through such consecutive operations, FT of the entire signal can be performed. The signal segment within the window function is assumed to be approximately stationary. As a result, the STFT decomposes a time domain signal into a 2D time-frequency representation, and variations of the frequency content of that signal within the window function are revealed [85].

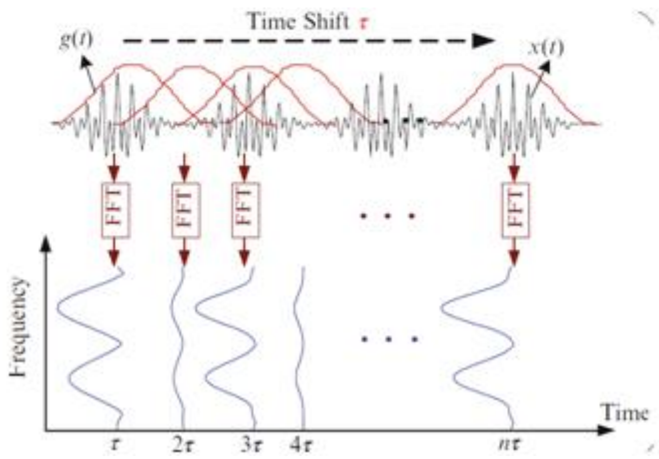

Figure 4.4 - Short-Time Fourier Transform: a window is moved by τ along the time line, performing the FT of the signal x(t). the STFT decomposes a time domain signal into a 2D time-frequency representation, revealing variations of the frequency content of that signal within the window function [from [85]]

The STFT at time τ and frequency f can be expressed in Equation 4.1 as:

$$STFT(\tau, f) = \int x(t) g^{*}_{\tau,f}(t) dt = \int x(t) g(t-\tau) e^{-j2\pi ft} dt \tag{4.1}$$

Where x(t) the signal to be transformed and $g(t-\tau)$ the window function centered at the time, τ .

There are various types of window functions, each one for different purposes, for example, the Gaussian Window is designed for analyzing transient signals, and the Hamming and Hanning windows are applicable to narrowband, random signals. The choice of the window function affects the time and frequency resolutions of the analysis result. [85]

To reduce the redundancy of the continuous STFT, it can be sampled in the time frequency plane, thus obtaining the discrete STFT. [84]

To Sum up, STFT is a compromise between time-based and frequency-based views of a signal, providing some information about both when and what frequencies a signal event occurs. However, there is a trade-off between time and frequency resolutions, which is determined by the size of the window: a good time resolution requires a short window, and a good frequency resolution requires a long window, conditions that cannot be simultaneously satisfied. Moreover, when choosing a particular size for the window, that window is the same for all frequencies [84][85].

4.2.2 Continuous Wavelet Transform

Many signals require a more flexible approach – the window size can be varied to determine more accurately either time or frequency.

The Wavelet Transform (WT) is a tool for carving up functions, operators, or data into components of different frequency, allowing one to study each component separately.

Wavelets are functions defined over a finite interval and having an average value of zero. The basic idea of the WT is to represent any arbitrary function f(t) as a superposition of a set of such Wavelets or basic functions. These functions or baby Wavelets are obtained from a single prototype Wavelet called the mother Wavelet, by dilations or contractions (scaling) and translations (shifts) [85].

The Continuous Wavelet Transform (CWT), equation 4.2, is defined as the sum over all time of the signal multiplied by a scale, shifted version of the Wavelet function:

$$CWT(s,\tau) = \int f(t)\Psi^{*}_{s,\tau}(t)dt \qquad (4.2)$$

At equation 4.2 * denotes complex conjugation. This equation shows how a function f(t) is decomposed into a set of basic functions $\psi_{s,\tau}(t)$, called the Wavelets. The variables s and τ are the new dimensions, scale and translation (position), after the WT. Also, if the CWT can be sampled in the time frequency plane, thus obtaining the discrete WT [85].

The Wavelets are generated from a single basic Wavelet, $\psi(t)$, called mother Wavelet, equation 4.3, by scaling (i.e., stretching or compressing) and translation- Scaling a Wavelet means stretching (or compressing) and translating (i.e., delaying or hastening its onset).

$$\Psi_{s,\tau}(t) = \frac{1}{\sqrt{s}}\Psi\left(\frac{t-\tau}{s}\right) \qquad (4.3)$$

In the above equation: s is the scale factor, τ is the translation factor and the factor $s^{-1/2}$ is for energy normalization across different scales.

The WT enables variable window sizes to analyze different frequency components within the signal. As seen in Figure 4.5 the signal is compared with a set of template functions obtained from scaling and shift of a base Wavelet Ψ(t) and looking for their similarities [85].

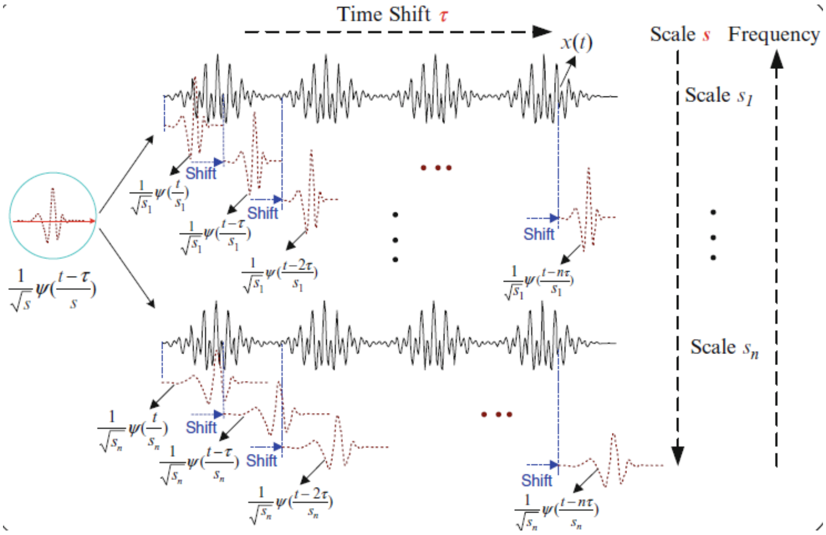

Figure 4.5 – Wavelet Transform: The signal is compared with a set of template functions obtained from scaling and shift of a base Wavelet Ψ(t) and looking for their similarities [from [85]]

The biggest problem with the WT is choosing the mother-Wavelet. However, for the CWT it is advisable to use Wavelets without filters: cgau, shan, fbsp, cmor, gaus, mexh, morl, which narrows the possibilities.

4.2.3 Discrete Wavelet Transform and Wavelet Packet Decomposition

The Discrete Wavelet Transform (DWT) is implemented by a sequence of digital filtering of the original signal. The signal (x[n]) passes through a low pass filter (h[n]), which generates the detail coefficients and also passed through a high pass filter (g[n]), generating an approximation coefficient. (Figure 4.6) The approximation coefficients are the high-scale, low-frequency components of the signal whereas the detail coefficients represent the low-scale, high-frequency components.

After filtering the signal is down sampled, factor of two, resulting in half of the original signal coefficients, which means that it is kept only one point out of two in each of the samples to get the complete information [86][87].

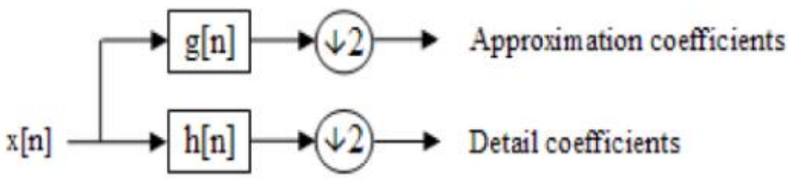

Figure 4.6 - Discrete Wavelet Transform: Signal x[n] is passed through lowpass and highpass filters and it is down sampled by two [from.[86]].

In the Wavelet Packet Decomposition (WPD) the signal is passed through more filters than the DWT.

In the DWT, each level is calculated by passing the previous approximation coefficients through a high and low pass filters. However, in the WPD, both the detail and approximation coefficients are decomposed, as seen on Figure 4.7 [86].

The WPD are more efficient to study high resolution cases as there are no loss of detail in higher frequencies and the final level of this multi-level decomposition tree are the coefficients that can be used to reconstruct the original signal. However, these coefficients are in no sequential order in terms of frequency, which should be noted before reconstructing the signal [87].

Also, for n levels of decomposition the WPD produces 2^n different sets of coefficients (or nodes) as opposed to (n+1) sets for the DWT [86].

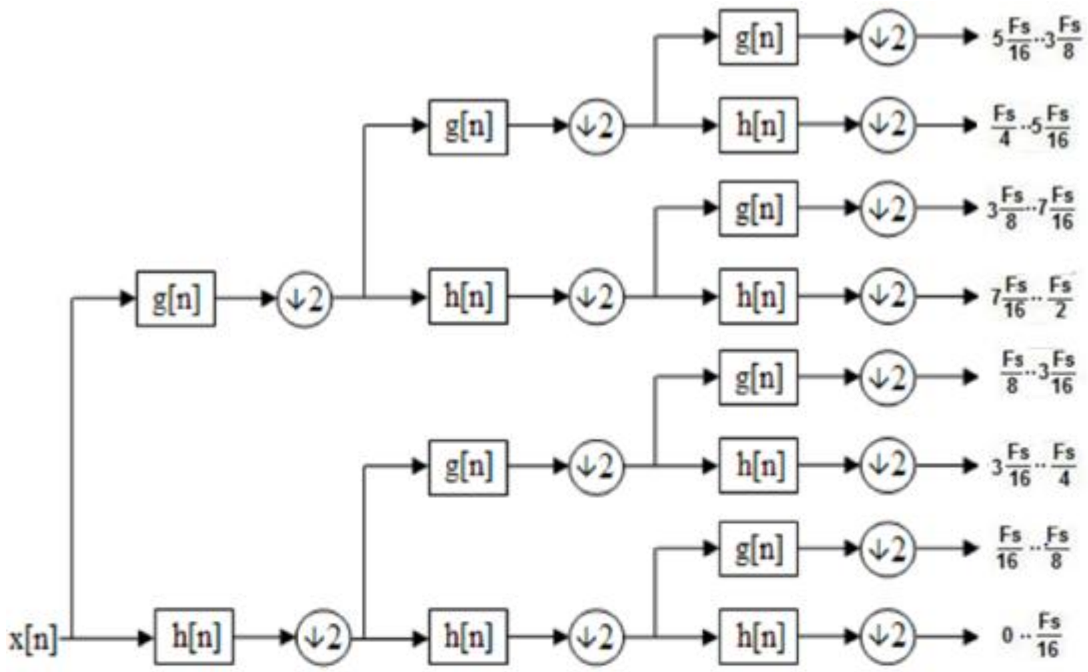

Figure 4.7 - Wavelet Packet Decomposition: Both the detail and approximation coefficients are decomposed by high and low pass filters [from.[86]]

4.3 Bilinear Time-Frequency Distributions

The so called bilinear time-frequency distributions can be formulated, equation 4.4, as the multiplication of the ambiguity function, Az(f, τ), with the ambiguity kernel, φ(f, τ).

$$A_Z^Q(f,\tau) = A_Z(f,\tau)\cdot\phi(f,\tau) \qquad (4.4)$$

Therefore, The ambiguity function, Az(f,τ), has the name ambiguous standing for something that is not clear defined. It is a function that measures the time-frequency correlation of a signal x, i.e. the degree of similarity between x and its translated version in the time-frequency plan. The ambiguity function is defined in equation 4.5, where z(t) is the analytic signal, t the time, f the frequency and τ is the lag:

$$A_Z(f,\tau) = \int_{-\infty}^{\infty} z(t+\frac{\tau}{2})z^*(t-\frac{\tau}{2})e^{-i2\pi ft}dt \qquad (4.5)$$

The ambiguity kernel acts as a weighting function trying to let the signal terms unchanged and rejecting the interference terms [83][84][88][89].

4.3.1 Wigner-Ville Distribution

The Wigner-Ville Distribution (WVD) is a time-frequency energy distribution defined as:

$$W_x(t,f) = \int_{-\infty}^{\infty} x(t+\frac{\tau}{2})x^*(t-\frac{\tau}{2})e^{-i2\pi f\tau}d\tau \qquad (4.6)$$

Where x(t) is the signal, t the time, f the frequency and τ is the lag. The WVD has the simple ambiguity domain kernel φ(f, τ)=1

In an analogy to the STFT, the window is basically a shifted version of the same signal. It is obtained by comparing the information of the signal with its own information at other times and frequencies.

The WVD is a fundamental concept for increased resolution in time frequency distributions, especially compared to the STFT. However, the WVD has severe interference (cross) terms that confuse interpretation and require additional effort to resolve [83][84][88][89]. As such and because the WVD is a bilinear function of a signal $x(t)$, according to the bilinear superposition principle:

$$W_{x+y}(t,f) = W_x(t,f) + W_y(t,f) + 2\Re\{W_{x,y}(t,f)\} \qquad (4.7)$$

where the cross-WVD of x and y is given by:

$$W_{x,t}(t,v) = \int_{-\infty}^{+\infty} x(t+\tau/2)y^*(t-\tau/2)e^{-j2\pi f\tau}d\tau \qquad (4.8)$$

Therefore, in the WVD a third point is created by the interference of two points in the time-frequency plane. The point created by the interference is located in the geometrical midpoint of the two points interfering with each other. Also, these interference terms oscillate perpendicularly to the line joining the two points interfering, with a frequency proportional to the distance between these two points.

These cross-terms must be present or the good properties of the WVD cannot be satisfied (marginal properties, instantaneous frequency and group delay, localization …).

Compared to the Scalogram the WVD gives the best resolutions (both in time and frequency), but presents the most important interferences, whereas the spectrogram gives the worst resolutions, but with nearly no interferences [84].

4.3.2 Choi-Williams Distribution

This distribution corresponds to a particular case of the Cohen's Class also known as the Reduced Interference Distributions (RID) [84].

As such, RID are methods to reduce cross terms, or interference terms. The most applied RID is the Choi-Williams Distribution (CWD) also known as Exponential Distribution (ED) with the ambiguity kernel defined in equation 4.9 as:

$$\phi ED(f,\tau) = e^{-\frac{f^2\tau^2}{\sigma}} \tag{4.9}$$

In equation 4.9: σ is a design parameter, f the frequency and τ is the lag. Also, the CWD also classified as product kernel which has the advantage in optimization of being dependent of one variable, i.e., x=fτ [83][89]. And when $\sigma\rightarrow+\infty$ the WVD is obtained. Inversely, the smaller is the σ, the better the reduction of the interferences.

Despite having less interference terms when compared to the WVD, the efficiency of this distribution strongly depends on the nature of the analyzed signal. For example, if the signal is composed of synchronized components in time or in frequency, the CWD will present strong interferences [84].

4.3.3 Spectrogram

The Spectrogram can be interpreted as a measure of energy of the signal contained in the time-frequency domain. Considering the squared modulus of the STFT, it is obtained the spectral energy density of the locally windowed signal $x(t)h^*(t-\tau)$:

$$S_x(\tau,t) = \left| \int_{-\infty}^{+\infty} x(t)h^*(t-\tau)e^{-j2\pi ft}dt \right|^2 \tag{4.10}$$

The Spectrogram being the squared magnitude of the STFT has a limited time-frequency resolution. As mentioned before, there is a trade-off between time resolution and frequency resolution which is the main drawback of this representation.

The Spectrogram contains interference terms. However, if the signal components are sufficiently distant so that their Spectrograms do not overlap significantly, than the interference term will be nearly zero. This property is a good consequence of poor resolution [84].

4.3.4 Scalogram

The Scalogram shows the energy distribution along the two variables time and frequency. Each coefficient is represented by a color corresponding to the magnitude of the coefficient. As such, blue represents the low energies, followed by green, yellow and red for higher energies.

The Scalogram is the square of the CWT modulus (Equation 4.11)

$$\left|\Psi_{s,\tau}(t)\right|^2 = \left|\left|s\right|^{-1/2} \int_{-\infty}^{+\infty} f(t)\psi^*\left(\frac{t-\tau}{s}\right)dt\right|^2 \tag{4.11}$$

By contrast with the STFT, which uses a single analysis window, the CWT uses short windows at high frequencies and long windows at low frequencies (Figure 4.8). As such, short windows represent a long time interval with a short frequency range. As for long windows, they represent small time intervals with large frequency ranges [84][90].

The interference terms of the Scalogram, as for the Spectrogram, are also restricted to those regions of the time frequency plane where the corresponding signal terms overlap. Hence, if two signal components are sufficiently apart in the time-frequency plane, their cross-Scalogram will be essentially zero [84].

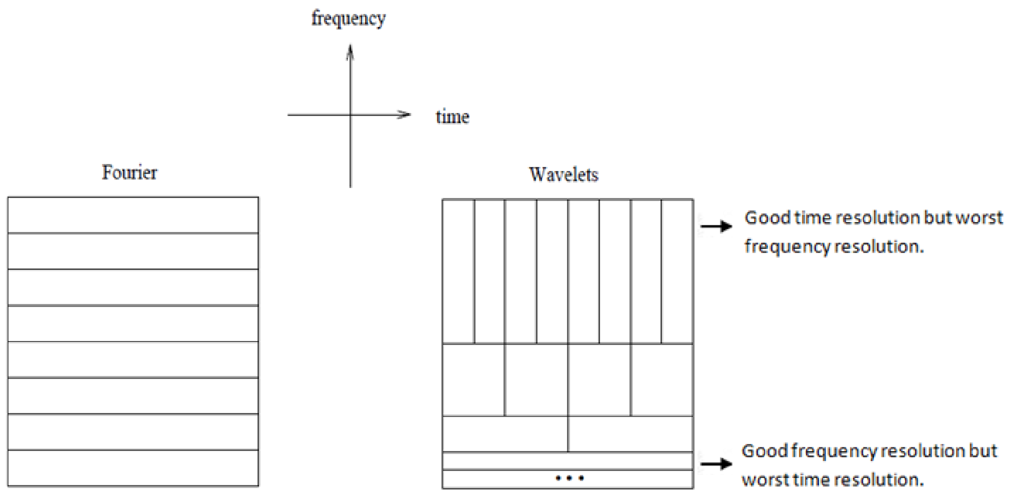

Figure 4.8 - Time frequency representation of the STFT and CWT: The STFT uses a single analysis window. The CWT uses short windows at high frequencies and long windows at low frequency [from.[84]] .

4.4 Marginal Distributions

The marginal distributions of a time-frequency representation express, by integrating the representation along one variable, the repartition of energy along the other variable.

The time marginal, which corresponds to the instantaneous power of the signal is defined as follows:

$$M_t(f) = \int_{-\infty}^{+\infty} tfr(t, f)dt \qquad (4.12)$$

where tfr(t,f) is the time frequency representation [84].

In turn, the frequency marginal corresponds to the energy spectral density, which can be interpreted as the energy per unit of bandwidth of the spectral components of the signal x(t) centered at a frequency f. Is obtained as follows:

$$M_f(t) = \int_{-\infty}^{+\infty} tfr(t, f)df \qquad (4.13)$$

where tfr(t,f) is the time frequency representation [84].

4.5 Methods Comparison

With the purpose of comparing the methods above exposed the software Time-Frequency Toolbox for use with MATLAB was used to generate a signal and the following methods were applied to the signal: WT, STFT, WVD and CWD. Afterwards, the same methods were applied to an EHG signal.

Therefore, the generated signal, Figure 4.9, contains three Gaussian atoms in the time-frequency plane. The atom that appears at time 100s and frequency 0.4Hz shares the same time as the atom localized in the bottom left of the time-frequency graph (t=100s and f=0.2Hz) and the same frequency as the atom in the right (t=400s and f=0.4Hz).

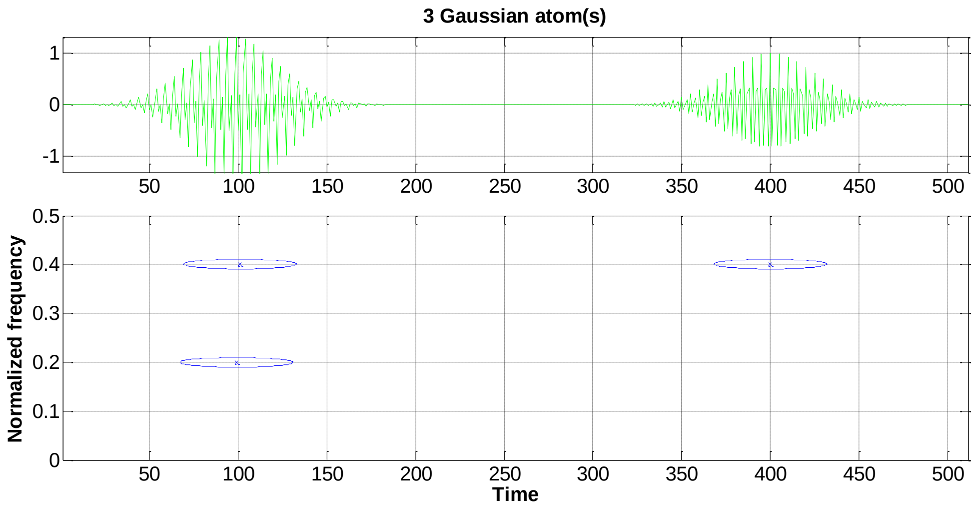

Figure 4.9 - Time representation of three gaussian atoms (above) and its respective time-frequency representation (below)

As such, it was computed the WVD of the signal (Figure 4.10, top left) and as it can be seen in the time-frequency representation each point interfere with the other two creating an interference located in their geometrical midpoint. The interferences are not very energetic, however can cause confusion on the time-frequency plane analysis.

The CWD applied to the same signal (Figure 4.10, top right), shows only interference along the time axis, i.e. only the atoms occurring at the same time interfere with each other.

Finally, by applying the Scalogram (Figure 4.10, bottom left) and Spectrogram (Figure 4.10, bottom right) to the same signal the interference disappears in both cases. Between the two methods, the Scalogram yields the best results in terms of resolution, as expected.

However, even though the interference disappears in the Scalogram, there is a loss in resolution, especially in the lower frequencies compared with the results yield by the CWD and WVD distributions, being the last one the best in terms of resolution.

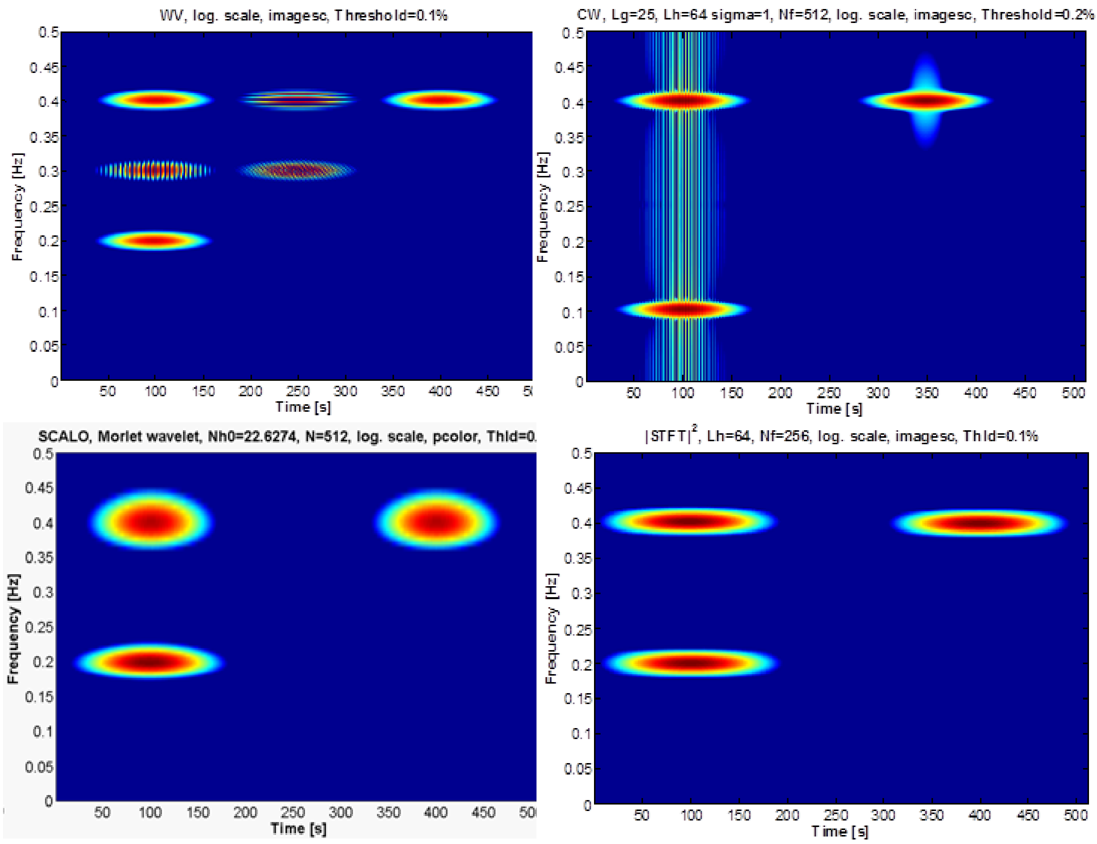

Figure 4.10 - Time-Frequency representation of three gaussian atoms: WVD (top left), CWD (top right), Scalogram (bottom left) and Spectrogram (bottom right) in logaritmic scale. Both CWD and WVD have interference terms, however those two are the best methods in terms of resolution. In the Scalogram and Spectrogram the interference disappears. Between the two the Scalogram has better resolution.

Despite the resolution loss, the uterine EHG signal has components occurring at the same time and/or frequency and to avoid interferences the Scalogram will be used. As such, the following example illustrates the difference of results yield by the four methods, in an EHG signal.

In Figure 4.11, there is the time representation of an EHG uterine signal, below the following time-frequency representations of the same signal: WVD (middle left), CWD (middle right), Scalogram (bottom left) and Spectrogram (bottom right).

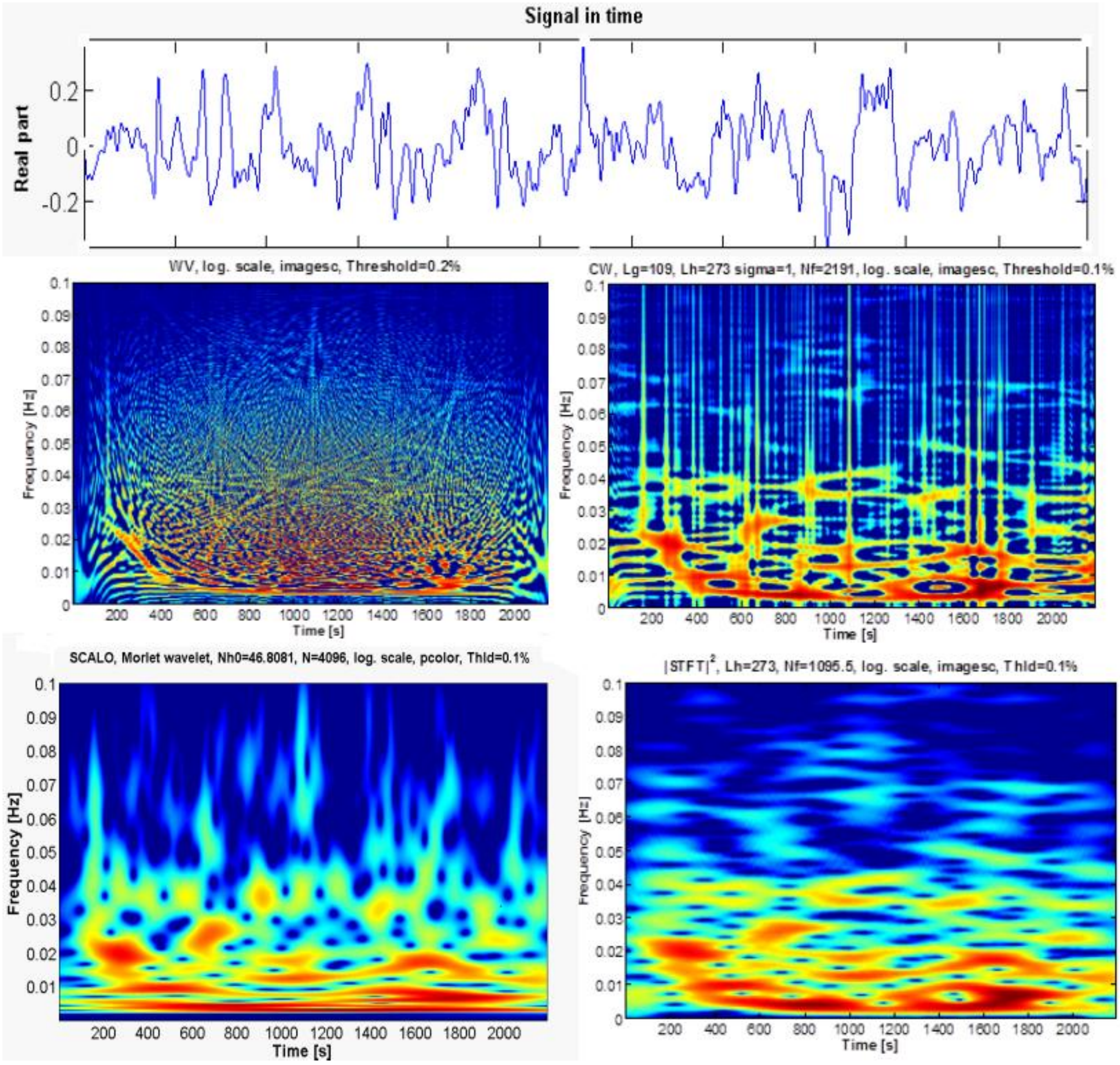

Figure 4.11 - Time representation of an EHG signal (above) and time-frequency representations of the EHG signal: WVD (middle left), CWD (middle right), Scalogram (bottom left) and Spectrogram (bottom right): all in logaritmic scale. Despite better resolution, the WVD and CWD introduce cross-terms, which does not happen with both Scalogram and Spectrogram. The Scalogram resolution is considerably better than the Spectrogram

As it can be seen on Figure 4.11, the WVD and CWD introduce cross-terms in the time-frequency plane which can disturb the readability of the representation. In turn, both Scalogram and Spectrogram seem to produce much less cross-terms than the other two methods, despite inferior resolution.

The Scalogram resolution is considerably better than the Spectrogram, thus making it the chosen time-frequency method in this thesis.

Chapter 5

Spectral Analysis and Energy Estimation

Spectral analysis considers the problem of determining the spectral content (i.e, the distribution of signal power or amplitude over frequency) of a time series from a finite set of measurements, by means of either parametric or nonparametric techniques.

Despite the EHG signal being a non-stationary signal, it is of interest to see the power distribution over frequency. Since this is a widely used method in this research area. The assumption is made that the EHG signal is approximately stationary in the time interval.

Nonparametric methods are based on the Fourier transform and are used when little is known about the signal. In turn, the parametric methods assume that the signal satisfies a generating model with known functional form, thus the signal spectral characteristics of interest are derived from the estimated model [91].

Apart from the spectral analysis, the following features will be applied to the EHG signal: Time-Average Power, Root Mean Square, Teager Operator and Crest Factor, providing energy estimations and in the case of the Crest Factor, a ratio between the peak values of the EHG signal with their effective value.

As such, this chapter briefly describes the theoretical basis of both parametric and nonparametric methods of spectral analysis, as well as the already mentioned tools for energy estimation and Crest Factor.

5.1 Power Spectral Density with Nonparametric Methods

5.1.1 Discrete-time Fourier Transform

The discrete-time Fourier series analysis, used in this work, is an extension of the continuous analysis procedure, but modified by two operations: sampling and windowing [92].

As a result, the Discrete Fourier Transform (DFT) takes a vector of N complex numbers x_k, k=0…N-1, and transforms it into a vector of N complex numbers y_m, m=0…N-1.

The computer uses the Fast Fourier Transform (FFT) algorithm to compute the DFT:

$$y_m = \sum_{k=0}^{N-1} x_k \exp(-2\pi i \frac{mk}{N}) \text{ , m=0…N-1} \tag{5.1}$$

The Power Spectral Density (PSD) describes how the power of a time series is distributed with frequency. Mathematically, is defined as the FT of the autocorrelation sequence of the time series.

The steps to compute PSD are:

- Multiplying one segment of the time series with a suitable window function.
- Performing a DFT.
- Scaling the results to PSD.

As such, the windowing process is the multiplication of the data by some window shape such as Hanning, rectangular or Blackman window, among others. If the waveform is simply truncated and no shaping is performed, than the window shape is rectangular. The process of selecting the appropriate window depends on what spectral features are of interest, however often the most appropriate window is selected by trial and error [92].

Therefore, the time series x_j is multiplied with a window of length N, which is defined by a vector of real numbers {w_j}, j = 0…N-1. The DFT input is $x_j^{'} = x_j.w_j$.

The DFT output, a complex vector y_m of length N/2+1, is converted into a PSD as follows:

$$PSD = \frac{2 \cdot |y_m|^2}{f_s \cdot s_2} \tag{5.2}$$

Where f_s is the sampling frequency and, for normalization purposes, the squared sum of the window value w_j is used to prevent redundant results for negative frequencies [92]:

$$s_2 = \sum_{j=0}^{N-1} w_j^2 \tag{5.3}$$

5.1.2 The Welch method

The results from power spectrum with DFT are still 'noisy'. Therefore, in order to reduce the standard deviation there is a need to average the result. To do so, that averaging should be done with the PSD. In conjunction with the use of window functions, this method of averaging several spectra is known as 'Welch's methods of averaging modified periodogram's.

As such, a periodogram means the DFT of one segment of the time series, while modified refers to the application of a time-domain window function. Finally, averaging is used to reduce the variance of the spectral estimates which is achieved by dividing the waveform into a number of segments, possibly overlapping, followed by the evaluation of the FT on each segment. The final spectrum is therefore taken from an average of the FT obtained from the various segments [92][93].

This method is attributed to Welch and is also known under various acronyms such as WOSA ('Welch Overlapped Segmented Average') [93].

In the Welch approach, overlapping segments are used and a window is applied to each segment [92]. If there is no overlap, each segment of length N is processed by DFT with a window function, as illustrated in Figure 5.1.

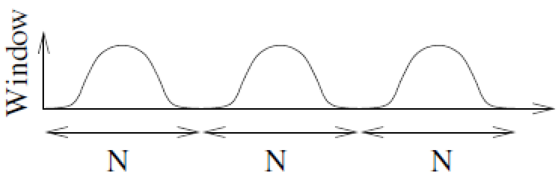

Figure 5.1 - Segmented data stream with window and no overlap [from. [93]]

However, this means that a significant portion of the signal is overlooked, as the window function is typically very small or zero near its boundaries. To avoid the loss of information, the segments should overlap as depicted in Figure 5.2 [93].

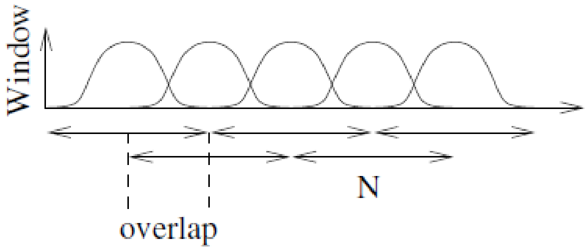

Figure 5.2 - Segmented data stream with window and overlap [from. [93]]

Average periodograms obtained from noisy data traditionally average spectra with segments that overlap by 50%. Higher amounts of overlap, such as maximum overlaps, which means shifting over by just a single sample to get the new segment, are recommended when computing time is not a factor [92].

As such, the original signal is split into L data segments of length M, overlapping by D points. The overlapping data segments are defined as

$$x_m(n) = x(n+mD)\text{, n=0,1,…,L-1; m=0,1,…,k-1} \tag{5.4}$$

The data segments are then windowed:

$$P_{PER}^{m}(f) = \frac{1}{LU}\left|\sum_{n=0}^{L-1} x_m(n)w(n)e^{-j2\pi fn}\right|^2 \tag{5.5}$$

Where

$$U = \frac{1}{M}\sum_{n=0}^{M-1} w^2(n) \tag{5.6}$$

Finally, the Welch spectrum estimate is the average of these modified periodograms,

$$P_w(f) = \frac{1}{K}\sum_{m=0}^{K-1} P_{PER}^{(m)}(f) \tag{5.7}$$

where K is the number of overlapping segments.

With this method a long set of data is required in order to have a good resolution and due to windowing, it suffers leakage thus making it difficult to find weak signals in the data. [92][94].

5.2 Power Spectra and Power Spectral Densities

The Power Spectral Density (V^2/Hz) describes how the signal power varies along the frequency axes. Its main feature is that accumulative sum (cumsum) equals the energy in a band. The cumsum has been used as an important signal feature and will be implemented for each PSD estimate parametric and non-parametric.

The Power Spectrum (V^2) is a useful plot to represent the narrowband individual components power. For instance, if a signal is composed by two sine waves with amplitudes of 2V and 4V the PS will show peak power amplitudes of 4W and 16W. However, if one is interested in estimate the peak amplitudes instead of power the Linear Spectrum (V) should be used instead.

In turn, the Linear Spectral Density ($V/\sqrt{Hz}$) is used to determine the level of the noise in the signal.

The PSD can be converted into a Power Spectrum (PS), Linear Density Spectrum (LDS) or Linear Spectrum (LS) as follows:

Table 5.1 - Naming convention [from. [93]]

Abbrev.	Name	Relation	Unit
PSD	Power Spectral Density		V^2/Hz
PS	Power Spectrum	PS=PSD x ENBW	V^2
LSD	Linear Spectral Density	LSD = $LSD = \sqrt{PSD}$	$V/\sqrt{Hz}$
LS	Linear Spectrum	$LS = \sqrt{PS} = LSD \times \sqrt{ENBW}$	V

As seen on the table above the relationship between estimates of power spectra and power spectral densities is given by the Effective Noise-Equivalent Bandwidth (ENBW):

$$ENBW = fs \frac{s_2}{(s_1)^2} \tag{5.8}$$

where s_1, the sum of the window value w_j is defined in the following manner:

$$s_1 = \sum_{j=0}^{N-1} w_j \tag{5.9}$$

5.3 Power Spectral Density with Parametric Methods

Parametric methods make use of linear processes to estimate the signal spectrum. As depicted on Figure 5.3, the linear process is assumed to be driven by white noise, which contains equal energy at all frequencies and thus making its spectrum constant over all frequencies. Thus, the output is compared with the input waveform and the model parameters adjusted for the best match between model output and the waveform of interest. When the best match is obtained, the model's frequency characteristics provide the best estimate of the waveform's spectrum, given the model constrains. This happens because the input to the model is spectrally flat so that the spectrum at the output is a direct reflection of the model's magnitude transfer function which reflects the input spectrum [92].

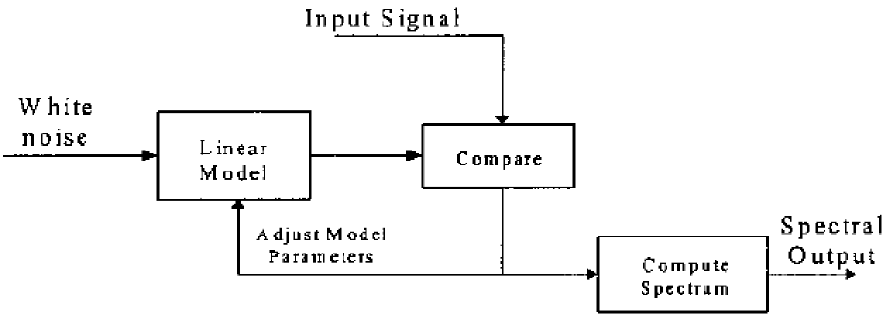

Figure 5.3 - Schematic representation of model-based methods of spectral estimation [from.[92]]

Parametric methods both resolution and fidelity strongly depend on model selection.

Three models are used in this approach, differentiated by the nature of their transfer functions: Autoregressive (AR), Moving Average (MA) and Autoregressive Moving Average (ARMA) [92].

After selecting the model, the next step is to estimate the model parameters for a given data and finally estimating the signal spectrum by using the estimated parameters.

Therefore, the signal x_n is viewed as a response of a linear time-invariant filter to an input v_n. The purpose of the parametric models is to find the filter H(z) and the input v_n that make the output 'as close as possible' to x_n.(Figure 5.4) Being H(Z):

$$H(z) = \frac{B_q(Z)}{A_p(Z)} = \frac{\sum_{k=0}^{q} b_k z^{-k}}{1 + \sum_{k=1}^{p} a_k z^{-k}} \qquad (5.11)$$

Where the a_k and b_k represent the filter coefficients [95].

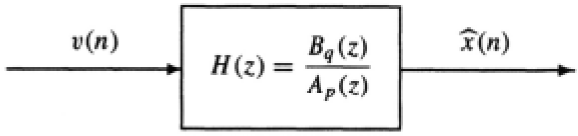

Figure 5.4 - Signal modeling [from. [95]]

The model used in this work, the AR model, the only implemented in the MATLAB signal processing Toolbox, is useful for estimating spectra that have sharp peaks but no deep valleys, being the most popular parametric method as it obtains very precise estimations of AR parameters even for a small number of samples [92][96].

Its transfer function has only a constant in the numerator and a polynomial in the denominator. It is represented by the following time domain equation:

$$y(n) = -\sum_{k=1}^{q} a(k)y(n-k) + u(n) \tag{5.12}$$

Where u(n) is the input or noise function and p is the model order. The output is obtained by convolving the model weight function a(k), with past versions of the output (y(n-k)).

As for the other models: the MA model is useful for evaluating spectra with valleys but no sharp peaks and the ARMA is a combination of the two former methods and is used when the spectrum is likely to contain bold sharp peaks and valleys. Furthermore, the existent algorithms to estimate the MA and ARMA parameters are less plentiful when compared to those existent for estimating AR parameters. Also, these algorithms involve significant computation and are not guaranteed to converge, or may converge to the wrong solution. Moreover, most ARMA methods estimate de AR and MA parameters separately, instead of jointly, as required for optimal solution, and MA approach cannot model narrowband spectra well, as it is not a high-resolution spectral estimator [92].

The PSD of the AR method can be estimated as:

$$PSD_{AR}(f) = \frac{\sigma_e^2}{\left|1 + a_1(n)e^{-j2\pi\Delta t} + \ldots + a_M(n)e^{-jM2\pi\Delta t}\right|^2} \tag{5.13}$$

Where σ_e^2 is the constant noise power, f the frequency and Δt the sampling interval. Since σ_e^2 is a constant the only values that are needed for calculating the shape of the PSD function are the so-called prediction coefficients, a_m [97].

In addition to model type selection, it is also necessary to select the model order. If the model order is too small, the spectrum will be highly smoothed and lack resolution. If the model order is too high, false peaks from an abundant amount of poles begin to appear. As such, the general approach is based around the concept that model order should be sufficient to allow the model spectrum to fit the signal spectrum, but not to large that it begins fitting the noise as well. In many cases, model order is derived on a trial and error basis.

There are a number of different approaches for estimating the AR model coefficients and related power spectrum directly from the waveform. The most known are: the Yule-Walker, the Burg, the covariance and the modified covariance methods, all of them are implemented in the MATLAB Signal Processing Toolbox. Choosing the appropriate method depends on the expected (or desired) shape of the spectrum, since the different methods theoretically enhance different spectral characteristics.

The goal of this thesis is only to test the results of the mentioned methods, and not to describe them which itself would be a thesis. Therefore, the methods vantages and disadvantages are discussed bellow.

- **Yule-Walker Method**

The Yule-Walker method is thought to produce spectra with the least resolution and has a relatively poor performance for short data records. Also, has a very large bias.

On the other hand, it provides the most smoothing spectra and small variance, as well as good performance for large data records when compared to other methods [92][98][99].

- **Burg Method**

It is superior to the Yule-Walker method for short data records, producing a stable model. However, the accuracy of the Burg method is lower for high order models, long data records and high signal-to-noise ratios, which can cause line splitting, or the generation of extraneous peaks in the spectrum estimates. Moreover, the PSD estimation is susceptible to frequency shifts (relative to the true frequency) resulting from the initial phase of noisy sinusoidal signals [94][98].

- **Covariance Method**

For short data records, the covariance method generally produces good resolution spectrum estimates. However, may produce unstable models and frequency bias when estimating sinusoids with noise [95][97][98].

- **Modified Covariance Method**

It is an improvement on both the covariance methods and the Burg method as it does not suffer from spectral line splitting and provides much less distortion compared to the other mentioned methods. Also, this method produces the sharpest peaks, which is useful for identifying sinusoidal components in the signal. However, it is computationally demanding, may produce unstable models and has a minor frequency bias for estimates of sinusoids with noise [92][98].

- **Least-squares method**

This method is very similar to the covariance method. Therefore, produces sharp peaks, it does not suffer from line splitting and has good spectral fidelity for short data series. However, it should be used with caution as it may produce unstable models [98][100].

5.4 Windowing

The FFT assumes that the signal is periodic. However, if the signal is not a multiple of the frequency resolution, width of one frequency bin, the FFT will see a discontinuity between the last sample and the first sample due to the cyclic continuation which results in leakage on the frequency spectrum of the data [93].

Leakage in the frequency spectrum translates in a more disperse signal energy instead of a narrow frequency range as expected. The frequency peak widens, losing amplitude. This disperse shape makes it more difficult to identify the frequency content of the measured signal. In Figure 5.5, the sine wave (top, left plot) has a discontinuity between its first and last sample. As such, there is leakage in the power spectrum, resulting in a wide peak (bottom, blue). However, if a window is applied to the same signal (top, right plot) the power spectrum yields a narrower peak (bottom, red). It is in a dB scale to highlight the shape of the spectrum at low levels [101].

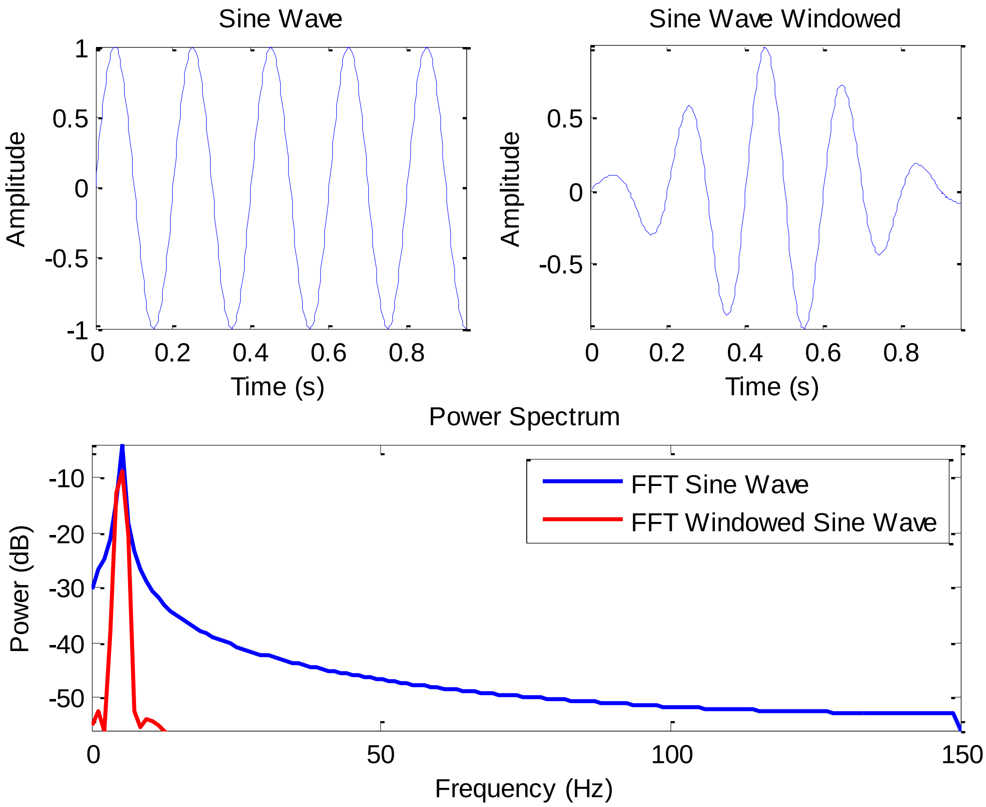

Figure 5.5 – Leakage in the power spectrum: The discontinuation between the first and last value of the sinusoidal signal (top plot, left) results in leakage in the power spectrum (bottom plot, blue). However, if a window is applied to the same signal (top plot, right), the power spectrum yields a narrower peak

As such, before computing the power spectra, the signal should be multiplied by a window function in the time domain. Some window functions are zero at the beginning and end, having a special shape in between. When multiplied by the signal, forces the signal to be periodic, thus removing the discontinuity [93][101].

Using a window function involves a compromise, between the width of the resulting peak in the frequency domain and the amplitude accuracy as well as the rate of decrease of the spectral leakage into other frequency beans [93]. Thus, a special weighting factor must be applied to recover the correct signal amplitude after the windowing [101].

Windows have advantages and disadvantages: some improve the frequency resolution, making easy to detect the exact frequency of a peak in the spectrum, others improve amplitude accuracy, i.e., indicate more accurately the level of the peak [101]. A comparison between the different window functions regarding frequency resolution, spectral leakage and amplitude accuracy, can be seen bellow, Table 5.2.

Table 5.2 - Comparison between window functions [from. [101]]

Window	Frequency Resolution	Spectral Leakage	Amplitude Accuracy
Barlett	Good	Fair	Fair
Blackman	Poor	Best	Good
Flat Top	Poor	Good	Best
Hanning	Good	Good	Fair
Hamming	Good	Fair	Fair
Rectangular	Best	Poor	Poor

5.5 Bandwidth

The signal bandwidth, Hertz, refers to the frequency range in which the signal's spectral density (V^2/Hz) is nonzero or above a small threshold value. The threshold value is often defined relative to the maximum value, most commonly the 3dB-point, which is the point where the spectral density is half its maximum value, or the power spectra (V) is more than 70.7% of its maximum [102].

As such, the bandwidth is the difference between the lower and upper frequencies (f_1 and f_2, Figure 5.6), in which the amplitude drops 3dB. The center frequency (f_0, Figure 5.6) is the geometric mean of f_1 and f_2 [103].

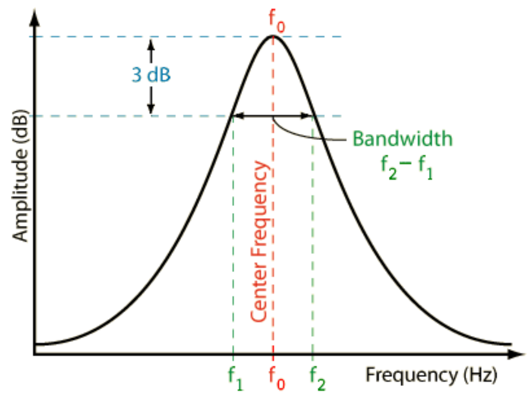

Figure 5.6 – Ilustration of the concept of -3dB bandwidth: the lower and upper frequency (f1 and f2, respectivelly) are the frequencies in which the signals amplitude drops 3dB. The center frequency is the geometric mean of f1 and f2 and the bandwidth is f1-f2 [from.[103]].

However, if a signal is multicomponent, i.e., has several components and more than one frequency, the bandwidth cannot be determined with the above method. The EHG signal has components with several frequencies. Therefore, the bandwidth was defined as follows:

In the case of the parametric and non-parametric methods the lower and upper frequency contains a selected percentage of the total energy of the signal, in this case 75%. This is achieved with the MATLAB function obw (occupied bandwidth), which according to the MATLAB help [104], obw computes a power spectral density estimate, using a periodogram and a Kaiser window. Afterwards, the PSD is integrated with a rectangular approximation. The bandwidth is computed from the frequency intercepts where the integrated power crosses 12.5% and 87.5% of the total power in the spectrum, in the case of 75% of occupied bandwidth.

The lower, central and upper frequency in the marginal are determined with a different method, with the locfreq of the Time-Frequency Toolbox, which determines both average frequency (f_m), central frequency and frequency spreading (B), lower and upper frequency bandwidth, as follows:

$$f_m = \frac{1}{E_x} \int_{-\infty}^{+\infty} \nu \left| \mathrm{X}(\nu) \right|^2 d\nu \text{ [Hz]} \tag{6.3}$$

$$B = 2\sqrt{\frac{\pi}{E_x} \int_{-\infty}^{+\infty} (\upsilon - f_m)^2 \left| \mathrm{X}(\nu) \right|^2 d\nu} \text{ [Hz]} \tag{6.4}$$

where E_x is the energy of the signal and $\mathrm{X}(\nu)$ the Fourier Transform of x(t) [105].

5.6 Comparing Methods

The routine, psd_ehg_estimation_v18_for_general_use, was developed on MATLAB for the Spectral Estimation, with the following command line:

```
psd_ehg_estimation_v18_for_general_use(signal,fs,model_order,window_ty
pe,window_length, nfft, overlap_sample,...
    power_percentage, title_patient,component_name )
```

The parameters to be introduced in this routine are described on the table below:

Table 5.3 - psd_ehg_estimation_v18_for_general_use function inputs

Signal	Input vector
Fs	Sampling Frequency
model_order	Order of the parametric methods
window_type	Window to be multiplied by the whole signal in the parametric methods and non-parametric methods.
window_length	Length of the window used in the Welch method. In the other methods the length of the window is the length of the signal.
Nfft	Eventual zero padding to be applied in the FFT calculations.
overlap_sample	Window overlap to be used in the Welch method.
power_percentage	Power percentage for bandwidth calculation.
title_patient	Comment to be introduced freely by the user. It will be plotted in the figure headers.
component_name	Name of the selected component. It will be plotted in the figure headers.

A small segment of an EHG signal, contraction was introduced in the psd_ehg_estimation_v18_for_general_use with: fs= 4 Hz, model order 30, hanning window with the same size as the signal and nfft of 256.

The results are illustrated bellow, Figure 5.7 and Figure 5.8. The non-parametric methods yield better resolution, i.e., sharper peaks, identifying more frequency peaks (red triangles). The main drawback is there are a lot of small peaks, spurious peaks, which despite being also marked with red triangles have no significant contribution to the signal power.

In turn, parametric methods yield a much smoother spectrum compared to the spectrum obtained with non-parametric methods. However, the frequency peaks are not very sharp, resolution is moderate, and also identifies less frequency peaks (red triangles).

The Wavelet marginal of the uterine component is performed and displayed on top (Figure 5.7). Like the other methods, has the red triangles signalizing the main frequencies peaks and, in this case, the results are more similar to those obtained with the non-parametric methods.

The cumulative sum, i.e., the sum of the area under the PSD curve can be seen on Figure 5.7 next to each PSD graph. The cumsum is almost linear until 0.3Hz, showing that there are numerous energetic frequency peaks contributing to the signal's power. From 0.3 Hz to 0.4Hz there is a region in the cumsum that is almost flat, which means that there is no significant increase in the signal's power. From 0.4 Hz until 0.5 Hz, there is a slight increase in the signal's power, as in that region there are some energetic frequency peaks.

Furthermore, the last cumsum value (total area) should match the energy of the component. The cumsum curve is also a component feature that can be used for classification.

Also, on Figure 5.7 in each spectrum there are three bars: two blue bars representing the lower and upper frequency and a third bar, red, in the middle, the central frequency. Therefore, the signal's frequency bands are determined as follows: [lower frequency-upper frequency].

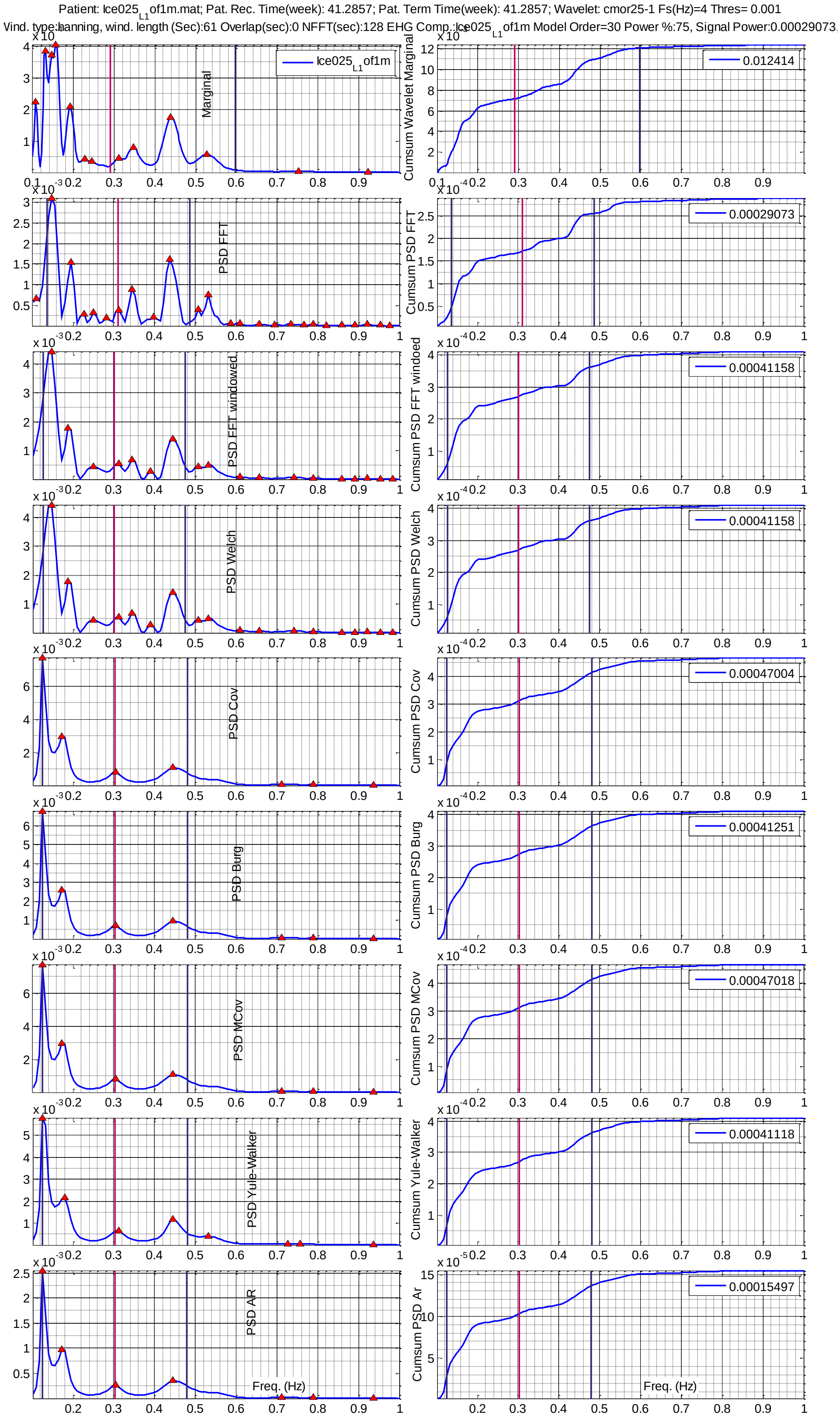

Figure 5.7 - Power spectral estimation of a selected component using the following non-parametric methods: FFT, Windowed FFT, Welch and the parametric methods with model order 30: Covariance, Burg, Modified Covariance, Yule-Walker (left) and the power cumulative sum of each method (right)

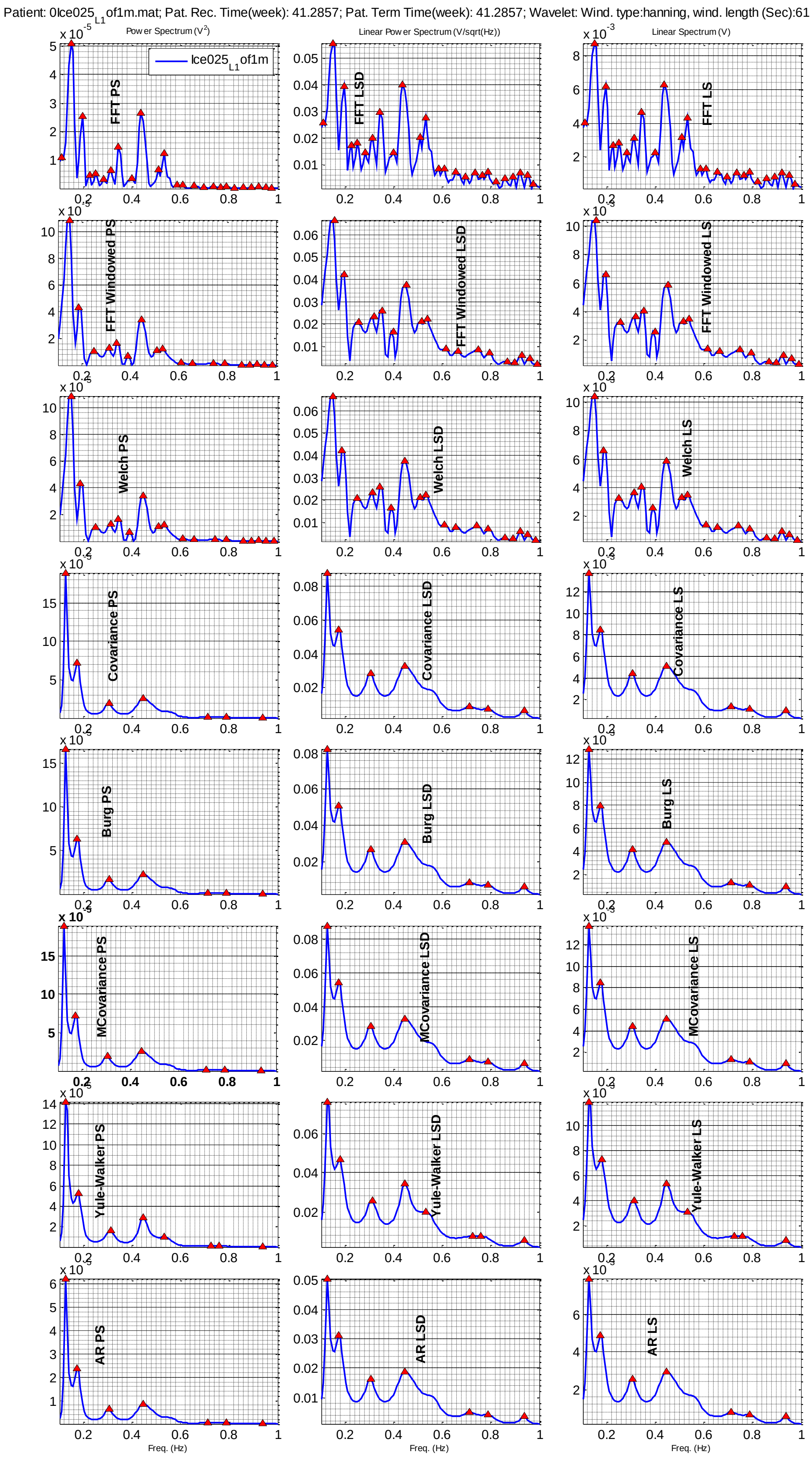

Figure 5.8 - PS methods (left), LSD (middle) and LS (right) of a selected component, using the following non-parametric methods: FFT, Windowed FFT, Welch and the parametric methods with model order 30: Covariance, Burg, Modified Covariance and Yule-Walker

5.7 Energy Estimation

5.7.1 Energy, Power and Root Mean Square

A signal can be defined as a function of varying amplitude through time, so a good measure of strength of a signal is the area under the curve, which is called energy, and since the signal may have a negative part, it is squared, being the energy the area under the squared signal. Power is the energy per unit of time, which can be very useful when the energy of the signal goes to infinity [106].

Considering a continuous-time signal x(t), the energy of this signal over an infinitive interval is given by:

$$E_x = \int_{-\infty}^{\infty} |x(t)|^2 dt \text{ [J]} \tag{5.14}$$

The energy of a discrete time signal is as follows:

$$E_x = \sum_{n=-ƛ-\infty}^{\infty} |x[n]|^2 \text{ [J]} \tag{5.15}$$

The Time-Averaged Power over an infinitive integral is:

$$P_{avx} = \frac{1}{T} \int_{-T/2}^{T/2} |x(t)|^2 dt \text{ [W]} \tag{5.16}$$

If the signal is discrete [107]:

$$P_{avx} = \lim_{N\to\infty} \frac{1}{2N+1} \sum_{n=-N}^{N} |x[n]|^2 \text{ [W]} \tag{5.17}$$

Since the power is proportional to the signal squared, this Time-Averaged Power corresponds to a mean value of the squared signal. As such, the square root of the Time-Averaged Power is the Root Mean Square value (RMS-value):

$$x_{rms} = \sqrt{P_{avx}} \text{ [V]} \tag{5.18}$$

In Figure 5.9, there is the EHG signal, the RMS value and time-average power of the correspondent EHG signals. Like the TOCO, both RMS value and the time-average power appear to be good energy estimators, detecting all the changes in energy relative to the contractions.

5.7.2 Teager Operator

The Teager energy operator (TE) [108] is an estimator of energy and is used to estimate the IUP. Therefore, the TE operator can be used to determine the frequency-weighed energy of the EHG signal, which resembles the mechanical process of myometrial contraction, with a reduced computational complexity.

As such, the application of the TE operator, Φ, in the continuous domain, to an input signal x(t) is given by:

$$\Phi[x(t)] = \left(\frac{dx(t)}{dt}\right)^2 - x(t)\frac{d^2x(t)}{dt^2} \tag{5.19}$$

In the discrete domain, TE operator becomes

$$\Phi[x(n)] = x(n)^2 - x(n-1)x(n+1) \tag{5.20}$$

where n indicates the index of the sample in x.

As it can be seen in equation (5.20), $\Phi[x(n)]$ only spans three consecutive samples of x to calculate the energy at time n, yielding an excellent time resolution. Other advantage is that the TE is robust to white noise and is very suitable for detection of transients in noisy signals.

However, the TE operator is not linear when superimposing two or more signals, which results in an underestimation of the total signal energy. Therefore, in order to calculate an exact energy using the TE operator, the various frequency components of the analyzed signal need to be separated before energy calculation. This is not a problem in the case of the EHG because its energy is concentrated in a limited frequency band, therefore the use of a single TE operator seems a suitable choice [108].

The filtered TE estimator is passed through a comb FIR filter with a duration selected by the user, resulting in the signal seen on Figure 5.9 (sixth plot) which quite well detects all the changes in energy relative to the contractions.

5.8 Crest Factor

Crest Factor (CR) of a waveform is the peak amplitude of the waveform divided by the RMS value of the waveform

$$CR = \frac{|x|_{peak}}{x_{rms}} \tag{5.21}$$

CR shows the ratio of peak values to the effective value. In other words, CR indicates how extreme the peaks are in a waveform. If it is 1 it indicates no peaks, like in direct current. Higher CR indicates peaks. It is a dimensionless quantity. The square of the CR is called **peak-to-average power ratio (PAPR)**.

$$PAPR = \frac{|x|_{peak}^2}{x_{rms}^2} = CR^2 \tag{5.22}$$

When expressed in decibels, CR and PAPR are equivalent [109].

In Figure 5.9, there is the result of the PAPR and CR applied to the EHG signal. The results are very similar, which was expected as the PAPR is expressed in decibels.

The original idea was to be able to detect contractions using the rational that contractions and baseline EHG signal should have different PAPR. However, the obtained results were not conclusive as shown in Figure 5.9. This was so because the sliding window main peak had abrupt variations. A possible solution for this outcome would be to somehow average peaks for each sliding window. It has been left for future work.

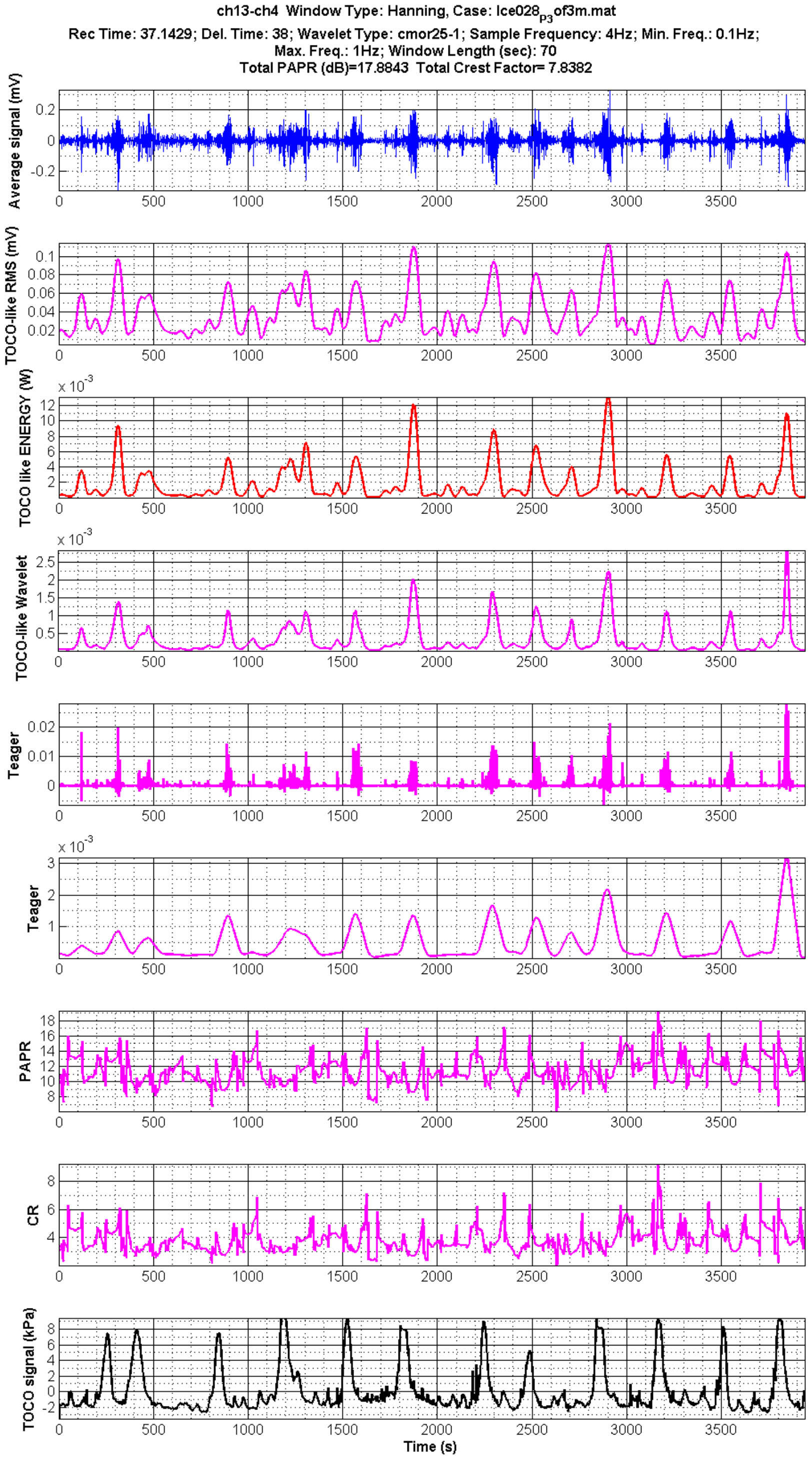

Figure 5.9 – Energy estimation, PAPR and CR of an EHG signal: The EHG signal (top) is followed by those features applied to the EHG signal: RMS-value, Time-average power, Wavelet marginal, Teager operator without filter, filtered Teager operator, PAPR and CR. Original TOCO (bottom). Like the TOCO, the RMS-value, Time-average power, Wavelet marginal and filtered Teager appear to be good energy estimators. The corresponding Tocogram is shown in the last row.

Chapter 6

Methodology

The goal of this thesis is the development of an EHG component database by detecting the following physiological events: Contractions, Alvarez, LDBF and Fetal Movements on the EHG signal.

As such, the components will be isolated and characterized in both time and frequency domains. As well as other parameters such as Root Mean Square, Time-Averaged Power, Teager operator and Crest Factor.

The methodology for the database construction will be explained in detail throughout this chapter, which follows the next steps: Subject Selection, the TOCO annotation, digitalization and synchronization with the EHG signal. Pre-processing of the EHG signal and finally event characterization.

6.1 Subjects Selection

The EHG signal retrieved in the public Icelandic EHG database contains 45 subjects: 41 with term deliveries and 4 with preterm deliveries. Each subject contains one or more records per pregnancy.

For subject selection a scattering plot was made, Figure 5.10, Recording Time vs Delivery Time with the 45 subjects of the Icelandic Database. Each subject is represented by a different color and marker. As it can be seen on the figure, most of the subjects had term deliveries, i.e., are above the delivery time of 38 weeks (blue line).

As such, and since for each selected subject, the correspondent TOCO had to be annotated by a physician, it was agreed that only a few subjects would be selected. Therefore, the subjects were chosen according to their number of records (more than three). The ones that had more than three records and different delivery dates were selected, which resulted in 5 subjects (19 recordings). The selected subjects are marked with an ellipse on the figure bellow.

Afterwards, and because there were very few LDBF contractions in the selected recordings, another 3 subjects (4 recordings), whose mentioned event was found on the recordings, were selected.

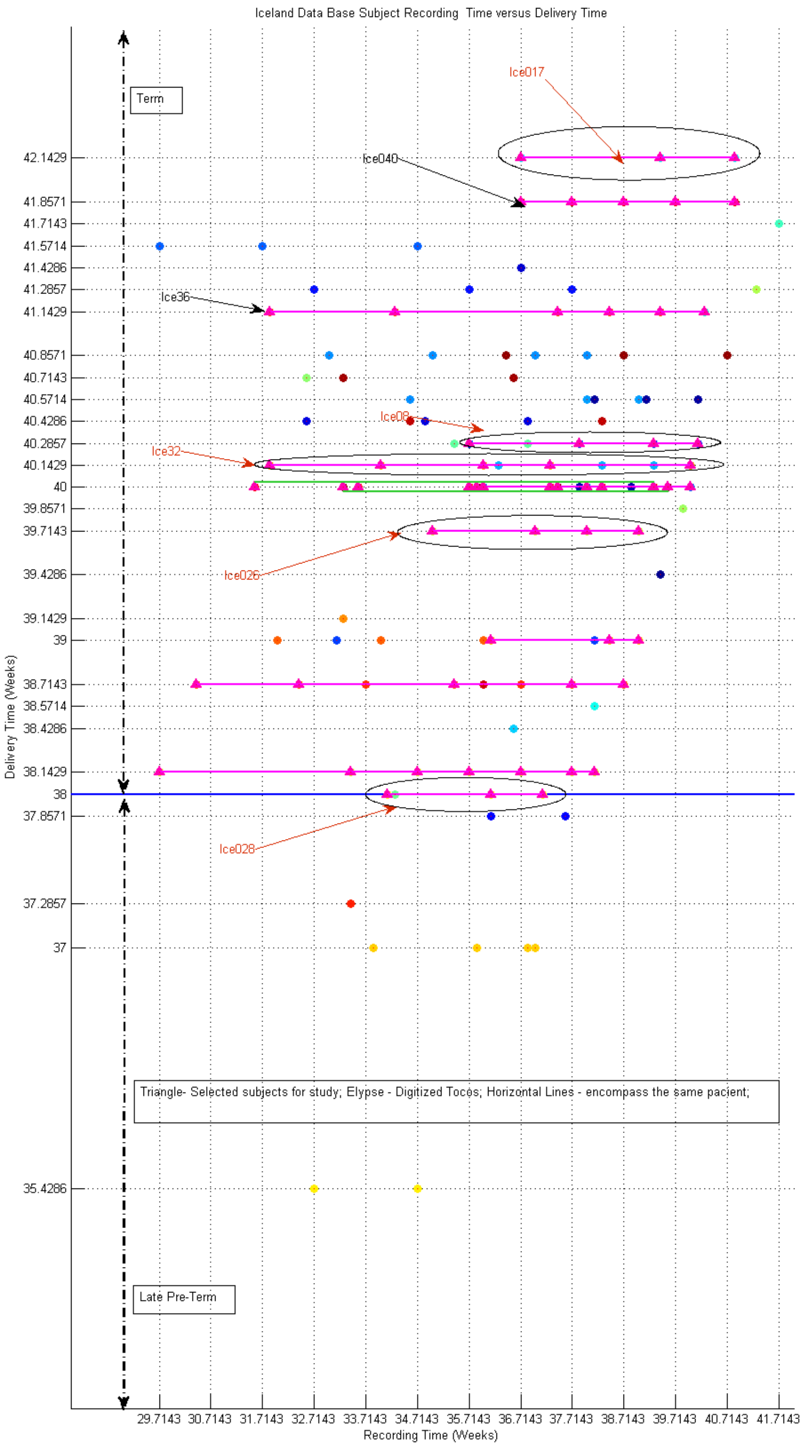

Figure 5.10 – Scattering plot (Delivery Time vs Recording Time) for the 45 subjects of the Iceland Database: each subject represented by a different color and marker. Five subjects were selected (marked with an ellipse)

6.2 TOCO Annotation

Each EHG record has its correspondent TOCO which were analyzed by four Maternidade Alfredo da Costa (MAC) obstetricians\gynecologists for an expert event classification, taken here as the golden standard. As such, the events present in the TOCO were classified as follows:

- **Basal Uterine Activity (BUA) –** It is defined as the intrauterine pressure at rest in between contractions. It can be a flat line as depicted in Figure 5.11 or a more turbulent line, like in Figure 5.13.
- **Uterine Irritability (UI) –** Very small, high frequency waves, it is thought to be Alvarez Waves. It is depicted in Figure 5.12.
- **Low Amplitude Contraction (LAC) –** Uterine contractions of low amplitude in the TOCO. (Figure 5.13).
- **High Amplitude Contraction (HAC) –** Uterine contractions with high amplitude in the TOCO (Figure 5.13)
- **Fetal Movement (FM) –** Usually, in the TOCO, FM are very narrow well defined peaks, as represented in Figure 5.11 and Figure 5.12.
- **Artifact –** Artifacts due to movements of the subject, such as movements due to breathing or changing position, which can resemble an impulse

Expert TOCO annotation is still a very subjective task:

- Some FM are not narrow peaks, and can be misinterpreted as artifacts or UI.
- There is no defined threshold upon which a wave it is considered to be HAC instead of LAC.
- UI is not very clear. At times the difference from the BUA is not evident.

For this reason, the TOCO's were annotated by four different physicians, which yielded sometimes different outcomes (Figure 5.14). Therefore, the common outcomes were selected.

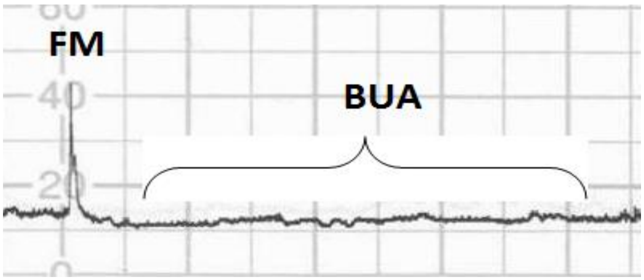

Figure 5.11 - Sample of a TOCO from the Iceland database with the following events classified by four experts at MAC: BUA and FM. Vertical scale: mmHG; horizontal scale: 2 square intervals equals 1 minute

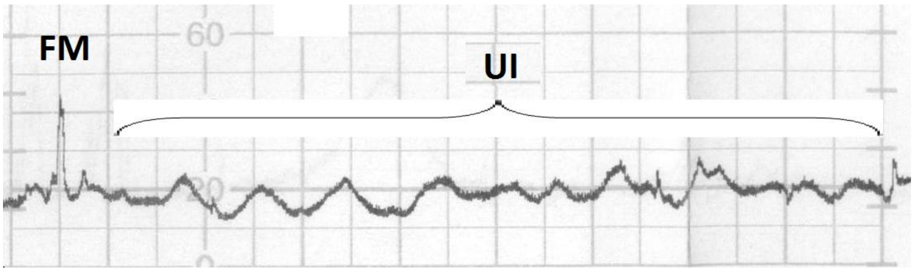

Figure 5.12 - Sample of a TOCO from the Iceland database with the following events classified by four experts at MAC: UI and FM. Vertical scale: mmHG; horizontal scale: 2 square intervals equals 1 minute

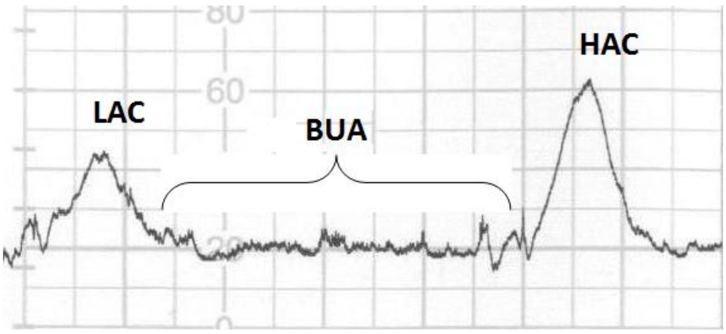

Figure 5.13 - Sample of a TOCO from the Iceland database with the following events classified by four experts at MAC: HAC,BUA and LAC. Vertical scale: mmHG; horizontal scale: 2 square intervals equals 1 minute

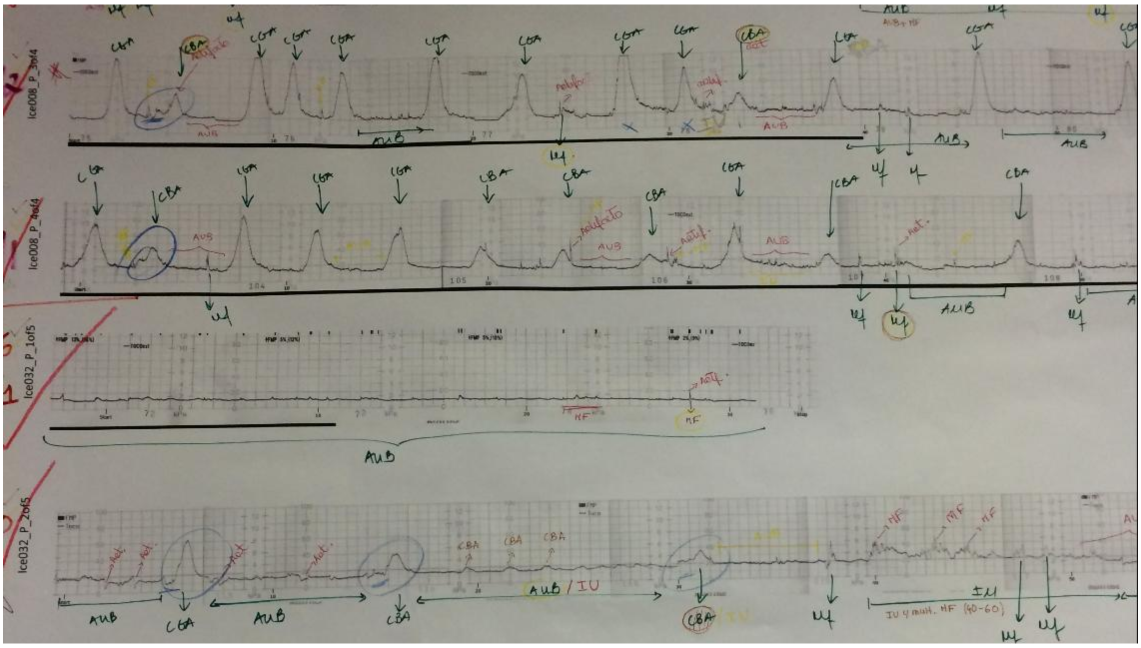

Figure 5.14 - TOCO's annotated by MAC's physicians

6.3 TOCO digitalization and Synchronization with EHG

The TOCO and EHG were acquired on different equipments, which were not synchronized. Consequently, there is a variable time lag between the two signals, which according to the Database publishers it is around 30 seconds.

For this work it was necessary to have the TOCO's digitized. For such, the *GetData Graph Digitizer*® was used, which provided very god results (Figure 5.15). Afterwards, the digitalized signal was interpolated with the *chirp* method [110]. Synchronization was done visually using two independent human scorers, relevant spikes in each signal – fiducial points were obtained.

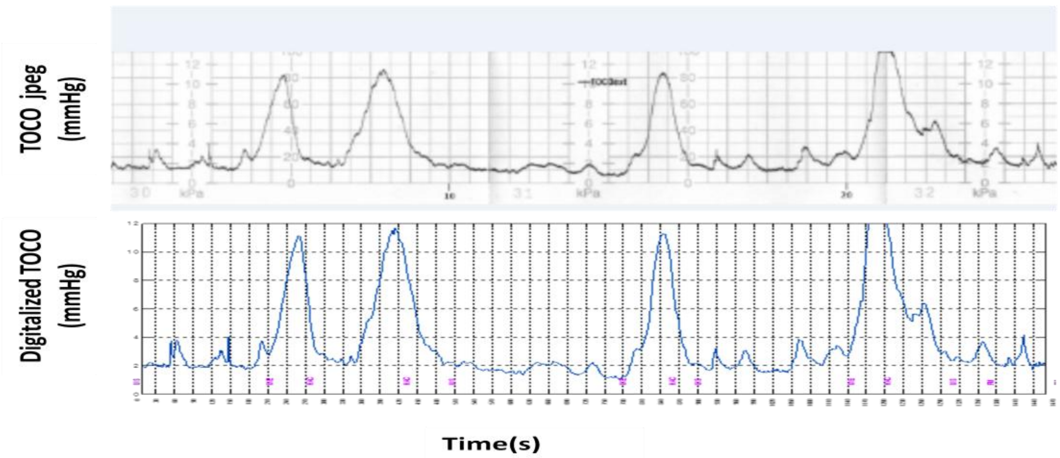

Figure 5.15 – Original TOCO in jpeg (top) and the results of its digitalization with *GetData Graph Digitizer*®. (bottom)

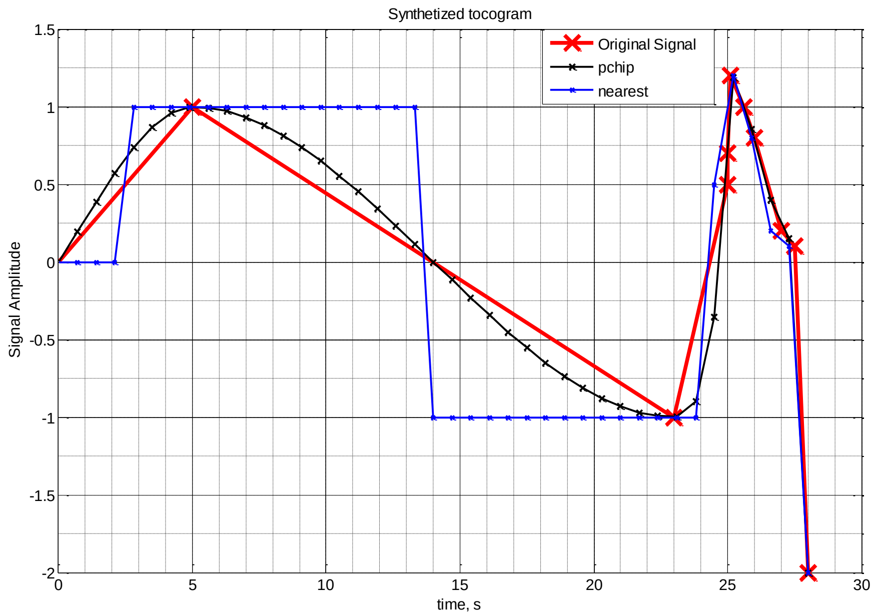

Figure 5.16 – TOCO interpolation methods: The original signal (red) and it's interpolation with both pchirp (black) and nearest (blue) methods. The chirp method provides better results, as it's shape is closer to the original signal.

The following routines (Figure 5.17) were developed for this process:

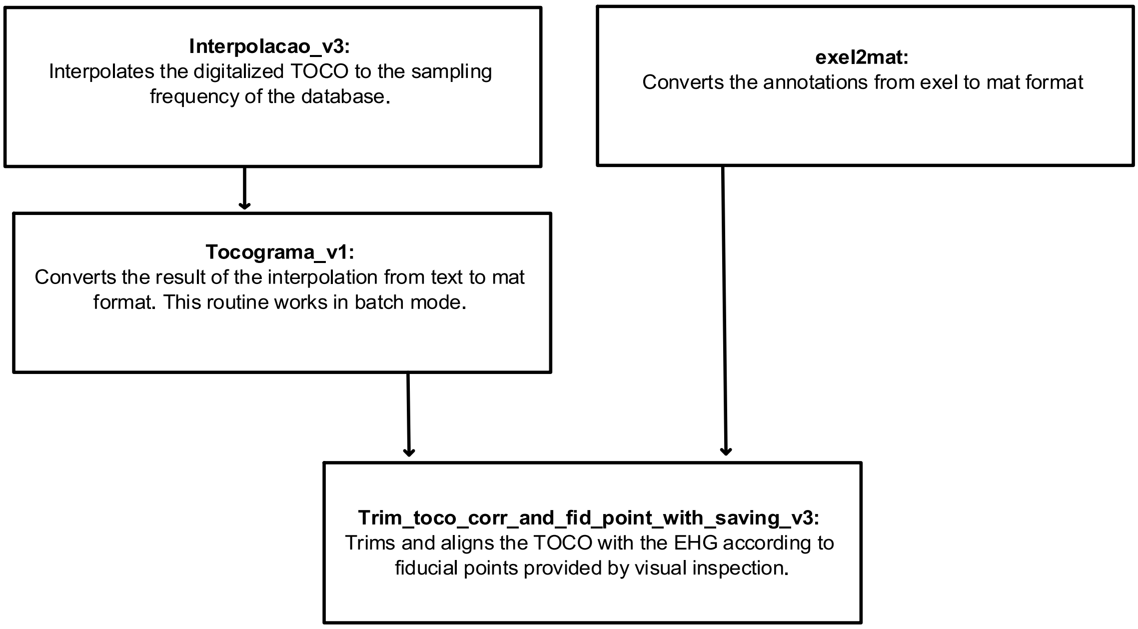

Figure 5.17 - Implemented routines for TOCO-EHG synchronization

The results of the implemented routines can be seen in Figure 5.18. The EHG signal (top plot) synchronizes with the original TOCO signal (middle plot) at the fiducial point (vertical black line) provided by visual inspection. The resulting trimmed TOCO (bottom plot) is zero padded to have the same length as the EHG signal.

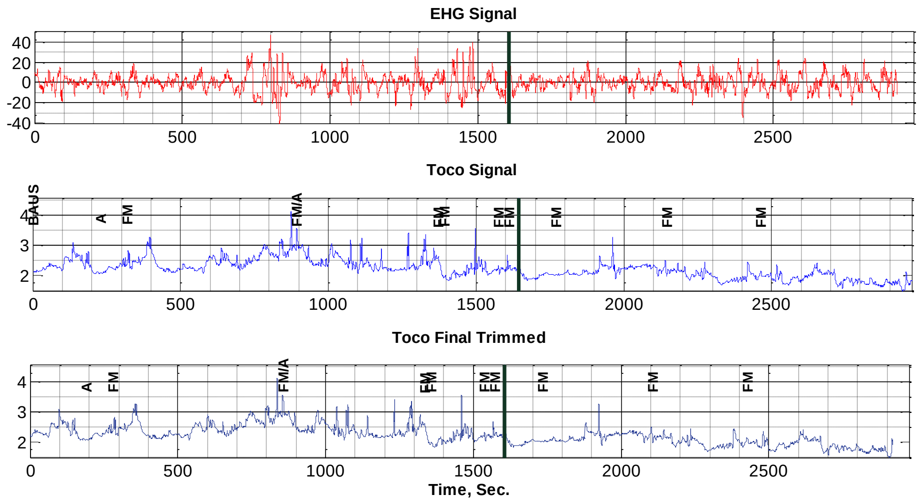

Figure 5.18 - Results of the implemented routines: EHG signal (top plot), original TOCO signal with annotations (middle plot) and TOCO final trimmed with annotations(bottom plot). The black vertical line represents the fiducial point

6.4 Pre-processing

6.4.1 Decimation

The EHG signal, originally with sampling rate of 200Hz and bandwidth of [0-100] Hz, was filtered with a FIR filter to [0-2] Hz and decimated to a new sampling rate of 4 Hz, thus using the decimation factor of 50. This is for computing and data representation efficiency.

6.4.2 Filtering

It was used a Wavelet filter instead of a FIR filter. In Figure 5.19 there are two plots: one with the raw unfiltered EHG signal (top) and other with both the results of the FIR filter (bottom, blue) and Wavelet filter (bottom, red) applied to the EHG signal. As it can be seen on the figure, the Wavelet filter deals better with the abrupt variation seen at the beginning of the signal, which is due to electrode polarization. It also preserves the other signal variations.

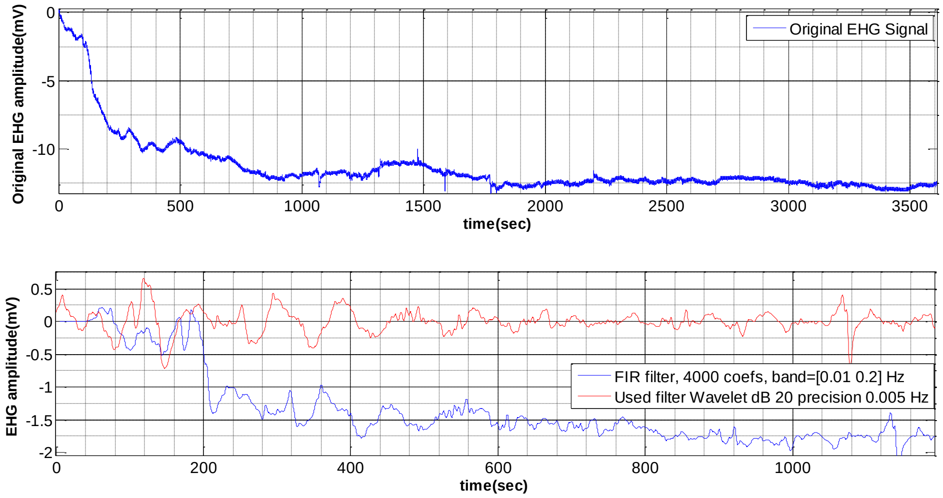

Figure 5.19 – Filtering the EHG signal: Unfiltered raw EHG signal (top). Results of the FIR filter applied to the EHG signal (blue, bottom plot) and results of the Wavelet filter applied to the same EHG signal (red, bottom plot). The Wavelet filter deals better with the abrupt variation seen at the beginning of the signal.

As mentioned on chapter 3, section 3.2.4, EHG components distribute its energy from [0.1–5] Hz, thus not having any significant frequency component outside this frequency band [23][55]. In order to exclude the artifacts and other unwanted components, most authors [62][55][63][64][65][66][67] study the changes occurring in the spectral region from 0.34 to 1.00 Hz, the so called “uterine-dominant” range, thus suppressing the maternal ECG and respiration artifacts.

However, there are components of interest that can be found under the 0.34 Hz spectral region. For that reason, in this thesis the spectral region of interest will be [0.1-1] Hz, which means that the respiration artifact will not be suppressed. Despite this fact, the Iceland Database has the electrodes bellow the umbilicus, meaning that the respiration artifact although not entirely suppressed does not represent a very strong interference.

The filter used the db15 (Daubechies 15), a Wavelet Packet filter, for which the leaves frequency precision was selected to be 0.005 Hz. The frequency band of interest is [0.1-1] Hz.

As such, and as depicted in the figure below, Figure 5.20, the original signal (blue signal) was filtered to [0-2] Hz and decimated, with a decimation factor of 50, which resulted in a new sampling frequency of 4Hz. After decimation, twenty seconds of the raw EHG signal, which corresponded to the abrupt variation seen at the beginning of the raw unfiltered EHG signal, were removed and the first value was subtracted to the whole EHG signal. Finally the filtered EHG signal (black signal) was obtained.

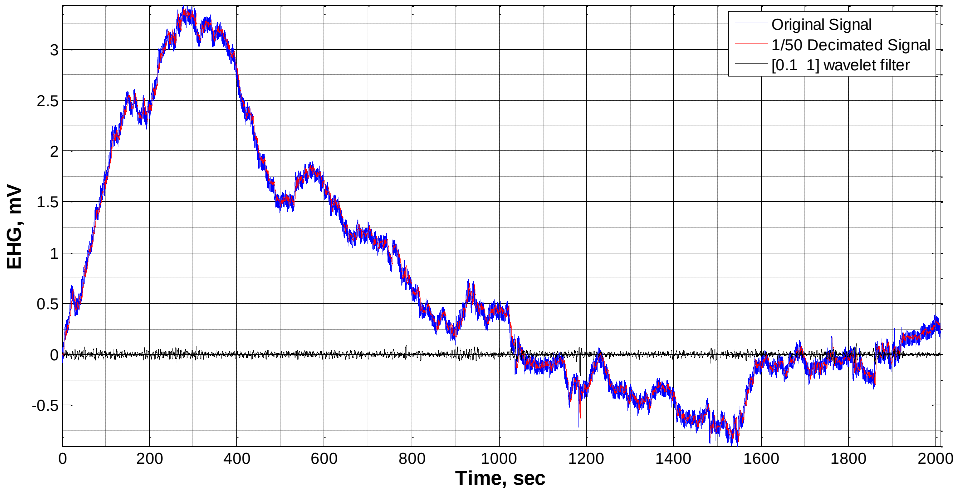

Figure 5.20 – EHG decimation and filtering: The raw unfiltered EHG signal (blue) is decimated by a factor of 50 (red) and filtered (black) to a [0.1-1]Hz frequency band

6.4.3 Bipolar or Monopolar derivation

As mentioned in section 3.2.5 and despite all the disadvantages regarding bipolar derivation, it reduces signal artifacts such as respiration, resulting in a much easier identification of the signal components, therefore being the chosen derivation for the EHG signal analysis. To avoid the loss of important components the electrode distance was as wide as possible.

As depicted in Figure 5.21, the electrode grid has 4x4 electrodes. The four bipolar channels (BP1-BP4) resulted from the differentiation between two monopolar electrodes that had the furthest separation from each other along the horizontal axis. The same was done along the vertical axis (BP5-BP8) and finally, the differentiation between the channels in the electrode configuration that were more distant from each other resulted in two bipolar channels. (BP9 and BP10)

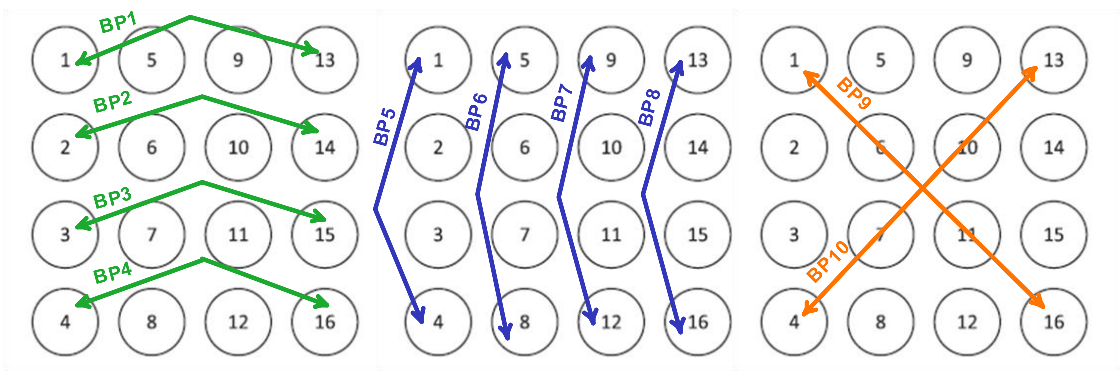

Figure 5.21 - Bipolar channels used on the signal analysis: four with the differentiation along the horizontal axis (BP1-BP4), vertical axis (BP5-BP8) and diagonal (BP9 and BP10)

6.5 Event Characterization

In the scheme bellow, Figure 5.22, it is depicted the steps for event characterization on the *Uterine Explorer*: The final step is the decision of the expert regarding the component classification.

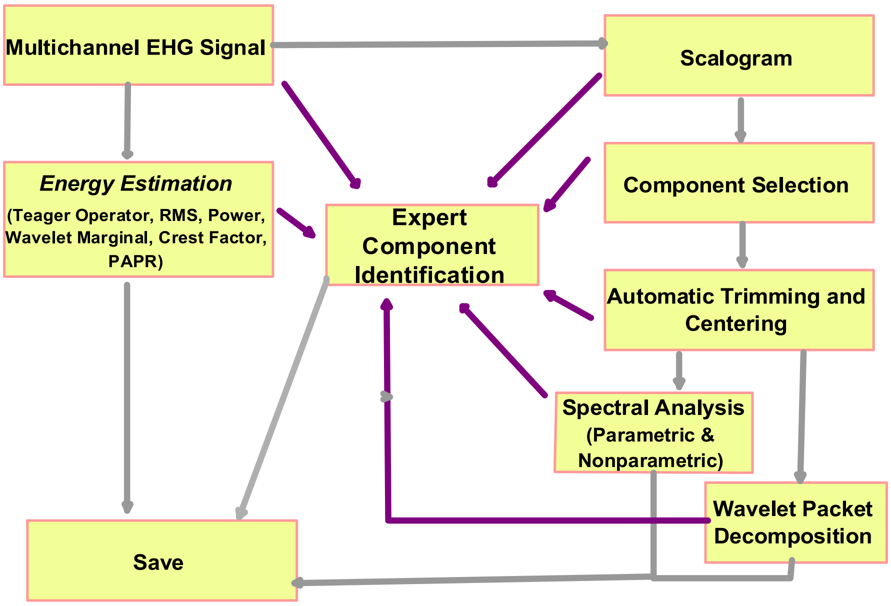

Figure 5.22 - Scheme representing the steps taken in signal analysis

6.5.1 Multichannel EHG Signal

First, the EHG signal is retrieved from the Iceland Database. As already discussed, the signal is analyzed in the bipolar configuration with ten bipolar signals. The electrode montage list is depicted on Figure 5.23.

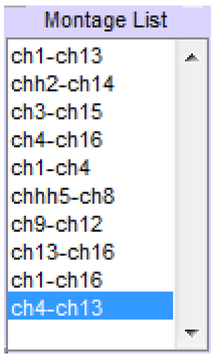

Figure 5.23 - Montage List of the tem bipolar electrodes

6.5.2 Scalogram and Component Selection

A time-frequency analysis of the EHG signal is performed with Scalogram, chosen time-frequency method after the results obtained on chapter 4. The Scalogram is computed with the Wavelet Morlet (cmor25-1), which, upon visual inspection presented the best results, identifying more events relatively to the others tested wavelets.

In Figure 5.24, there is the EHG signal (red signal) of the bipolar channel ch1-ch16, along with the Wavelet marginal (green signal) and the subject's annotations (blue letters). Bellow the EHG signal there is the Scalogram. The selected event, a contraction, can be found between two pink bars.

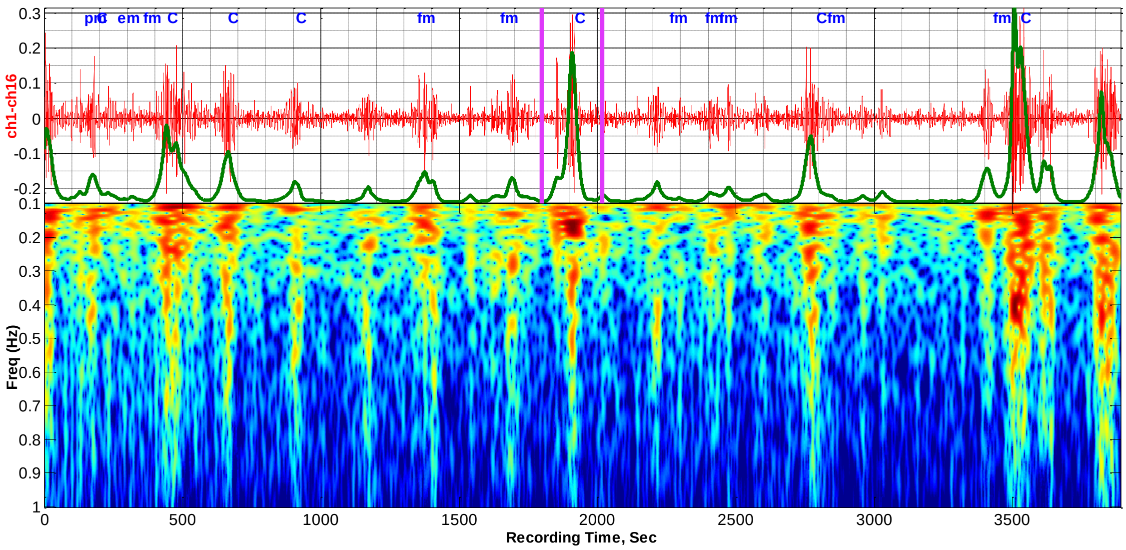

Figure 5.24 – Scalogram and component selection: EHG signal(red, top), Wavelet marginal (green, top) and subject annotations (blue letters, top) with correspondent Scalogram of bipolar channel ch1-ch16 (bottom, top). A contraction was selected on this channel (pink verical bars).

6.5.3 Automatic Trimming and Centering

To reduce subjectivity of manual selection the event is trimmed and centered. The algorithm determines the average time (t_m) of the selected component, in the following manner:

$$t_m = \frac{1}{E_x} \int_{-\infty}^{+\infty} t\left|x(t)\right|^2 dt \ \text{[s]} \tag{6.1}$$

where E_x is the energy of the signal, and x the selected component.

Finally, determines the time spreading of the component:

$$T = 2\sqrt{\frac{\pi}{E_x} \int_{-\infty}^{+\infty} (t - t_m)^2 \left|x(t)\right|^2 dt} \ \text{[s]} \tag{6.2}$$

Where E_x is the energy of the signal, x the selected component and t_m is the averaged time center [105]. Therefore, the selected component is trimmed in the lower and upper time limit of the time spreading band.

The result of the trimming and centering of the selected component can be seen in Figure 5.25, top graph, with the event already trimmed and the averaged time center (green bar).

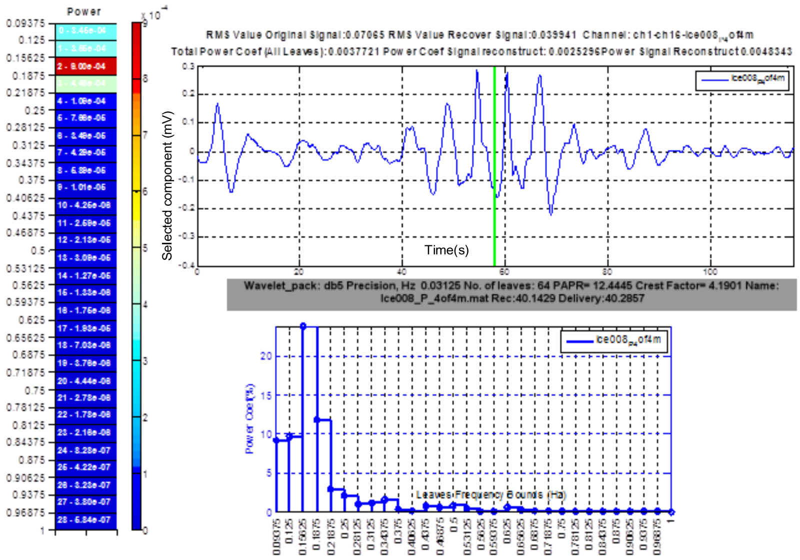

Figure 5.25 – Results of trimming and centering and WPD: Power of each leave in the final level of the WPD tree (left), selected EHG component trimmed and centered (top right) and Power percentage of each leave in the final level WPD tree (bottom right).

6.5.4 Wavelet Packet Decomposition

For the WPD the used mother Wavelet was db5 (Daubechies 5). Therefore, WPD tree has, on the final level, 64 leaves, which since the frequency band of interest is [0.1-1] Hz it is reduced to 29 leaves, each one with a precision of roughly 0.004 Hz. With WPD the user can reconstruct the signal selecting the appropriate leaves of the WPD tree. In this case all the leaves are used. As such, this feature is used to see the power distribution on each leave of the WPD tree, which can be seen on figure Figure 5.25 (left graph). In this case, most of the selected component power is located in the frequency interval [0.15625, 0.1875] Hz, third leave. This is confirmed on the graph Power Coef (%) vs Leaves Frequency Bounds (Hz), which contains the percentage of power on each leave on the final level of the WPD tree.

6.5.5 Spectral Analysis

Afterwards, a spectral analysis with the following non-parametric methods: FFT, Windowed FFT, Welch and the parametric methods: Covariance, Burg, Modified Covariance, Yule-Walker is performed on the selected event. As mentioned on chapter 5 and depicted,

Figure 5.7, each PSD graph has its correspondent cumsum curve (right) as well as the lower and upper frequency bandwidth (blue bars), containing 75% of the component energy as well as the central frequency (red bar). Also, all the signal main frequencies peaks are marked with red triangles.

Moreover, the Wavelet marginal of the selected component is performed and displayed on the top (top, Figure 5.7). Like the other methods, has the red triangles signalizing the main frequency peaks as well as the upper, lower and central frequency.

In Figure 5.8, there is the PS (left), LSD (middle) and LS (right) with both parametric and non-parametric methods used to estimate the PSD. All the main signal frequency peaks are marked with red triangles.

As such, the following decisions were taken:

The window used in all the methods, except in the non-windowed FFT, was the Hanning window with the size of the selected component. In the parametric methods to avoid the loss of spectral resolution the NFFT (number of points in the FFT) is determined as the smallest power of two (p) that satisfies:

$$NFFT = 2^{p} \geq S + 1 \tag{6.3}$$

Where S is the signal length [111].

The parametric methods model order was: Akaike's Information Criterion (aic) and Final Prediction Error (fpe) with four contractions.

FPE and AIC are defined as follows:

$$FPE(q) = \frac{N+q}{N-q} S^{2}(q) = \left[\frac{1+ q/N}{1- q/N} \right] S^{2}(q) \tag{6.4}$$

$$AIC(q) = \ln\left[S^{2}(q)\right] + \frac{2q}{N} \tag{6.5}$$

Where $S^2(q)$ is the variation of the prediction error for the order q and N the number of samples [112].

As depicted on the figure bellow, Figure 5.26, which corresponds to the result obtained from one of the four contractions tested, as the results obtained with the other three contractions are very similar, shows that the model order to be used is 30, since the graph appears to stabilize at that order. The fpe command yielded a very low order, being therefore ignored.

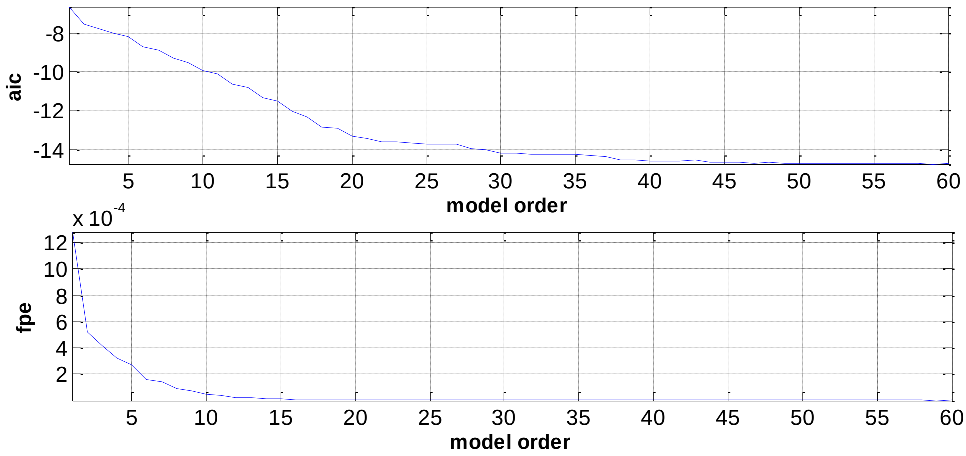

Figure 5.26 - Aic and fpe used on an uterine contraction to select an apropriate model order for spectral analysis with parametric models. The model order 30 was chosen.

6.5.6 Energy Estimation

As mentioned on chapter 5, energy estimation is performed by a Hanning sliding window with 70 seconds length, which is applied to the EHG signal extracting the following features, that can be seen on Figure 5.9: Root Mean Square (Toco-like RMS), Time-Average Power (Toco-like Energy), Teager Operator (Teager), filtered and non-filtered, PAPR and CR of the whole EHG signal. There is also the Wavelet time marginal (Toco-like Wavelet) and the TOCO (TOCO signal).

6.5.7 Saving the data

The results from time-frequency analysis (ehg_component_manually_selected), spectral analysis (spectral_estimation) and energy estimation (ehg_energy) can be retrieved on MATLAB in the header.data which has the structure depicted in Figure 5.26.

Spectral analysis (spectral_estimation) has the following structure:

- **freq_axis_of_wavelet_marginal**, **freq_fft**, **f_cov-** Frequency axes of the: Wavelet frequency marginal, FFT, parametric and Welch methods, of one channel, in which the event was selected.

  freq_axis_of_wavelet_marginal_all, **freq_fft_all**, **f_cov_all** – Contains the above explained for all the channels.
- **psd_matrix** – All the PSD estimations: parametric, non-parametric and Wavelet frequency marginal of the selected component and channel.

  psd_matrix_all – Contains the above explained for all the channels.
- **ps_matrix, ls_matrix, lsd_matrix -** Contains respectively the PS, LSD and LS estimations: parametric, non-parametric of the selected component in the channel in which it was selected.

ps_matrix_all, ls_matrix_all, lsd_matrix_all – Contains the above explained for all the channels.

- **cumsum_matrix** - Cumsum graphs: parametric, non-parametric and Wavelet frequency marginal of the selected channel
  cumsum_matrix_all – Contains the above explained for all the channels.
- **signal_power –** Power of the selected component on the chosen channel
  signal_power_all – Contains the above explained for all the channels.
- **psd_ps_ls_lsd_cumsum_id_string** – Contains the names of the used methods for the PS, LSD and LS estimations in the order of plotting in the chosen channel
  psd_ps_ls_lsd_cumsum_id_string_all - Contains the above explained for all the channels.
- **bw_flo_fhi_energy -** Contains the lower, central and upper limit of the bandwidth for each used method in the chosen channel. **bw_flo_fhi_energy_all –** Contains the above explained for all the channels.
- **locs_peaks_psd_cell, locs_peaks_ps_cell, locs_peaks_lsd_cell and locs_peaks_ls_cell** - Contains the time localization of the frequency peaks detected on each PSD, PS, LSD and LS spectrum in the chosen channel. **locs_peaks_psd_cell_all, locs_peaks_ps_cell_all, locs_peaks_lsd_cell_all and locs_peaks_ls_cell_all** - Contains the above explained for all the channels.
- **id_for_locs_peaks_psd_cell**, **id_for_locs_peaks_ps_lsd_ls_cel** – Contains the id strings of the methods used in the PSD, PS, LSD and LS estimations in the selected channel.
  id_for_locs_peaks_psd_cell_all, **id_for_locs_peaks_ps_lsd_ls_cell_all** - Contains the above explained for all the channels.

Results from energy estimation (spectral_estimation) are organized as follows:

- **window_length_sec, window_selection** – Contains respectively, the information about the chosen window length and its type.
- **channels_name** - Channels id.
- **teager, teager_filtered, rms, rms_squared, wavelet_time_marginal, wavelet_type, time_axis_sec -** Contains the results of the application of following methods in all the channels: Teager, its filtered version, RMS, Time-average power and Wavelet time marginal with the type of Wavelet used, as well as the time axis for the referred methods.
- **papr, cr**, **t_papr_cr_sec, cr_total, papr_total -** PAPR and CR estimations determined with the sliding window with correspondent time axis and the total value of CR and PAPR for each channel.

The results from time-frequency analysis (ehg_energy) are organized as follows:

- **matrix -** the selected component in all channels.

- **time-freq** - Time-Frequency representation of the component in all the channels.

The database has 87Gb of space. Spectral analysis occupies 1.5 Gb of space, the time-frequency representation of the selected component, 6 Gb and 2 Gb for energy estimations. The remaining space is occupied by other features.

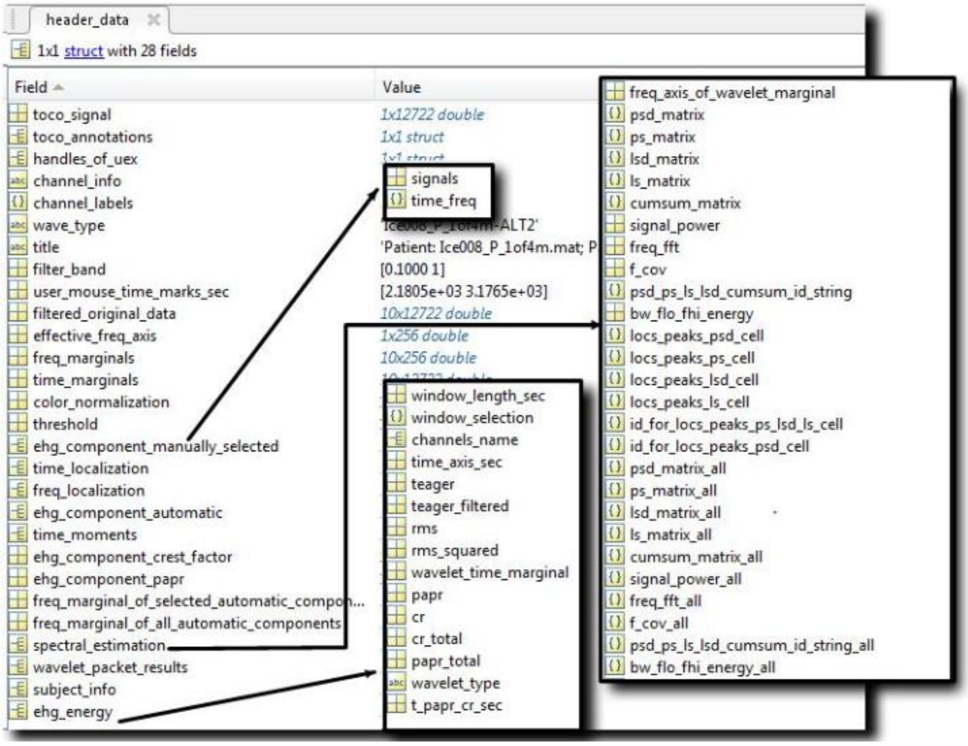

Figure 5.27 - Header.data structure

6.6 Scalogram Color Normalization

Visual component selection necessarily implies a certain degree of subjectivity.

In the time domain, the component offset and onset time are marked by the Wavelet marginal minima. In the frequency domain the color code gives an indication of the energy distribution. However, energy the distribution depends on the EHG signal itself, which varies from channel to channel and across the subject’s database. For instance, a red color for one particular EHG interval in a recording is not equivalent to the same red color on another record. For the visual inspector this is a problem, since the idea is to train the eye to consistently classify the correspondence between the colors and the energy.

As such, it has been decided to normalize the color code to the expected maximum and minimum values of typical EHG wavelet energy signal distribution, for which a number of cases were considered. The limits of 0 and 0.05 mW were agreed upon on. The drawback of this procedure is the fact that some EHG recordings present high amplitude events normally associated with artifacts such as subject movements or equipment related. However, it has been observed that the EHG amplitudes remain consistent throughout the recordings.

Figure 5.28 shows in the upper plot the same contraction (top plot) and respective Scalograms (middle plot), using two different color allocation minimum and maximum values called global TRF Max and Global TRF Min. As it can be seen, the middle plot on the right represents less efficiently the energy distribution along the frequency axis. Some details are missing, this is due to the fact that the high maximum value (0.3) has been allocated to the red color.

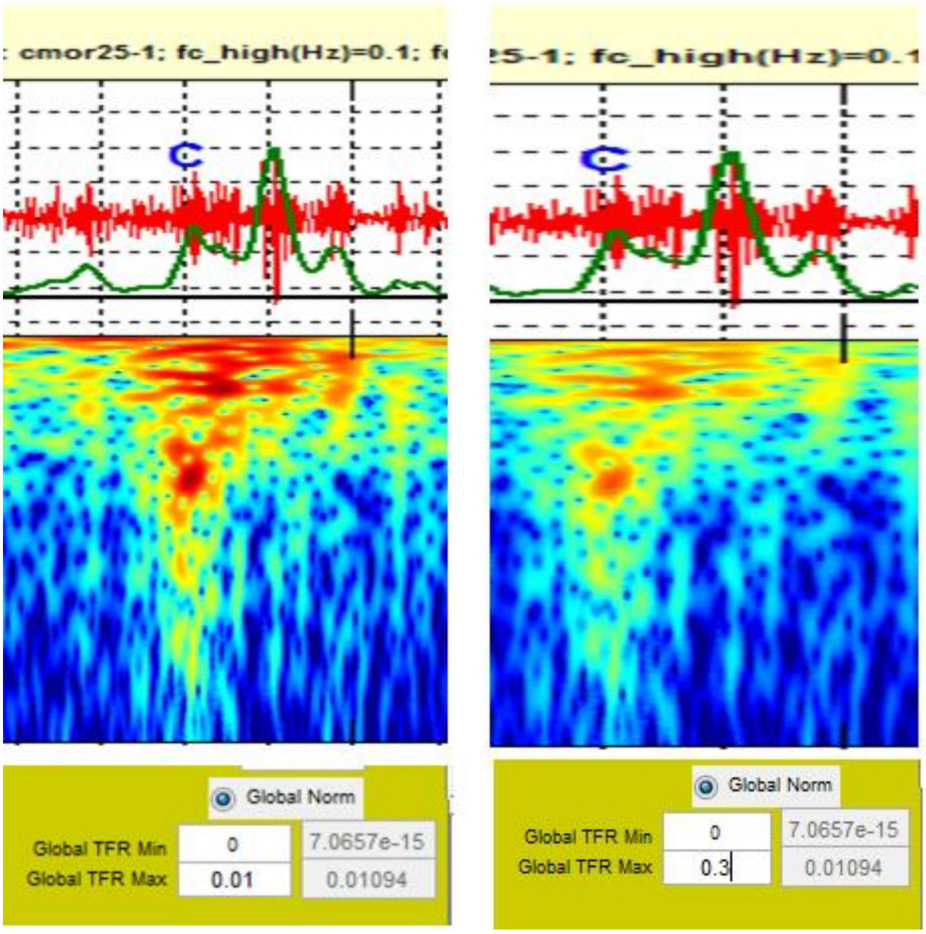

Figure 5.28 – Scalogram color normalization: Contraction (top plot) with correspondent Scalogram (middle plot) with two different color allocation minimum (Global TFR Min) and maximum (Global TFR Max) value. The middle plot on the right represents less efficiency the energy distribution along the frequency axis because the high maximum value (0.3) was allocated to the red color.

Chapter 7

Results

A database with 288 events was constructed where it can be found:

- Alvarez waves
- Contractions
- Early Labor Contractions
- Late Labor Contractions
- Fetal Movements
- LDBF waves
- Fetal Hiccups
- Basal Uterine Activity

For the decision making process not only it was taken into consideration, the frequency and time characteristics of the events but also the TOCO's analyzed by the MAC physicians, as well as the information provided in the Iceland database regarding each subject: BMI, gestational age at recording and delivery, observations.

In this chapter are shown the results obtained from the use of the referred tools: spectral analysis (PSD estimation), time-frequency representation, TOCO's, the provided subjects information and annotations for the characterization of each event above listed with the exception of Basal Uterine Activity, since is the relaxed uterus in between events, it has few spectral and time characteristics of interest.

Often the recognized golden standard reference in bio-signal classification is established by visual inspection of experts. This is the case in sleep scoring via the EEG and other polysomnographic signals. Ideally, more than one expert should intervene, using a blind scoring method. However, frequently the available scorers are limited, and the classification process relies only in an individual expert. In an emergent technique such as the EHG signal processing the available scorers are certainly limited [19][20][21] and there will always be a stage where initial scorers will act in a trial and error procedure. This means that the classification process should be iterative using several cycles, i.e, after a first pass and in view of the parameters obtained, a new classification process should begin. This is obviously a time consuming process and this thesis work is just the first iteration process where the right tools were developed to assist in this process.

7.1 Alvarez Waves

Alvarez waves, also known as uterine irritability or LAHF, are characterized in the literature as high frequency low amplitude waves [13].

The Alvarez train waves detected on the records of the Iceland database all present the same pattern, i.e., a train of waves (usually more than three bursts), all of which with small amplitude (typically around 100µV peak-to-peak and 60 seconds duration).

In Figure 7.1, there is an Alvarez train composed by six bursts (red, top plot), all of them detected by the Wavelet time marginal (green, top plot).

As seen on the Scalogram (Figure 7.1, bottom plot) the Alvarez waves distributes its energies from 0.1 Hz to almost 0.6 Hz with the highest energies (dark red) located in the lower frequencies [0.1 - 0.2] Hz and in the higher frequencies >0.4 Hz.

This is also verified in the spectral analysis results (Figure 7.2, left) where both parametric and non-parametric methods as well as the Wavelet frequency marginal detects the more energetic peaks at the beginning, [0.1 - 0.2] Hz, and then there is two energetic frequency peaks located at 0.3 Hz and 0.4 Hz, with the nonparametric methods detecting energy at 0.5 Hz. This is illustrated on the cumsum graphs (Figure 7.2, right) which have a higher slope in the frequency region [0.1 - 0.2] Hz, where there is a higher increase in power, being almost flat until 0.4 Hz, upon which there is a small increase in power. In this case, most of the component power is within [0.1-0.48] Hz.

In Figure 7.3, there is signal (top plot) and Scalogram (bottom plot) of one burst of the Alvarez wave train. As it can be seen, it distributes its energy from 0.1 Hz to almost 0.6 Hz. The darker tones of red on the Scalogram, more energy, are located on the lower energies [0.1 - 0.2] Hz and [0.4 - 0.5] Hz, whereas in between there is a decrease in energy (lighter tone of red).

The Alvarez waves were frequently detected on records very close to the labor date, or even in labor records, which is expected as they can lead to the development of more synchronous contractions, labor contractions. However, before the 37 weeks of gestation (Late Preterm) it can lead to preterm labor and this fact explains its recent interest for pre-term risk evaluation [45].

The Alvarez waves detected on the EHG were, at times, present on the TOCO as uterine irritability, other times they were only detected on the EHG as there was no correspondent uterine irritability at the TOCO.

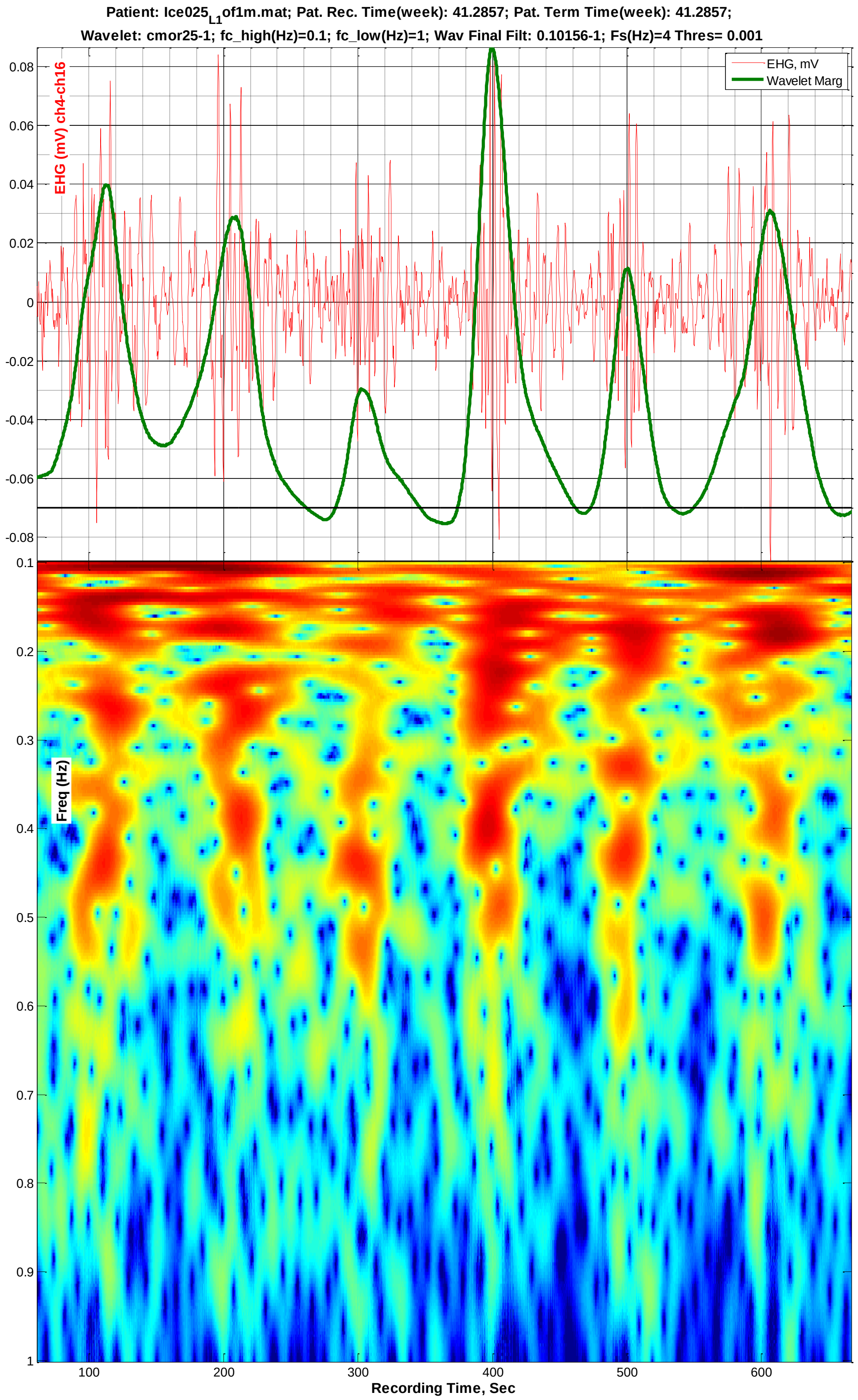

Figure 7.1 – Time-Frequency representation of an Alvarez train wave:Six bursts (red, top plot) all detected by the Wavelet time marginal (green, top plot). At the bottom plot there is the Scalogram in which it can be seen that the component distributes its energy from 0.1 Hz to almost 0.6 Hz.

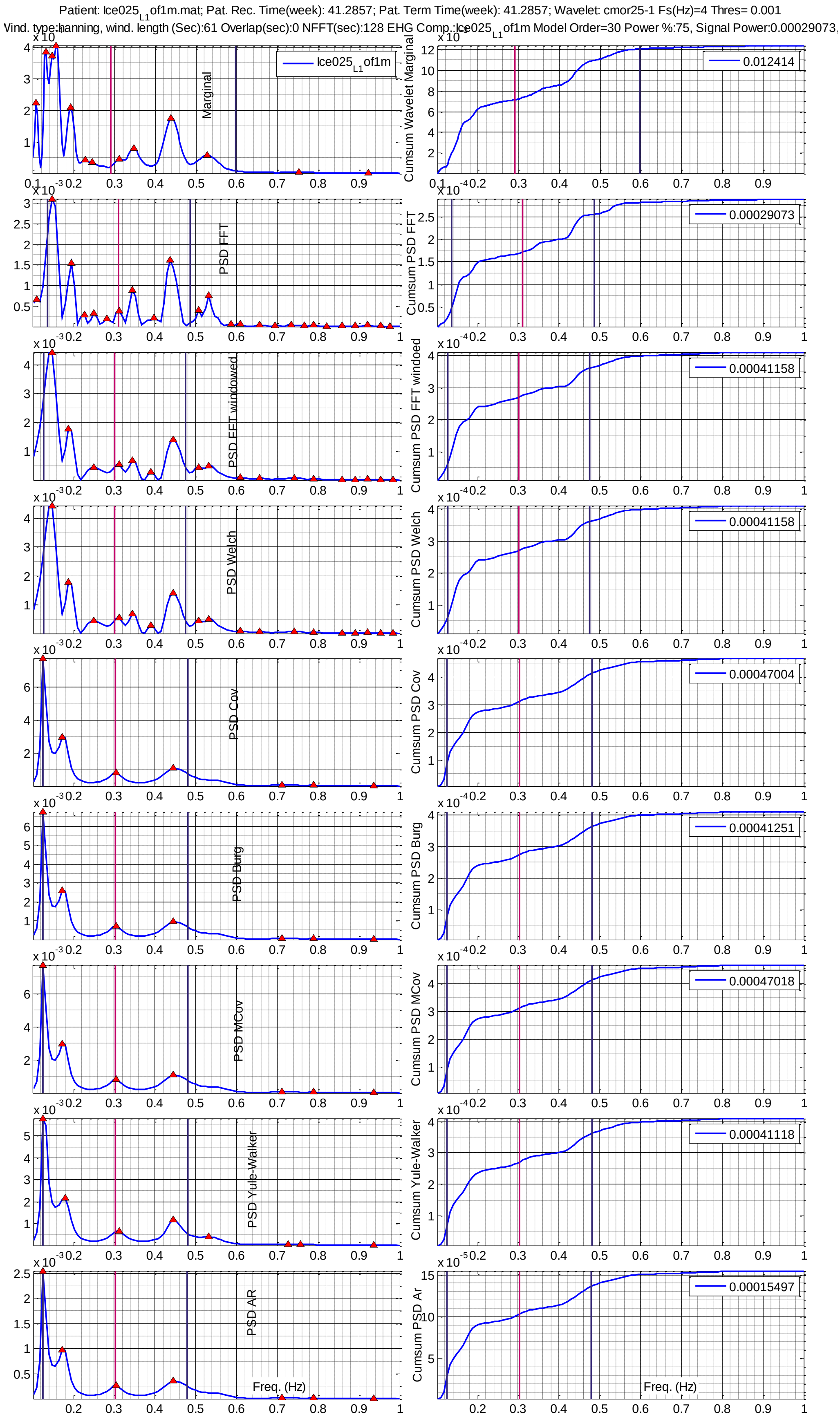

Figure 7.2 - PSD estimations of the Alvarez train wave: PSD estimations with the Wavelet frequency marginal, parametric and nonparametric methods (left) and respective cumsum (right). (More explanations are available in the text)

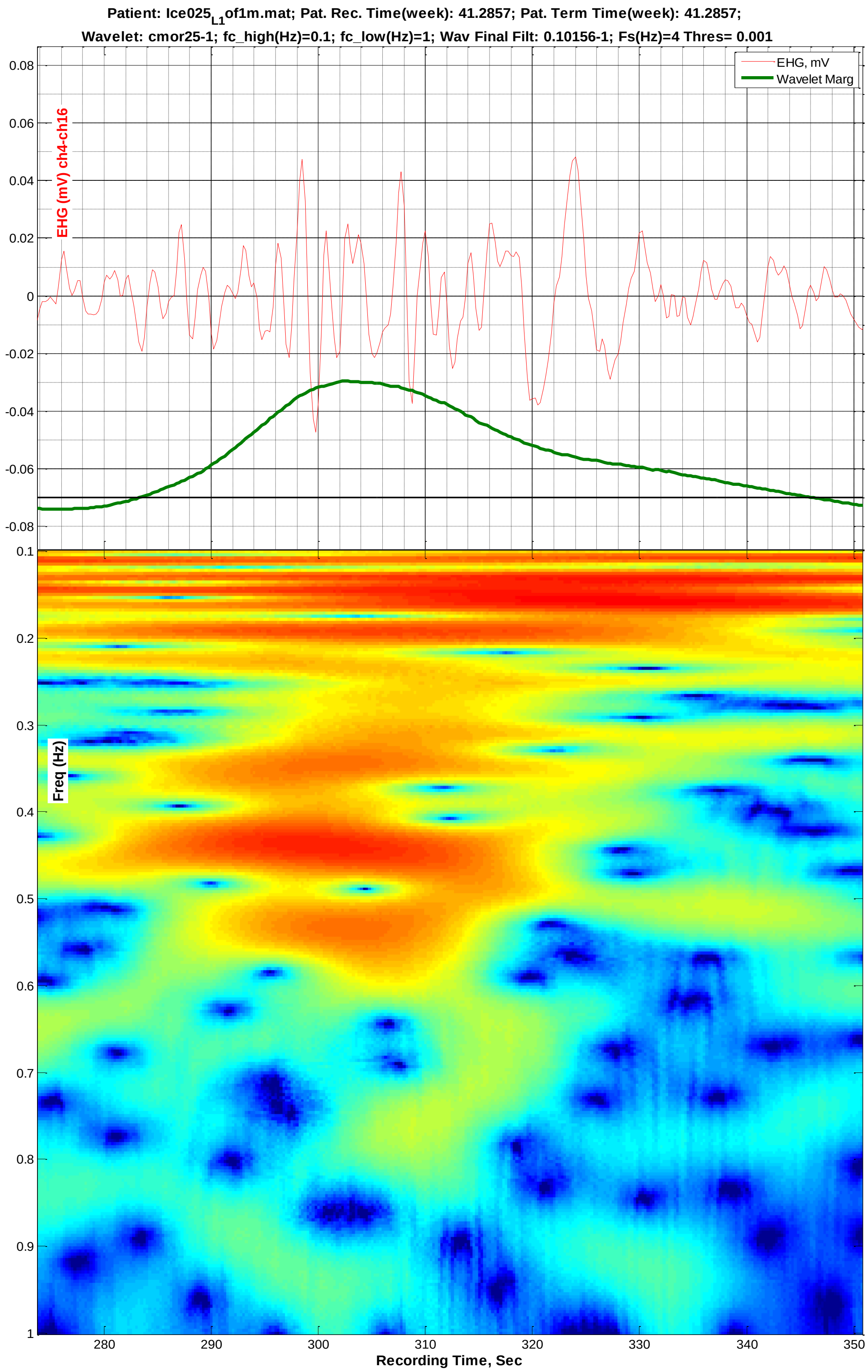

Figure 7.3 – Time-Frequency representation of one burst selected from the Alvarez train wave: Alvarez wave (red, top plot) with the Wavelet time marginal (green, top plot) and correspondent Scalogram (bottom plot). The component distributes its energy from 0.1 Hz to almost 0.6 Hz.

7.2 Contractions

Unlike the Alvarez, which is a train of waves, each one very close to each other, contractions can sometimes appear as just one burst in the record or with a significant distance of the next contraction. Also, contractions have higher duration compared to the Alvarez waves, and generally higher amplitude.

In Figure 7.4 there is the contraction followed by a fetal movement. The Wavelet marginal detects both the contraction and fetal movement. This was recurrently seen throughout the classification process – fetal movements following and preceding contractions, which may be an indicator of an interaction between the fetus and the uterus. Also, most of the contractions seen at the EHG were detected by the TOCO.

As mentioned on chapter 3 and reported by [22] at midterm the frequency of contractions is less than 0.2 Hz and at late term, is greater than 0.5 Hz.

In an attempt to find any differences in the frequency domain according to the gestational week, contractions were categorized as follows:

- **Contractions** – All the contractions before the 36 weeks of gestation.
- **Early labor Contractions (ELC)** – All the contraction after the 36 weeks of gestation, but weeks apart from labor
- **Late Labor Contractions (LLC)** – All the contractions very close to the labor date.

The events labeled as contractions presented the following behavior in the frequency domain, regardless of its gestational age:

- **Wide frequency band**, like the contraction in Figure 7.4, 37 weeks of gestation. Unlike the Alvarez Waves, the energy appears to be almost evenly distributed among the frequency interval [0.2 - 0.5] Hz, which can be seen on the spectral analysis results (Figure 7.5). The cumsum graphs shows an almost linear increase in energy from [0.1 - 0.55] Hz.
- **Narrow frequency band**, like the contraction in Figure 7.6, 38 weeks of gestation. This contraction was found on the records of subject 26, 38 weeks pregnant, delivered a week later. As seen on the Scalogram (Figure 7.6) and confirmed on the spectral analysis results (Figure 7.7), the energy is distributed among the lower frequencies [0.1 - 0.2] Hz. Also, the cumsum graph has a linear shape in that region, with a high slope, as most of the component final power is in that region.

None of the events in the constructed database were characterized as Braxton-Hicks as according to the consulted physicians more information is needed in order to characterize a contraction as Braxton-Hicks. That event appears before the 36 weeks of gestation and does not cause effacement or dilatation of the cervix, information that was not provided in the Iceland database. As such, the contractions found in the EHG signal, before the 36 weeks of gestation, can be Braxton-Hicks if there was no effacement or dilatation of the cervix, which there is no way of knowing.

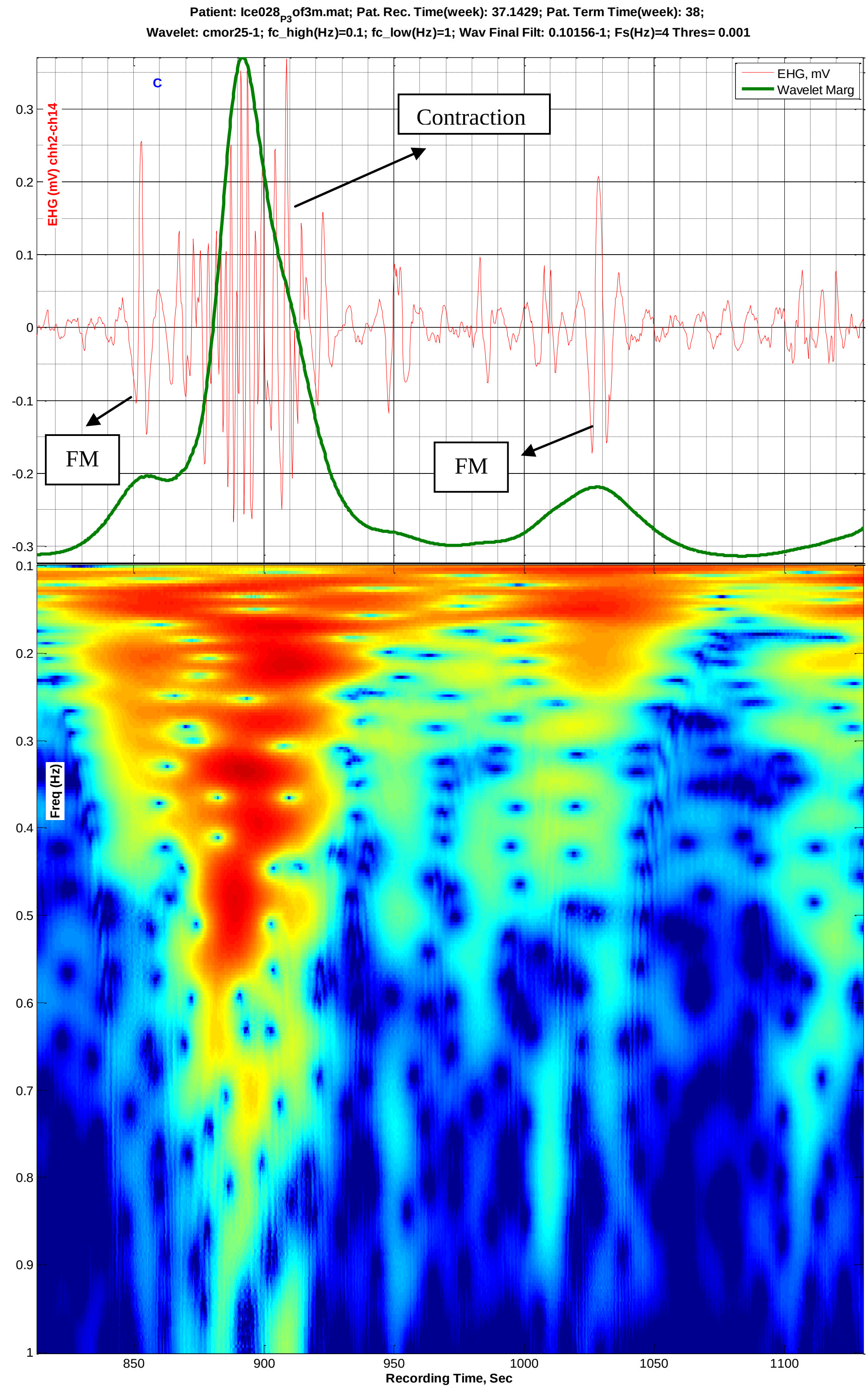

Figure 7.4 – Time-Frequency representation of a contraction (subject 28, 37 weeks of gestation) followed and preceded by fetus movements, all of which detected by the Wavelet time marginal (green, top plot) and correspondent Scalogram (bottom plot). The contraction energy is distributed among the frequency interval [0.1-0.6] Hz. The fetal movement has a narrow frequency bandwith, only in the lower frequencies.

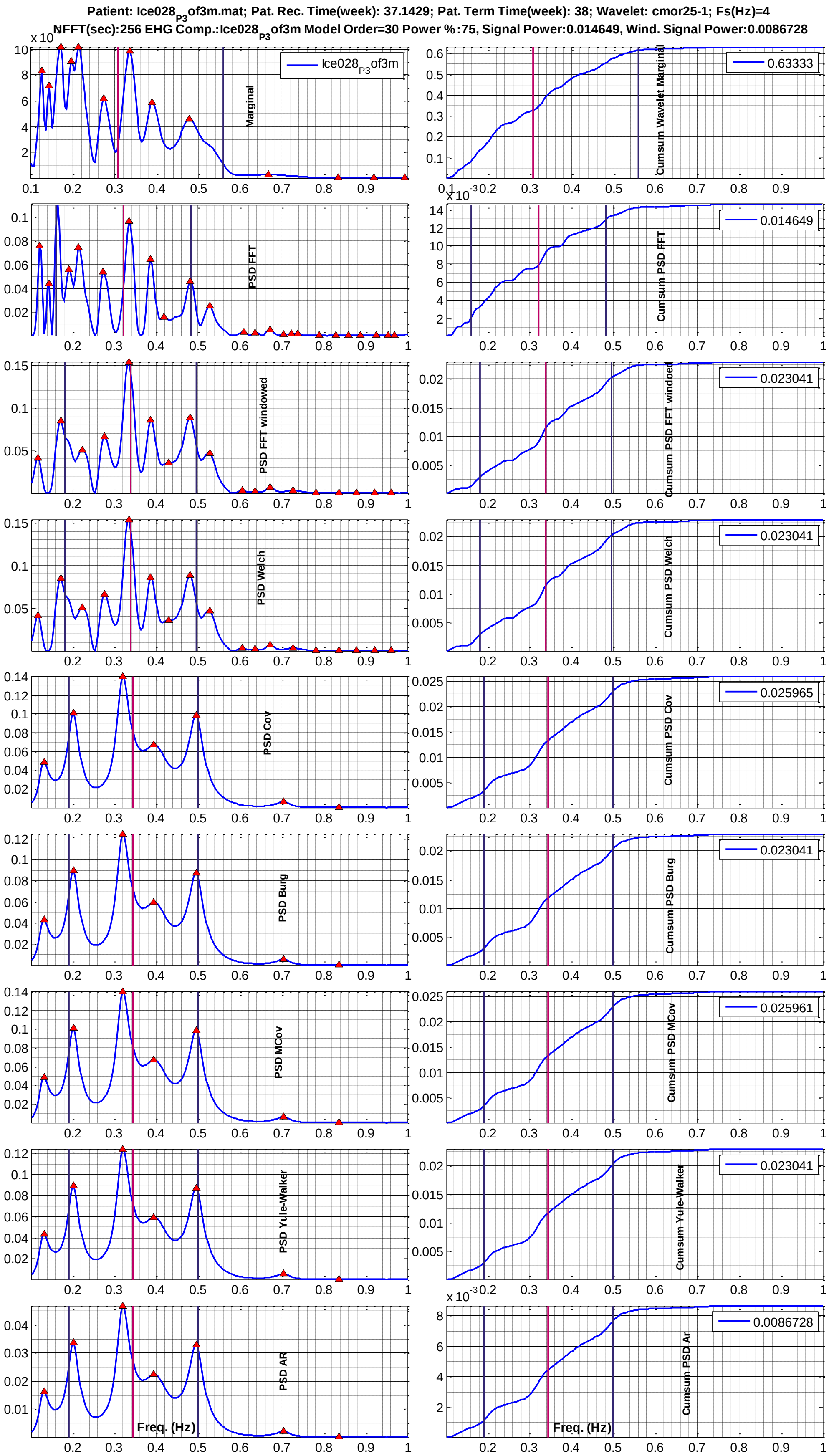

Figure 7.5 - PSD estimations of the Contraction (subject 28, 37 weeks of gestation) with the Wavelet frequency marginal, parametric and nonparametric methods (right) and respective cumsum (left). (More explanations are available in the text)

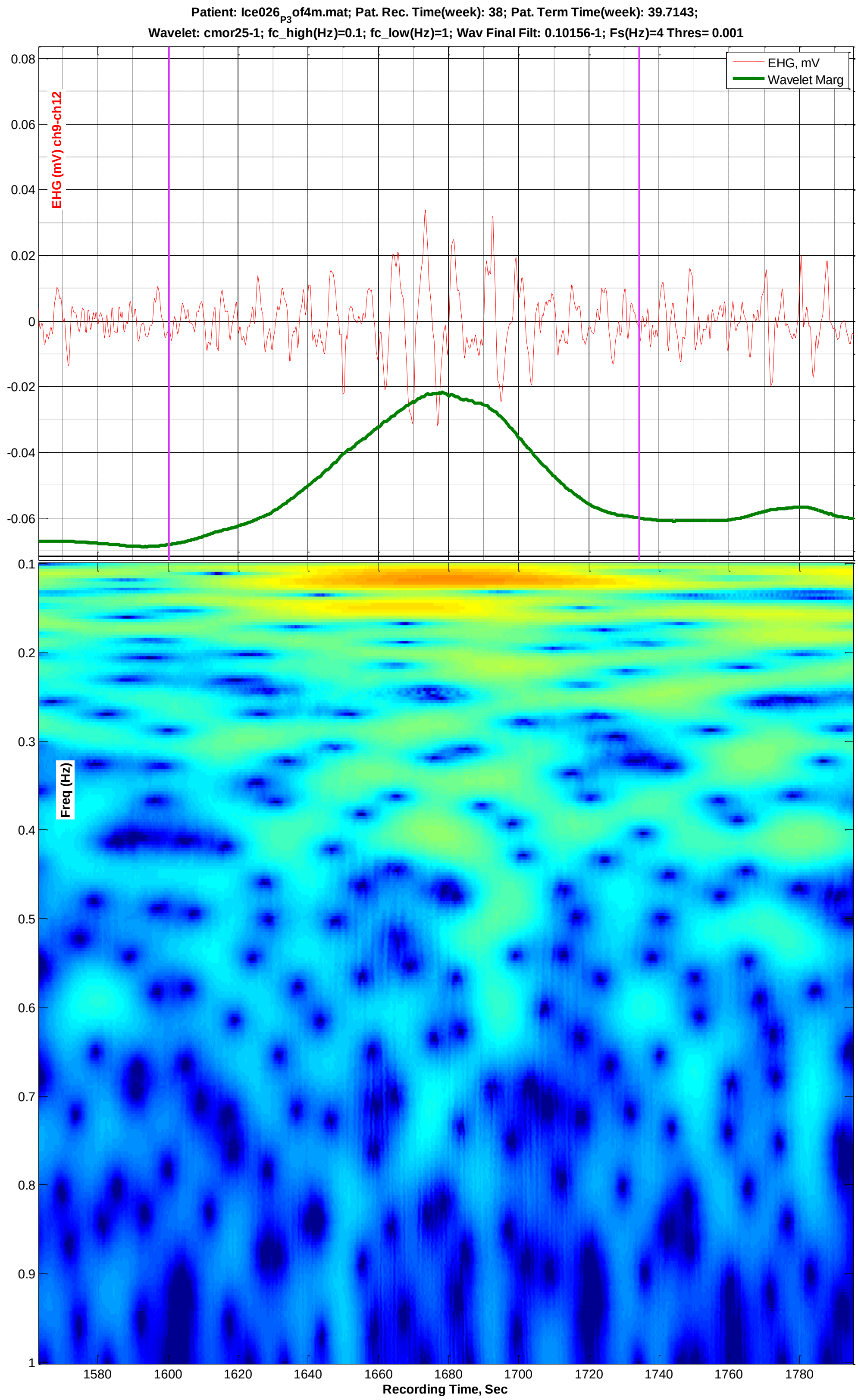

Figure 7.6 – Time-Frequency representation of a contraction (subject 26, 38 weeks of gestation) with Wavelet time marginal (top plot) and correspondent Scalogram (bottom). The energy is distributed among the lower frequencies [0.1-0.15] Hz

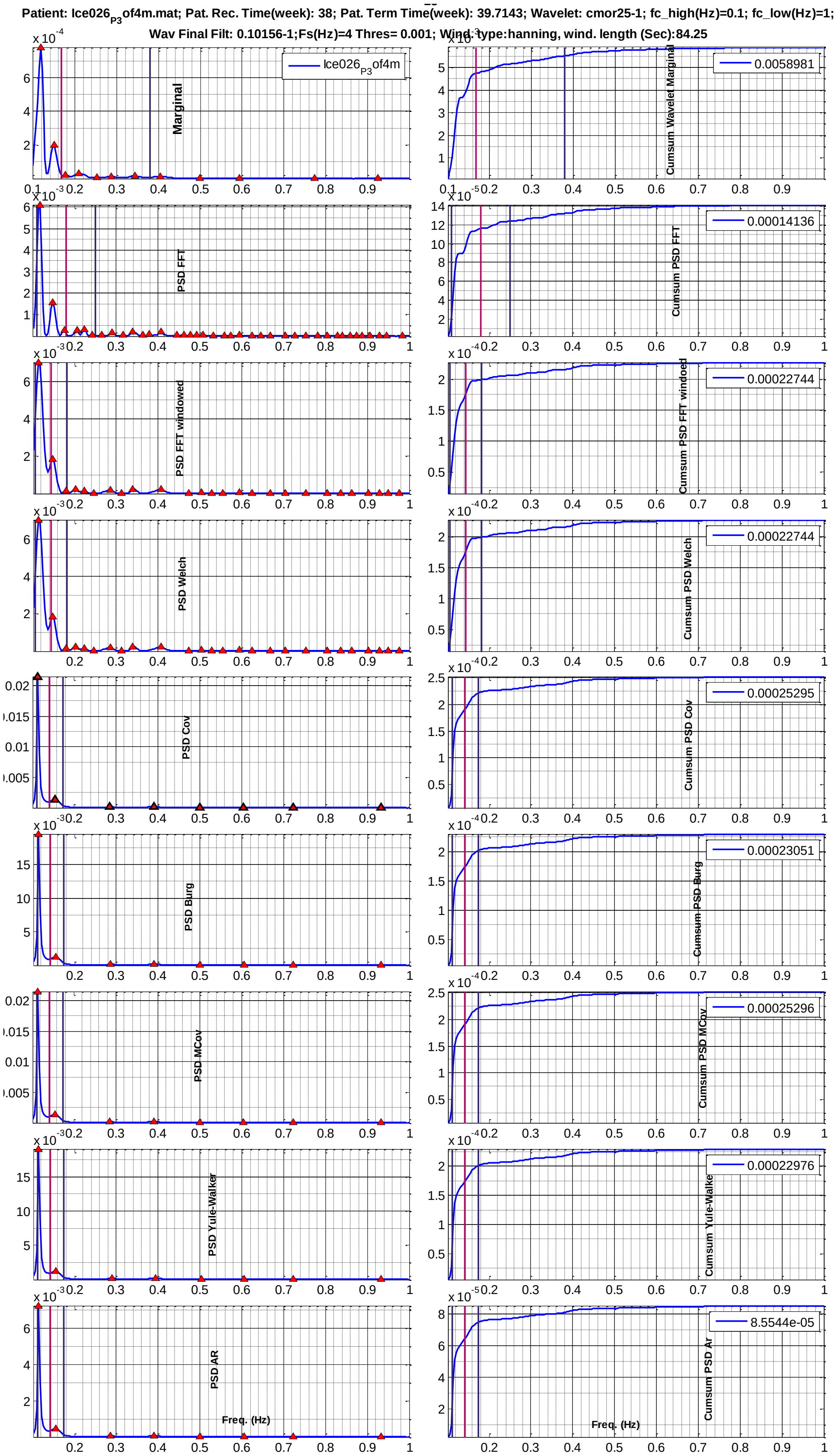

Figure 7.7 - PSD estimations of the Contraction (subject 26, 37 weeks of gestation) with the Wavelet frequency marginal, parametric and nonparametric methods (right) and respective cumsum (left) (More explanations are available in the text)

7.3 Fetal Movements

Fetal movements were also found throughout the analyzed records. They have a consistent shape like the one depicted on figure 7.8 (delimited by the pink bars). Thus, having a very small duration, but varying amplitude.

Fetal movements are low frequency components, with a sinusoidal like spectrum (Figure 7.9). Those events present a narrow frequency band, in this case the fetal movement has most of its energy within [0.1 – 0.25] Hz.

They are an indication of the fetus wellbeing. However, they can be found in between contractions or even Alvarez train waves, thus contaminating the spectrum of those components.

As mentioned before, they often seem to follow or preceded contractions, which may indicate that the fetus may cause the uterus to contract and vice versa, i.e., uterine contractions may cause fetal movements.

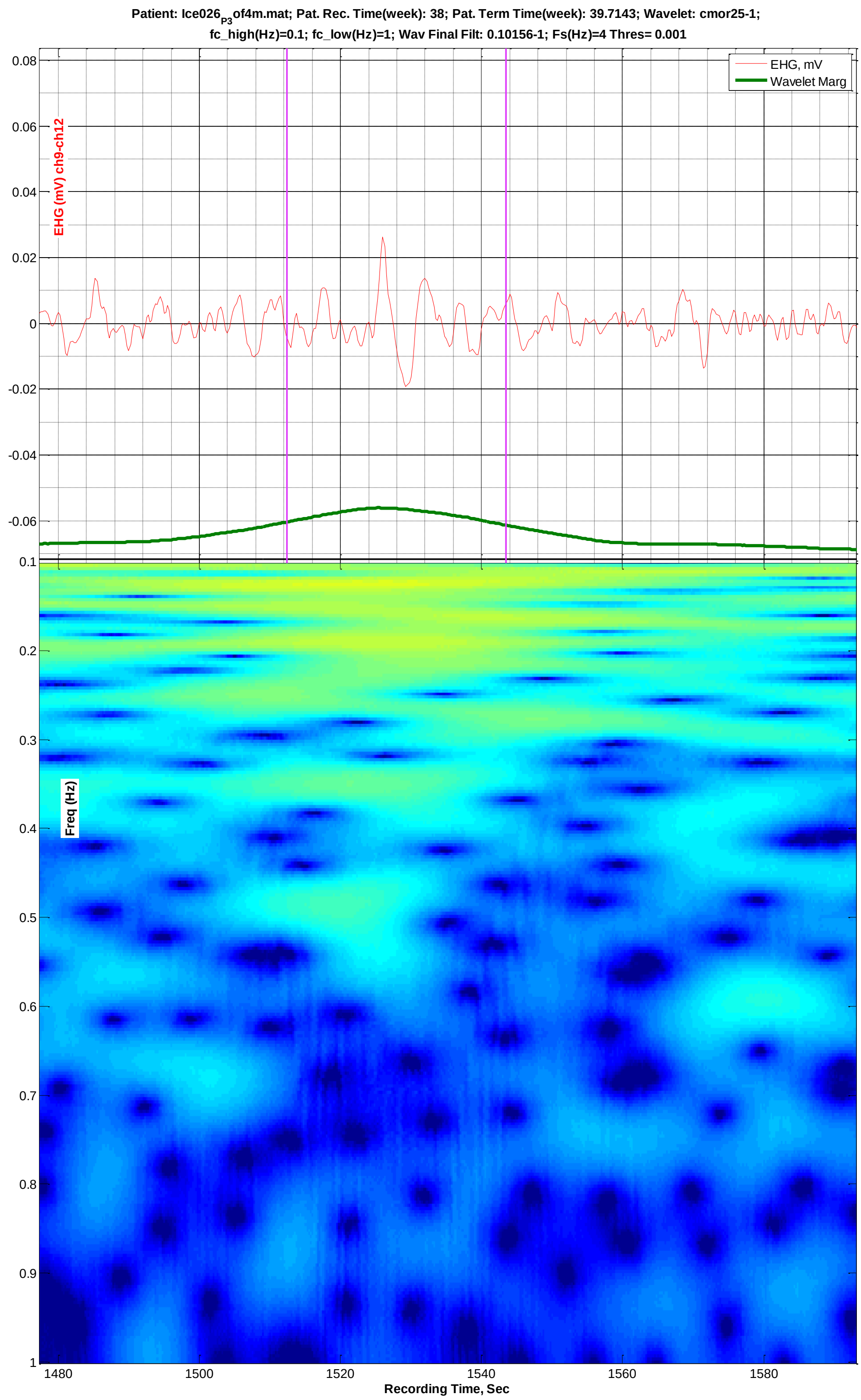

Figure 7.8 – Time-Frequency representation of fetal Movement (subject 26) with Wavelet time marginal (top plot) and correspondent Scalogram (bottom plot). It is a low frequency component.

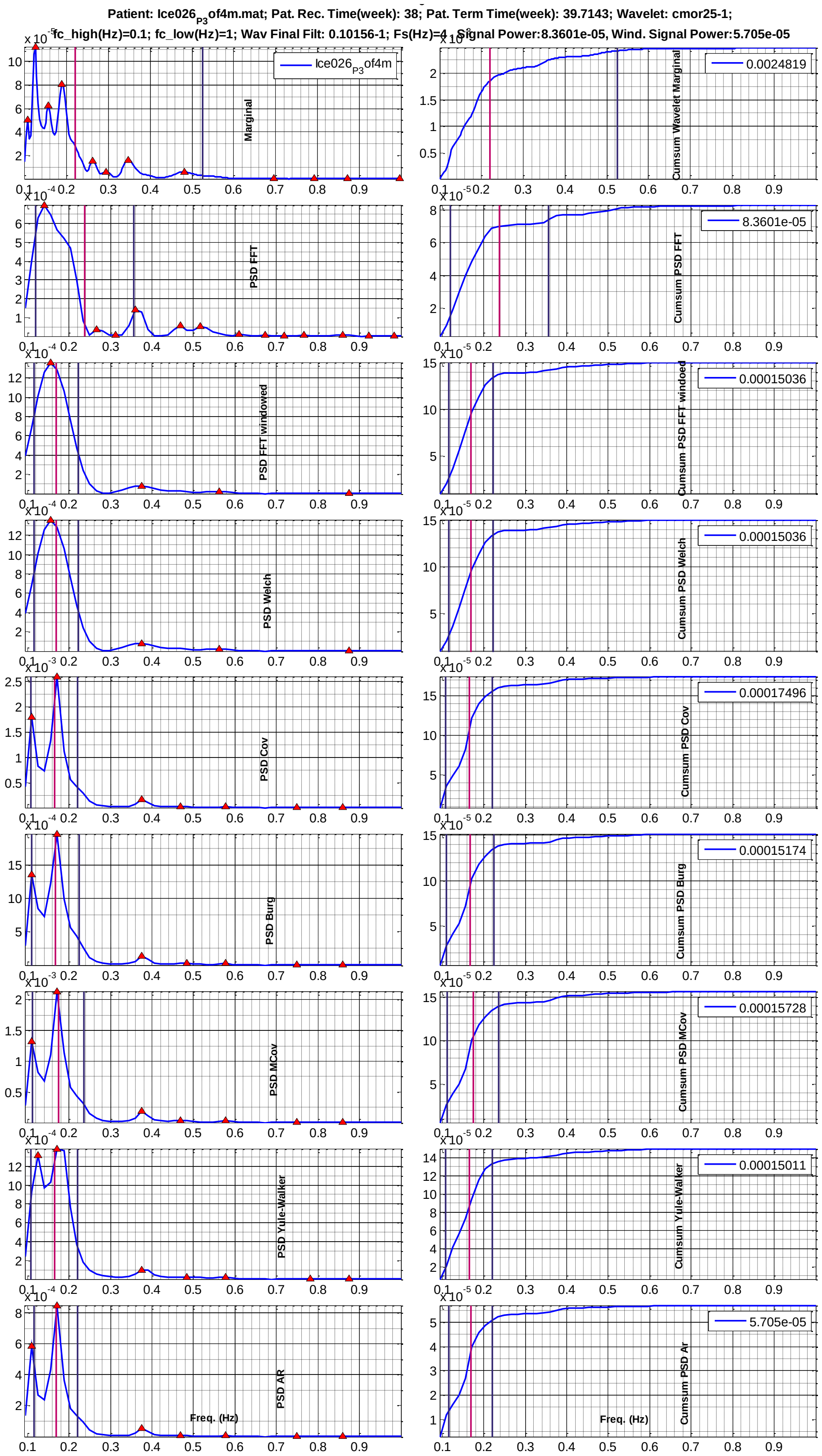

Figure 7.9 - PSD estimations of the fetal movement (subject 26) with the Wavelet frequency marginal, parametric and nonparametric methods (right) and respective cumsum (left) (More information provided in the text)

7.4 LDBF Waves

It was difficult for the doctors to identify this event on the TOCO, as they needed the fetal cardiogram, not available in the Iceland Database, to detect fetal bradycardia, which is caused by hypertonia. Also, a physician can easily detect uterine hypertonia through palpation, without consulting the TOCO. Nevertheless, this event is normally detected in the TOCO as an abnormally long contraction as the uterus does not relax for a long period of time, more than two minutes.

As such, in the available TOCO'S there were a few events that lasted longer than two minutes. Those events were classified as possible LDBF.

One of those events was found on subject 32, fifth recording, at 40 weeks of gestation. A contraction with a duration of roughly 3 minutes (200 seconds), as depicted on Figure 7.10. Therefore, this event was selected and classified as LDBF.

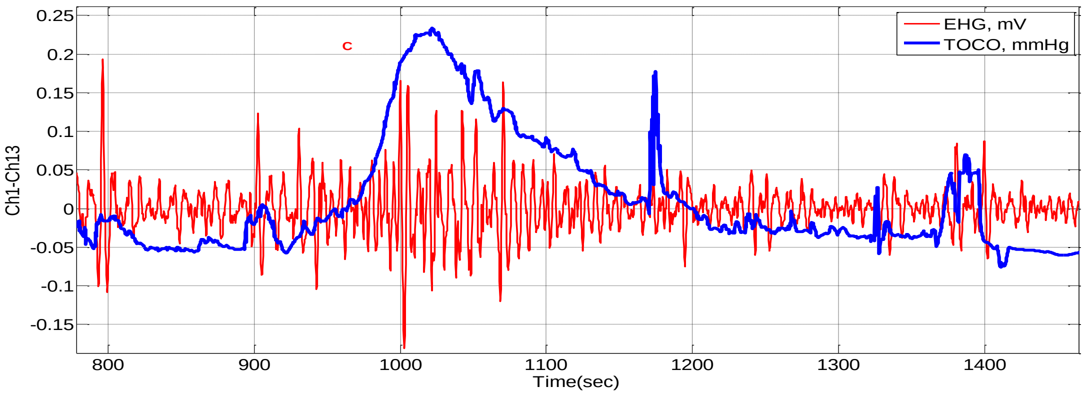

Figure 7.10 – EHG signal of the LDBF (red) with correspondent TOCO (blue)

In fact, this burst last longer than a contraction and has most of its energy distributed in the lower frequencies, [0.1 - 0.3] Hz, which can be seen on the Scalogram (Figure 7.11) and confirmed in the spectral analysis, Figure 7.12. The cumsum graphs show a higher slope on that region.

Also, Figure 7.13 shows the power of each leave in the final level of the WPD tree (top), power percentage of each leave in the final level WPD tree (bottom left) and RMS in each leave of the final level WPD tree. (bottom right) As it can be seen most of the component's energy is in the lower frequencies.

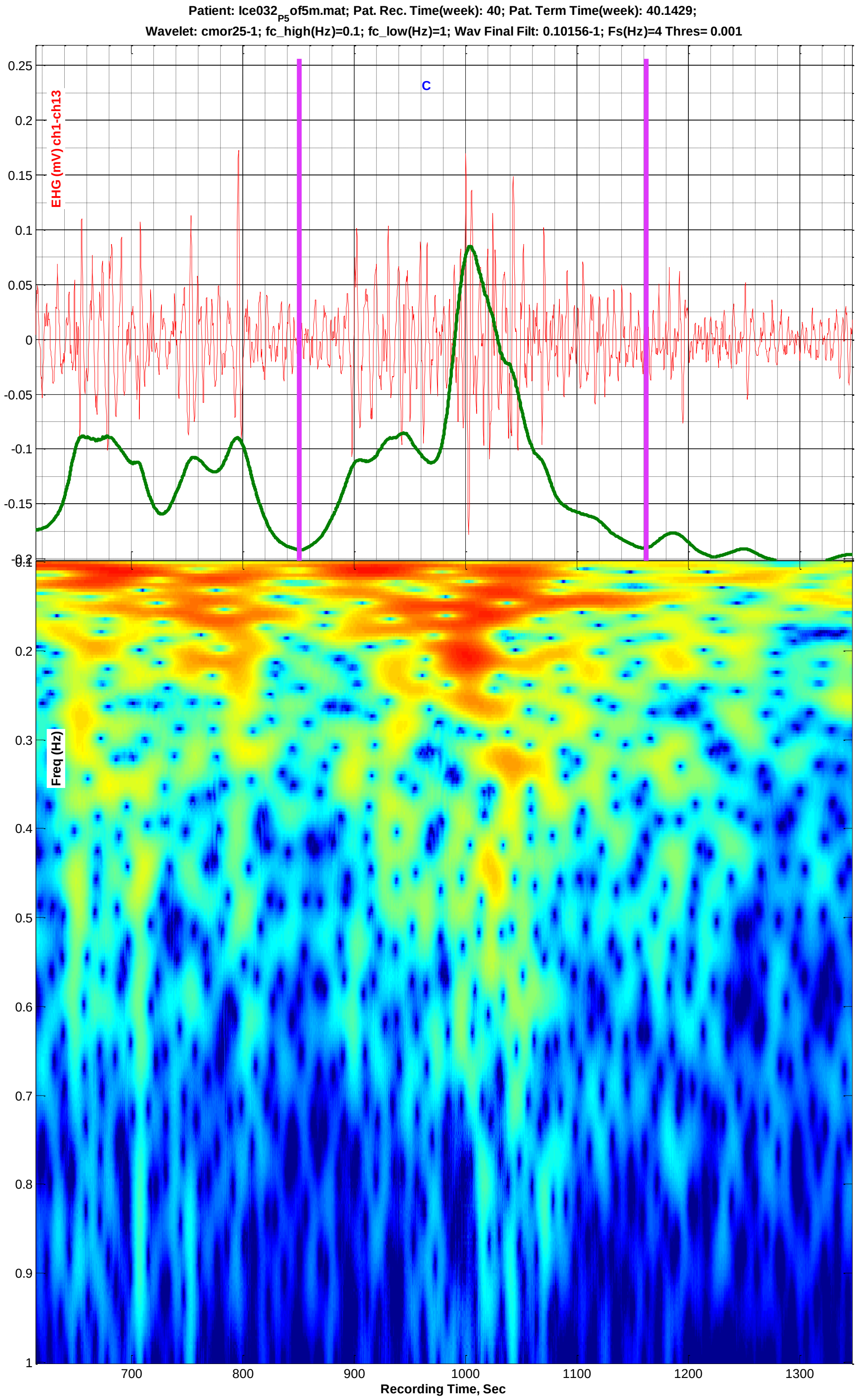

Figure 7.11 – Time-Frequency representation of a LDBF wave (subject 32), delimited with two pink bars (top plot) and identified by the Wavelet time marginal (green,top). The Scalogram (bottom plot) shows an energy distribution in the lower frequencies.

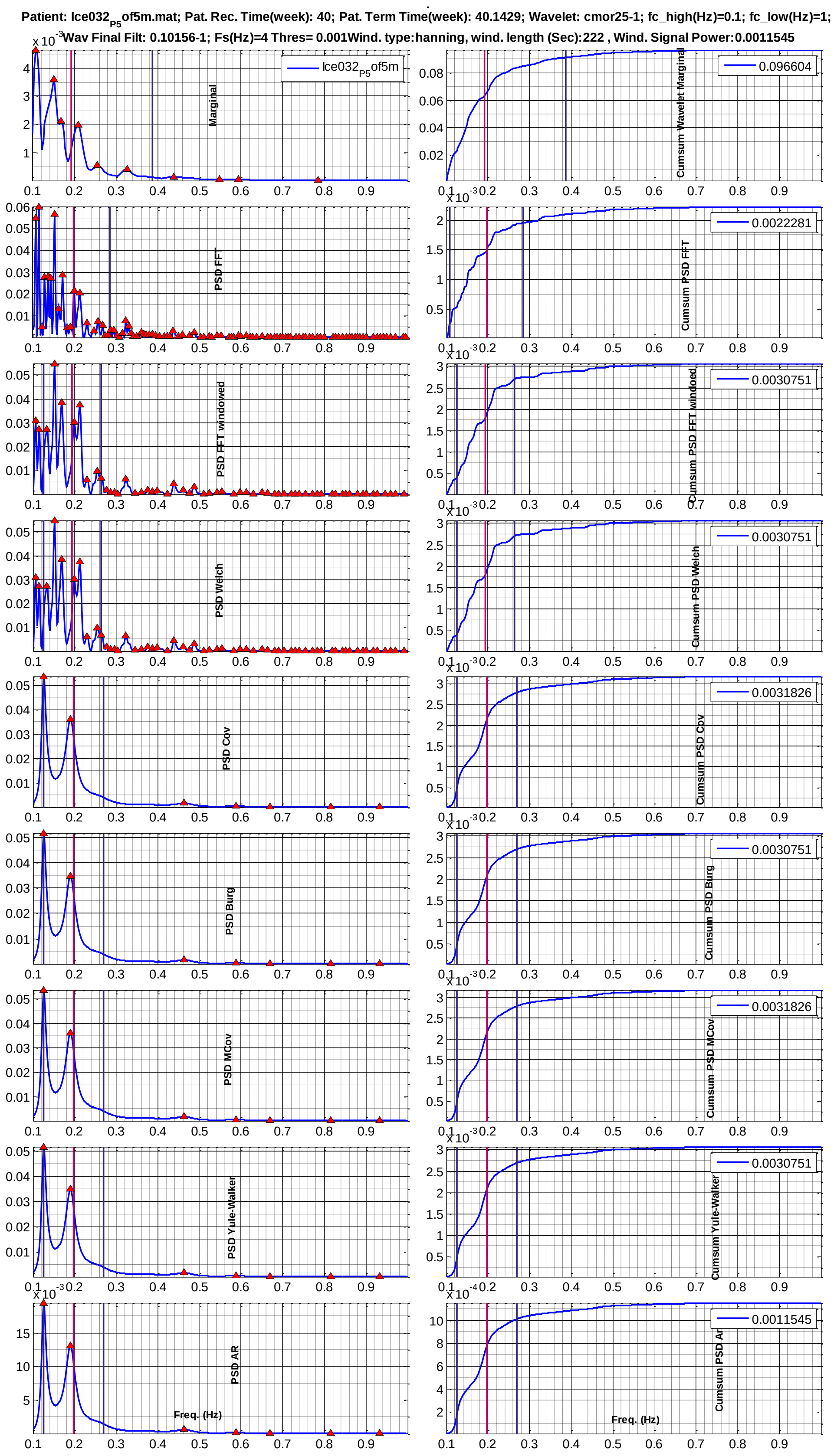

Figure 7.12 - PSD estimations of the LDBF wave (subject 32) with the Wavelet frequency marginal, parametric and nonparametric methods (right) and respective cumsum (left) (More information available in the text)

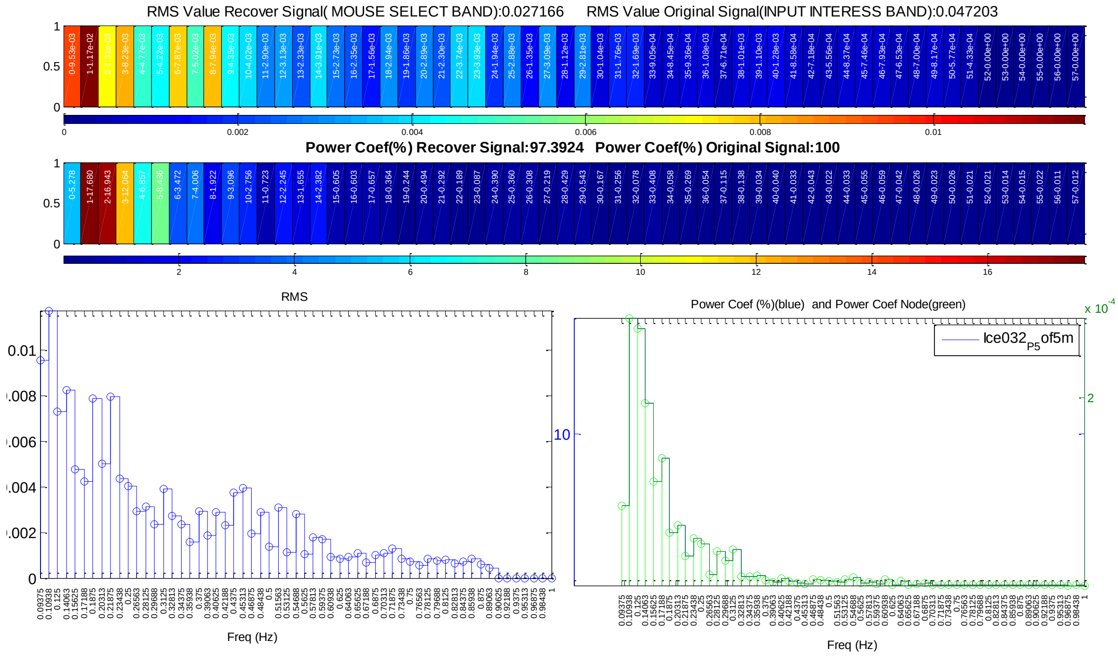

Figure 7.13 – WPD of LDBF wave: Power of each leave in the final level of the WPD tree (top), power percentage of each leave in the final level WPD tree (bottom left) and rms in each leave in the final level WPD tree. (bottom right)

7.5 Fetal Hiccups

Fetal Hiccups are considered normal and can occur after the 9 week of gestation. They can be felt as abrupt, repetitive fetal movements or as irregular, jerky fetal movements. The rate of occurrence is low, as 1 in 50 fetus has hiccups [113].

Fetal Hiccups were found in the Iceland database on the records of subject 34, at 35 weeks of gestation. The event found on that record was labeled as hiccups, since in the provided subject information there was a comment referring that fetal hiccups started at 46 minutes, around the time in which this event is found on the EHG.

As such, this event has a very particular shape, as the frequency decreases in time, which is depicted on the Scalogram, Figure 7.14: the darker red spot starts with a frequency of 0.2 Hz decreasing through time until the minimum frequency, 0.1 Hz. There is a lighter red spot, above with the same behavior, which corresponds to the second harmonic. This characteristic of the signal, frequency variation through time, can only be seen on the Scalogram, whereas the spectral analysis (Figure 7.5) yields the distribution of energy throughout the frequencies, where it can be seen that most of the energy is in the lower frequency region [0.1 - 0.3] Hz.

The question arises about the real origin of this electrical signal: the uterine myometrium that responds to the somewhat saccadic hiccups fetus movements or the associated EMG fetus signal. However, and according to the consulted physicians the first hypothesis seems to be more accurate.

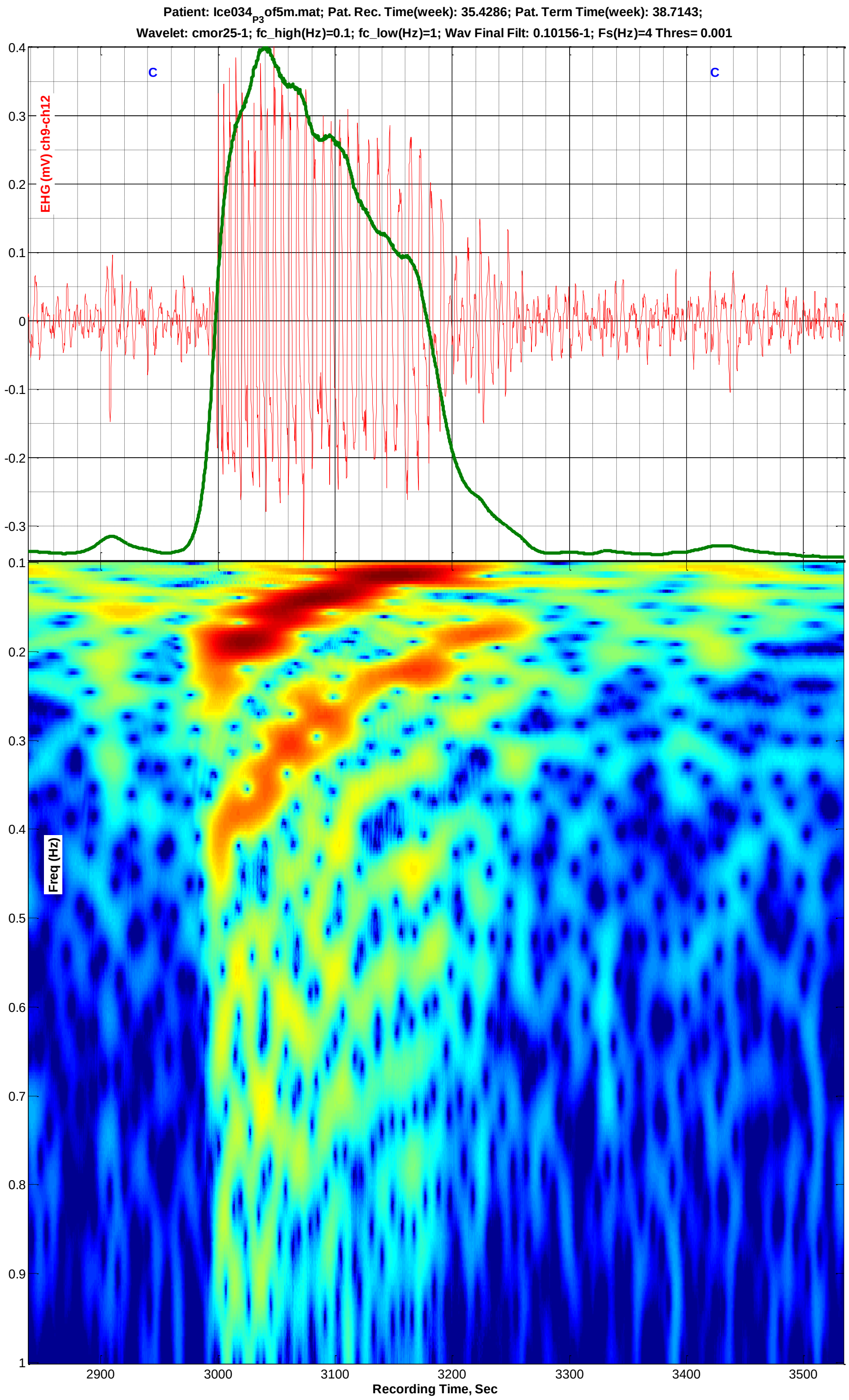

Figure 7.14 – Time-Frequency representation of Fetal Hiccups (subject 34) with Wavelet time marginal (green, top plot) and correspondent Scalogram (bottom), which shows a frequency decrease in time in both the first harmonic (darker red) and second (lighter red).

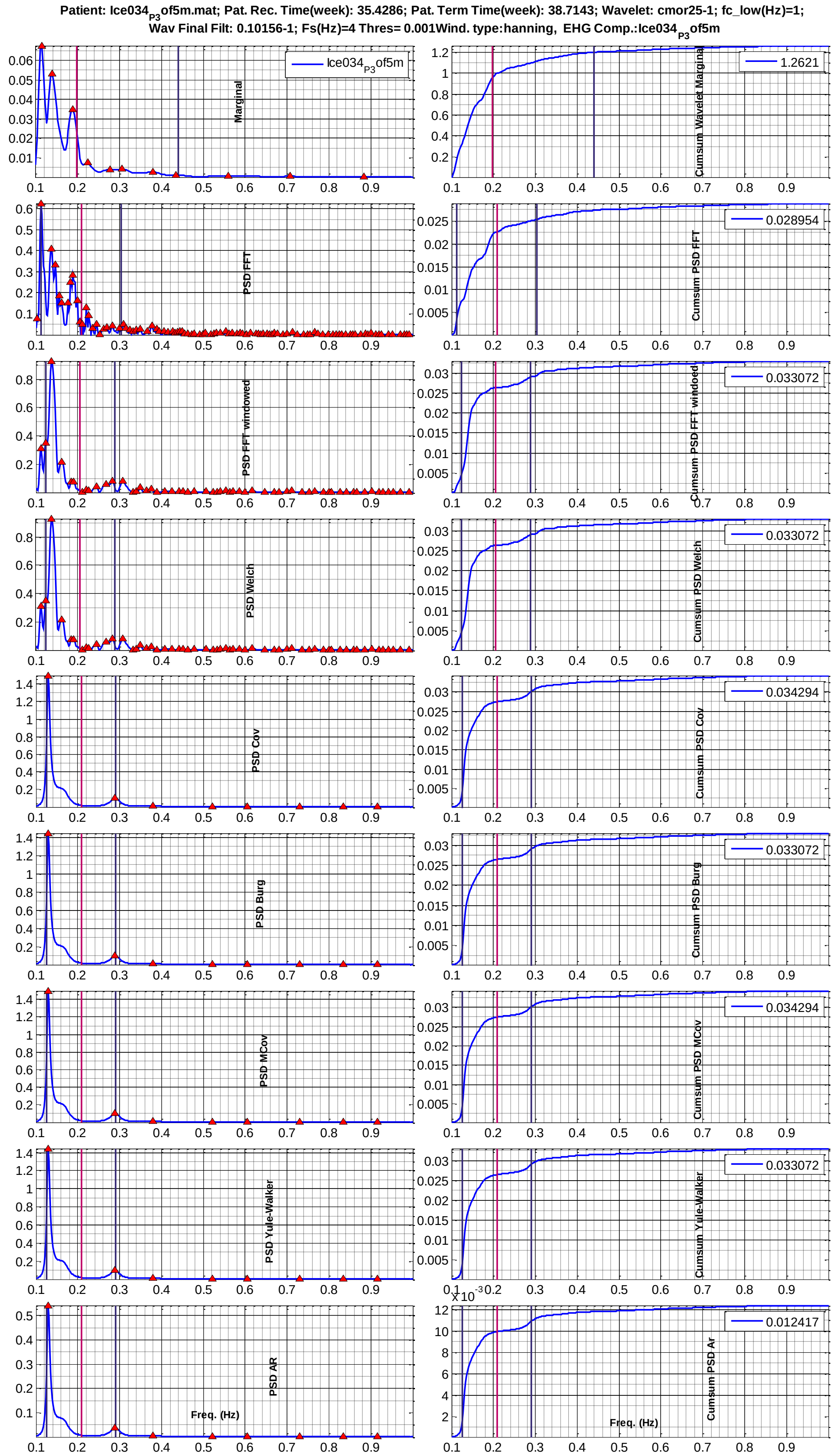

Figure 7.15 - PSD estimations of the fetal hiccups (subject 34) with the Wavelet frequency marginal, parametric and nonparametric methods (right) and respective cumsum (left) (More information in the text)

7.6 Averaging Spectra for each Component

The considerations above listed were about visual inspection of spectral analysis and time-frequency methods.

In this section, an average of the spectral analysis of each component found on the Iceland database records, with the exception of the fetal hiccups (only one event), was computed with the following PSD methods: Wavelet marginal, Welch, Covariance and Least Squares.

- **Alvarez Waves**

In Figure 7.16 there is the PSD average of 10 Alvarez waves. The multicomponent nature of the signal is patent with relevant energy peaks in the lower frequencies (around 0.15 Hz and 0.2 Hz) and in the higher frequencies, 0.4 Hz.

Also, the Standard deviation (red dotted line) for the PSD average is very low, which is an indication that all events labeled as Alvarez waves present a very similar spectrum.

- **Contractions**

Figure 7.17 represents 28 contractions PSD averaged (blue) along with 71 ELC (green) and 17 LLC (red). For comparing purposes the spectrum of those three classes were plotted on the same graph, since they belong to the same event family.

A relevant frequency peak in the lower frequencies is present at 0.1 Hz. In this work, the interpretation given to the peaks at 0.1 Hz is the following: it may result from the low pass filtering of 0.1 Hz over the signal whose spectrum is decaying from 0 Hz. It may be also a true signal frequency peak. To distinguish these two cases the time-frequency representation should be inspected for each case. As for the remaining frequency peaks, they appear to shift to the higher frequencies as the pregnancy progresses.

However, ELC seems to be more energetic than LLC, but this may be due to the insufficient number of LLC events in the database.

Additionally, as shown in Figure 7.18 the following parameters were extracted from the events labeled as contractions, ELC and LLC: Upper and lower frequency limits, containing up to 75% of the event's power density spectrum (FFT, Welch and Burg methods) and bandwidth. In the case of the marginal the frequency bounds were automatically obtained through the PSD standard deviation and central frequency.

After parameter extraction an average for each class was computed. The results are illustrated in Figure 7.18, and are consistent regardless of the PSD method. There is a slight increase in the upper frequency limit, which is more noticeable from the contraction to the early labor contractions. There is also an increase in the lower frequency limit and the bandwidth remains constant. These results are consistent with reports that establish a frequency increase with gestational age [114][115][116]. Nevertheless, the represented frequency increase is very discrete which may be a result of the limited number of events in the database.

Also, the Standard deviation (dotted line) for each average PSD is very low, meaning that all the spectra used in the average have a similar behavior.

- **Fetal Movements**

The averaged PSD for 89 events labeled as fetal movements is depicted in Figure 7.19: Both marginal and Welch estimates detect a broad peak in the lower frequencies (0.12 Hz). Two more frequency peaks are detected by the parametric estimates (0.15 Hz and 0.24 Hz), which better represents low duration signals as these. It is a low frequency component.
Standard deviation (red dotted line) of the average PSD is very low, which is an indication of the consistency of the average spectrum.

- **LDBF Waves**

There were only four events classified as LDBF waves in the event database. So, the averaged PSD of those four events results in a wide band spectrum as depicted in Figure 7.20, which is not consistent with the common LDBF definition: a low frequency signal, this should be related with the low sample number (only four events). Despite this fact, a 0.15 Hz component is dominant, which may be an indication that this is actually a composite signal.

This LDBF waves is a rare event and this makes its presence in any database an infrequent component. However, LDBF's are a marker of a serious obstetric condition.
The standard deviation (red dotted line) is high, which may be an indication that some events were incorrectly classified as LDBF waves.

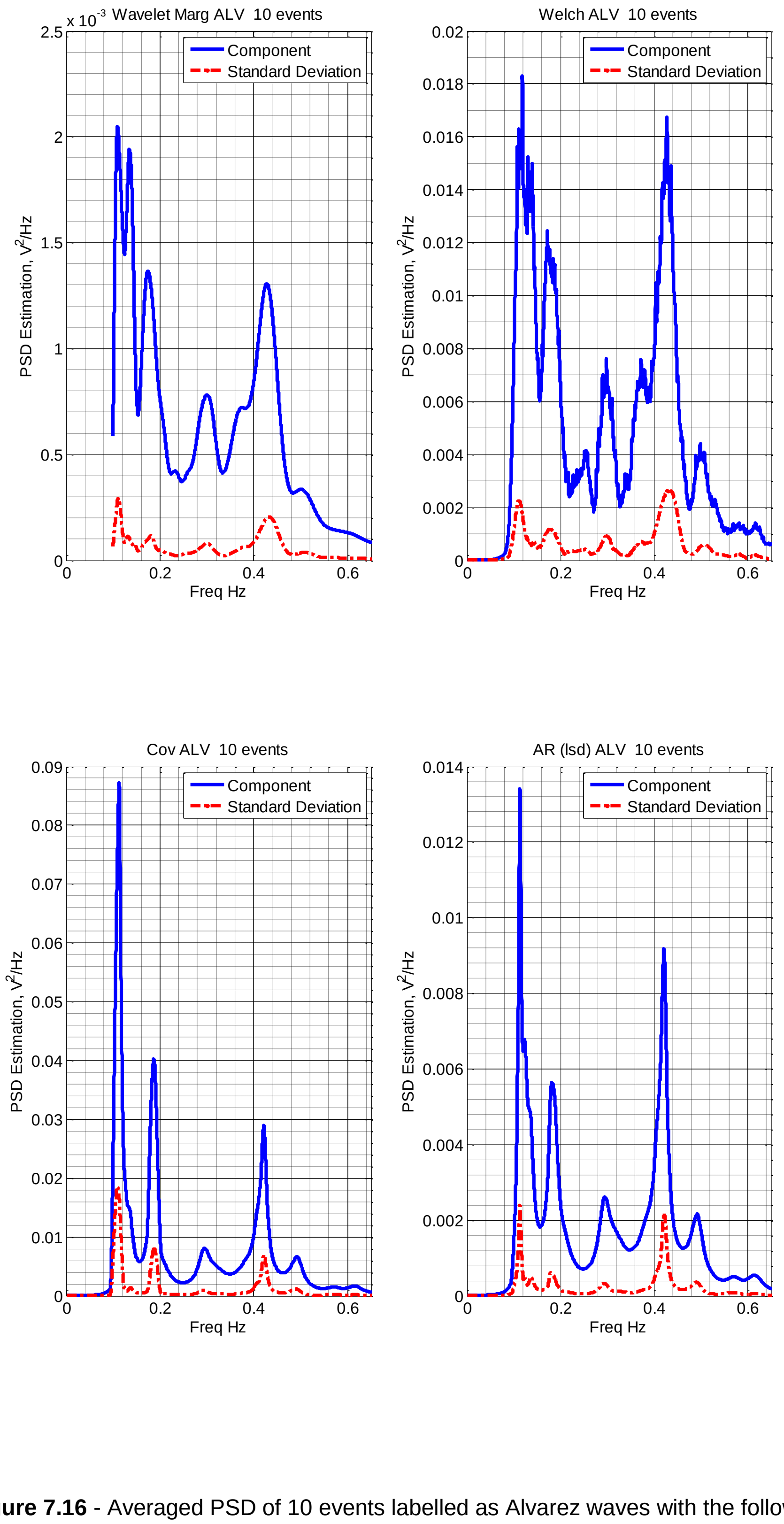

Figure 7.16 - Averaged PSD of 10 events labelled as Alvarez waves with the following methods: Wavelet marginal (top, left), Welch (top. rigth), Covariance (bottom, left) and Least Squares (bottom, right). Standart deviation for each PSD average (red dotted line)

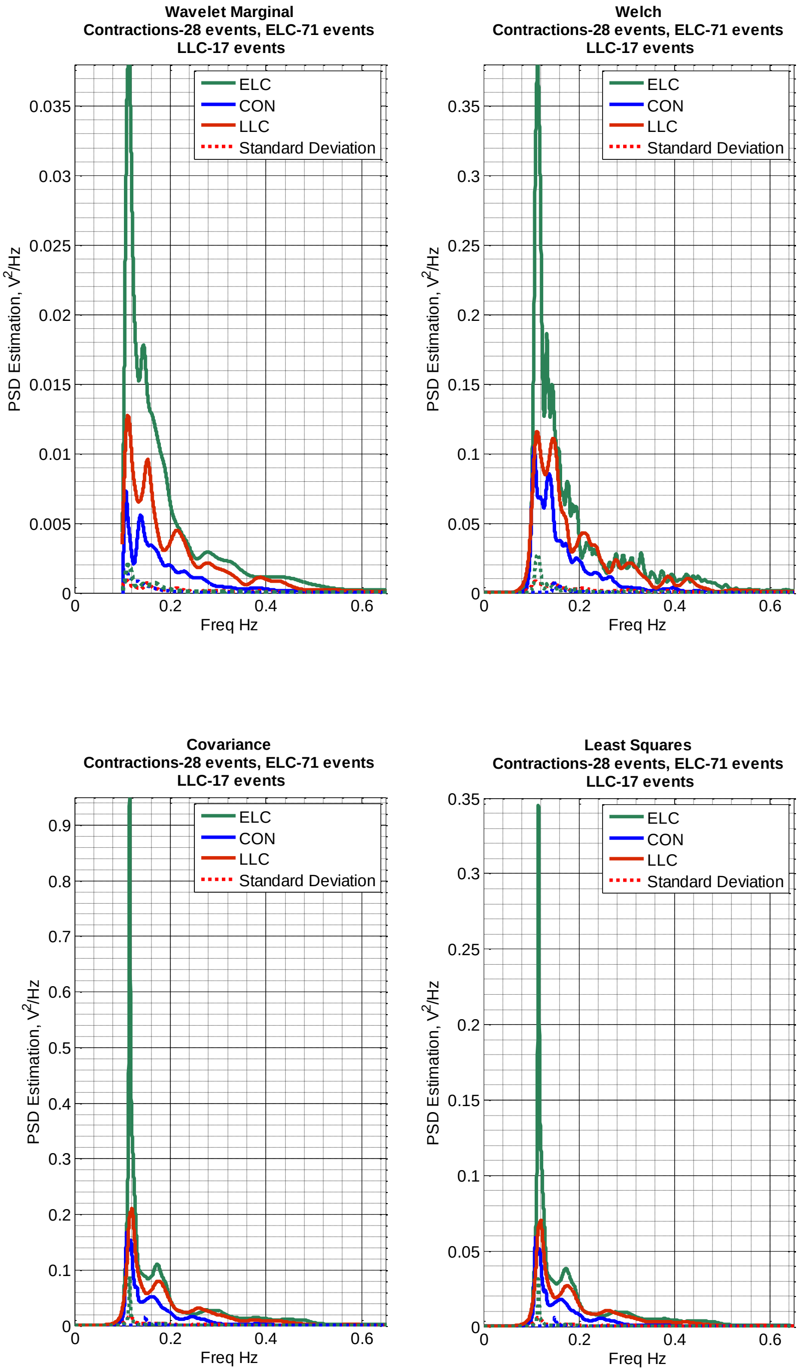

Figure 7.17 - Averaged PSD of Contractions (blue), ELC (green) and LLC (red) events with the following methods: Wavelet marginal (top, left), Welch (top. rigth), Covariance (bottom, left) and Least Squares (bottom, right). Standart deviation for each PSD average (red dotted line)

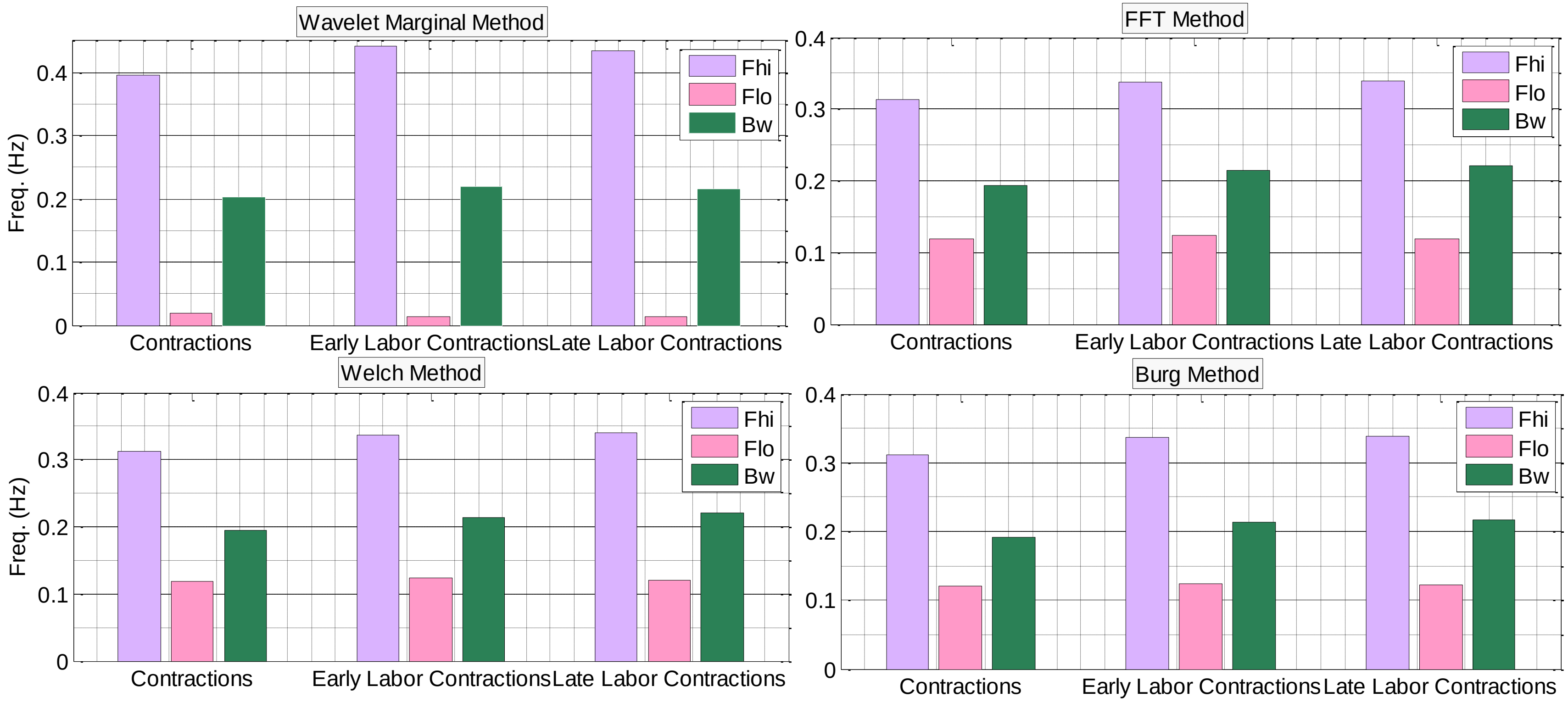

Figure 7.18 - Study of the contractions power distribution throughout pregnancy: Average of the following parameters extracted from three classes of uterine events (contractions, early labor contractions and late labor contractions): Upper and lower frequency limits (Fhi and Flo respectivelly), containing up to 75% of the PSD (marginal, FFT, Welch and Burg methods) and bandwidth (Bw). There is a slight increase in both upper and lower frequency limits, specially from the contractions to the early labor contractions.

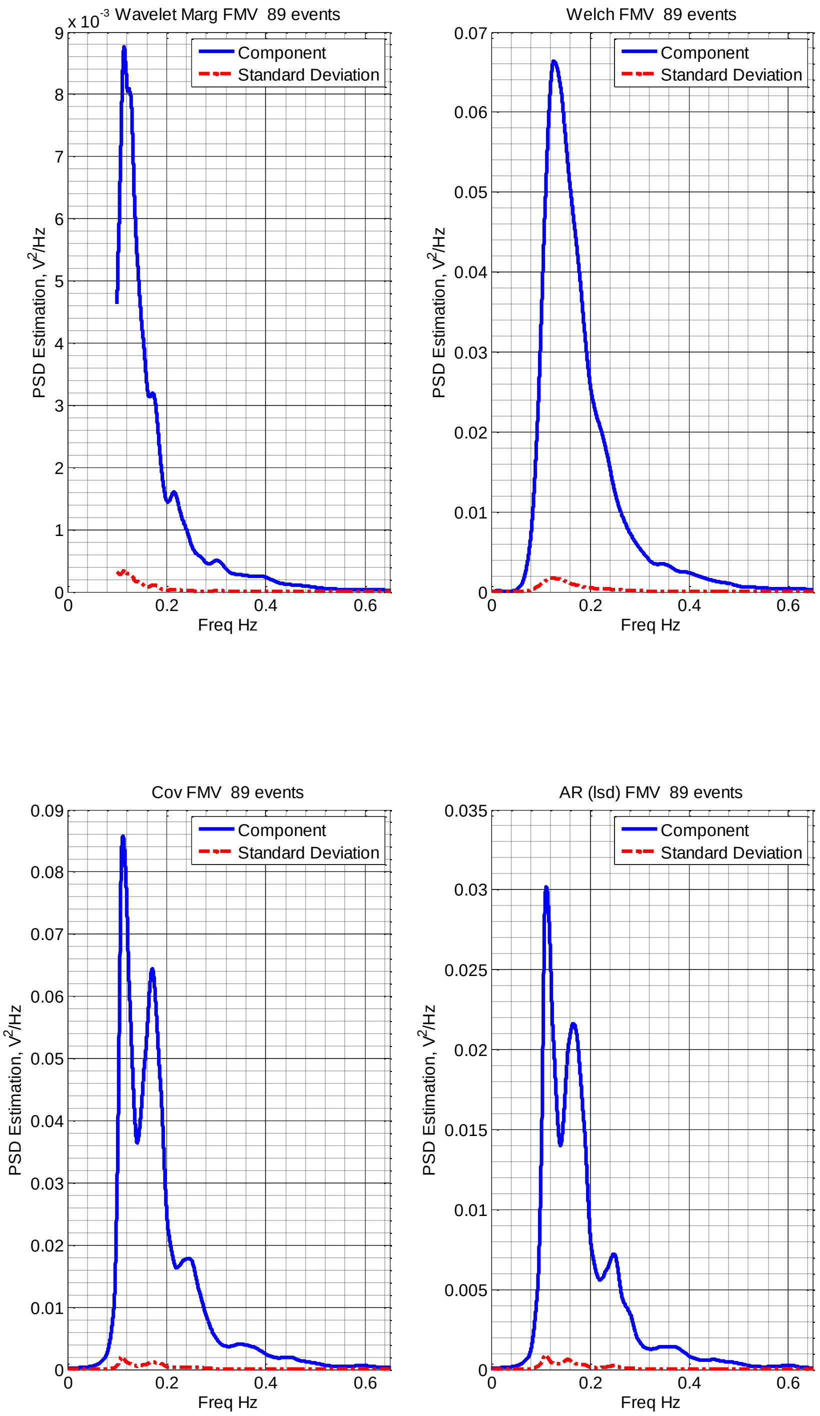

Figure 7.19 - Averaged PSD of 89 events labelled as fetal movements with the following methods: Wavelet marginal (top, left), Welch (top. rigth), Covariance (bottom, left) and Least Squares (bottom, right). Standart deviation for each PSD average (red dotted line)

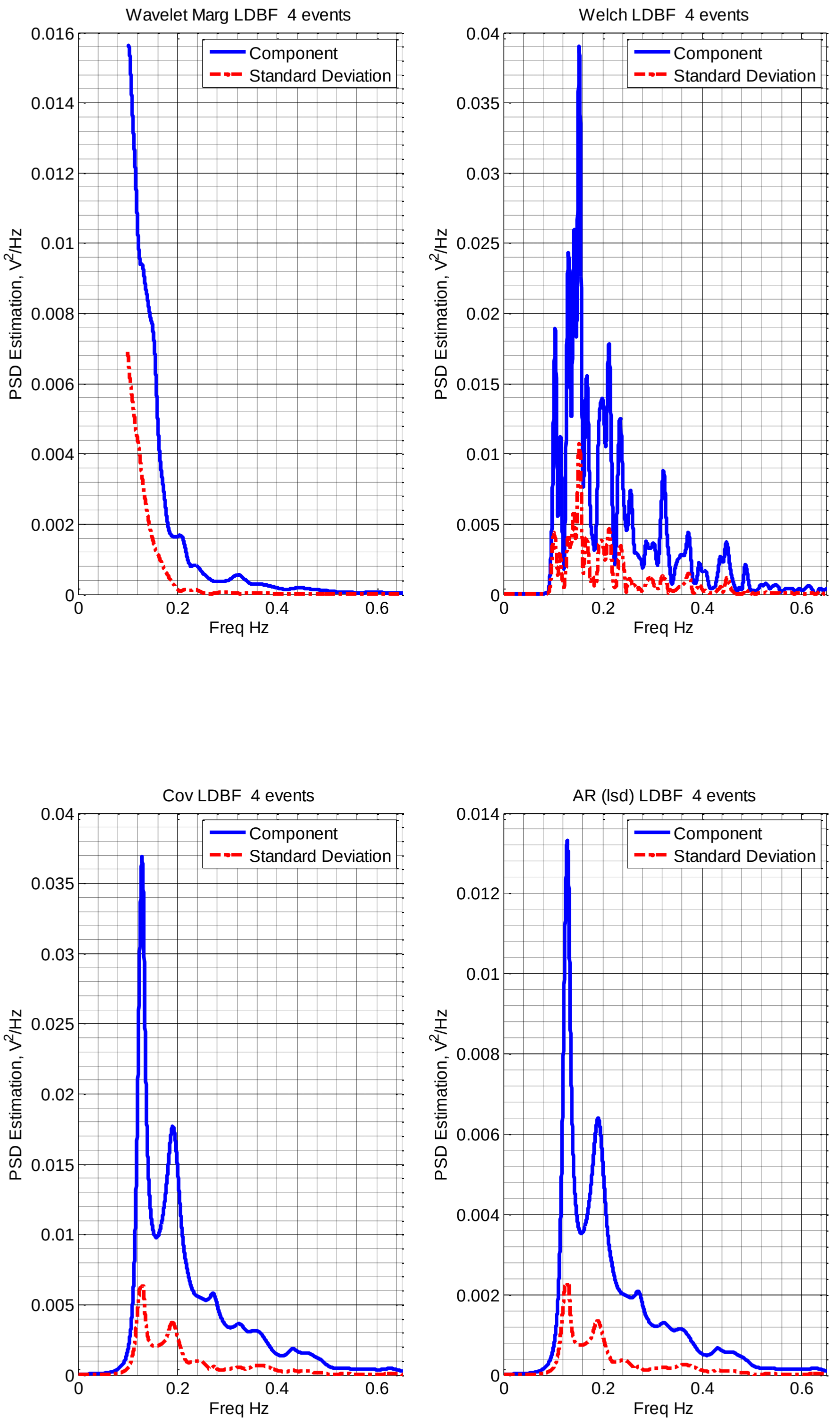

Figure 7.20 - Averaged PSD of 4 events labelled as LDBF waves with the following methods: Wavelet marginal (top, left), Welch (top. rigth), Covariance (bottom, left) and Least Squares (bottom, right). Standart deviation for each PSD average (red dotted line)

Chapter 8

Conclusions and Future Work

After the results obtained in the preceding chapter, some conclusions were drawn, which can be found in this chapter as well as principal achievements and future work.

8.1 Conclusions

A component database was constructed with 288 events:

- Alvarez waves
- Contractions
- Early and Late Labor Contractions
- Fetal Movements
- LDBF waves
- Fetal Hiccups
- Basal Uterine Activity

The database not only has the separated components but also its time and frequency characterization.

The tools that most contributed for event identification were the following:

- **Bipolar configuration** – The monopolar configuration had too much common mode noise, therefore it was difficult to select an event as sometimes it was hard to known were the event started and ended. Selecting the bipolar configuration seemed to be a better choice as there was significant reduction on signal artifacts, despite the risk of losing some components with the common rejection mode of the bipolar configuration. This risk was reduced with the distance between electrodes set as wide as possible. This has been addressed in chapter 3.

- **The Scalogram** - Shows the energy distribution along time and frequency. Also, it is possible to see the changes of frequency with time. It was crucial for event characterization as each event had a distinct behavior in the time-frequency domain. However, there was an issue with the Scalogram and its color code scheme since it depended on EHG signal itself, i.e., the Scalogram maximum was attributed the red color (more energetic) and minimum to the blue color (less energetic). Nevertheless, each signal has a different maximum which means that the same tone of red in two different representations does not correspond to the same energy. Several methodologies can be implemented to solve this normalization problem. In this work, as has been mentioned in chapter 6, section 6.6, the maximum and minimum color were assigned to the Time-frequency values of 0 and 0.05 mW, which were found as average energy bounds for the typical EHG signals of the used database. Other options could be used in a future implementation. The Scalogram's ability to represent energy distribution along the time axis was also used to check out the existence of one of the most significant artifacts: maternal respiration induced signal. This interference overlaps with the interest frequency band, and despite having been greatly reduced by the bipolar electrode arrangement, may be present showing a consistent energy trace. The channels showing this behavior, even after the bipolar montage, were discarded for analysis.

- **Spectral Analysis** - Provides the distribution of power over frequency. As such, the same events have similar spectra, which contributed to the differentiation between them. However similar spectra for different events were also found. In these cases the Scalogram was always a unique feature for differentiation, despite being a more complex representation that requires some training to be correctly interpreted.

- **Wavelet Time Marginal** - Was plotted with the EHG signal. Since it detects the changes of the EHG energy along time, it was used for detecting events. To reduce component selection subjectivity the time onset/offset was chosen between local minima of the Wavelet time marginal. This feature proved to be quite useful and assertive.

- **Tocogram -** Generally, the events present on the EHG were found in the TOCO as well. As such, and after synchronizing the TOCO with the EHG, it was easier to label the components. However, in many cases the events found in the EHG did not match any feature in the corresponding TOCO, which is an indication that the EHG better represents uterine activity.

- **Subject's Information** - provided in the Iceland Database and was very helpful, not only the annotations (contractions, fetus motions, movements) but the information regarding the gestational age at recording and delivery, to distinguish between contractions. Also, the comment mentioning the occurrence of fetal hiccups which otherwise would have been characterized as an artifact.

Tools with lower contribution in the classification process:

- **Wavelet Packet Decomposition** - Reconstruction in selecting nodes were occasionally used to rapidly inspect EHG signals components in a certain frequency band. However, this tool was primarily implemented for future classification and clustering work.

- **Teager, RMS squared** - These energy estimators were also providing information for the classification. They provided a different view on the EHG energy distribution likewise the Wavelet time marginal. Code has been developed for this powerful estimator.

- **CR and PAPR** – These features proved to be quite a noisy representation of the signal, due to the reasons mentioned in chapter 5, section 5.7. Variations to the implementation method should be done in future work.

- **LSD and PS -** Given the multicomponent and relatively narrow band of the selected components, the LS was the feature generically used, along with the PSD where one could observe the respective cumsum's. For the sake of future work and data-base completeness the LSD and PS estimates were also included.

All the tools above mentioned made possible the event characterization into the following categories:

- **Alvarez Waves**

This event was found on the records very close to labor and on labor records, which is not surprising as according to the literature [45] Alvarez waves may lead to the development of labor contractions, and thus labor, being a problem before the 37 weeks of gestation (preterm labor).

In the time domain, Alvarez waves are a train of bursts (generally more than three), very close to each other, with small amplitude.

Both spectral and time frequency representations had energy distribution among the lower frequencies and higher frequencies with a 'gap' in between, in which there was a decrease of energy.

- **Contractions**

Electrical bursts with higher duration and generally more amplitude in comparison with Alvarez waves.

The contractions were classified in the event database according to gestational week: Contractions (before 36 weeks), Early Labor Contractions (after 36 weeks) and Late Labor Contractions (very close to delivery time). However, all the contractions detected on the records, regardless of its gestational age, appeared to present one of the following two behaviors in the frequency domain: a narrow frequency band with only the lower frequencies or a more wide frequency band that ranges from lower to higher frequencies. Nevertheless, on average it was found that the frequency peaks shift to the higher frequencies as the pregnancy progresses. which is in agreement with the literature [22][117].

Contractions classification has posed some challenges which lead to the scorer´s decisions might have not been the most appropriate in light of the results obtained. The scorer used the gestational age as a classification method, which was probably not a good idea. A better option would have been to create two or three subclasses according to time and frequency characteristics.

Among the contractions found in the records before 36 weeks of gestation, the ones that did not cause any cervical effacement or dilatation are Braxton-Hicks. However, this information was not provided, therefore there is no event labeled as Braxton-Hicks in the database, in this step. As such, an unsupervised clustering technique should be applied to detect the Braxton-Hicks class, or even if it is possible to separate the contractions according to the gestational week, which is beyond the scope of this work.

- **Fetal movements**

This component has a very small duration and with energy distribution among the lower frequencies.

- **LDBF waves**

This event was found on the TOCO's. In the EHG it is a contraction burst with increase duration. It distributes its energy among the lower frequencies. It is a rare event that indicates uterine hypertonia.

- **Fetal Hiccups**

Only one event was labeled as fetal hiccups in the event database. It decreases in frequency throughout time (characteristic only seen on the Scalogram). The energy distribution is among the lower frequencies.

Finally, the database has only 288 components, which is due to the time invested in the development of the relevant software tools as well as the limited amount of time available by the physicians, who made the annotation on the TOCO's. However, at this stage know-how has been gathered in order to make the TOCO's annotations in a more autonomous way.

8.2 Principal achievements

- A software tool for the spectral estimation using parametric and nonparametric methods has been developed for the EHG component spectral estimation. Being the EHG a non-deterministic signal any spectral description is just another estimation. It is not clear which method produces the best results. In addition, the Wavelet frequency marginal, also referred as Wavelet spectrum was obtained. This work clearly demonstrates that the usual approach towards EHG signal processing; through the definition of frequency bands is a limited method, since it has been widely observed that EHG components with the same frequency band may have quite different spectra. This is a trait stemming from something that is generically overlooked in the literature: the eminent multicomponent nature of these signals. Defining a bandwidth for a multicomponent signal is reductive. The classical 3dB (half power) criteria is not adequate. So, all the spectra should be taken into account, and there was an effort to understand the EHG components spectral components. It has been found that the Wavelet frequency marginal is a smoother spectral representation that maps the signal better in the lower frequency band. The disadvantage is the inter-component variability (higher standard deviation) in the low band. Other problem of this representation is that the total energy rule may not be met [118]. There is a tradeoff between spectral resolution and this late feature. The Welch estimate (often used in EHG signal processing) revealed to have good detection abilities (sharp peaks) but with too many peaks, the so called "nervous" representation. The smoothing effect of a possible sliding window could be used, if the components would not be generically short in sample number. The parametric models showed to perform better than the others for short duration components such as the fetal movements. The Scalogram proved to be the best tool for the event classification. These components are highly non stationary. So spectral analysis by itself is always limited.

- There is only one research group that has done work using the EHG components [17][18][19][20][21] instead of the all signal. However, the respective database was not release for the public domain. Other research groups work with the full records which may contain different EHG components, mostly under the assumption that detecting individual events is a difficult and unpredictable task. So, in that respect this work has a novelty component about it. The available time for this thesis, whose work consisted of software development for spectral classification and, expert classification- did only allow for the classification of only 288 events in the Iceland data-base. Ideally all the data-base should be catalogued, a time consuming task but made possible using the know-how acquired in this work.

- The most abundant EHG component is the fetal movement (FM). Throughout the classification process an intricate relationship between the FM and the contractions (contractions, LLC or ELC) was patent. FM seemed to trigger uterine contractions and vice-versa, sometimes with seemingly possible FM occurring during contractions. This cause-effect relationship is not yet fully understood. The provided spectral and time-frequency tools are the correct settings for this research area, along with the expert classification know-how.

- Expert classification for golden standards establishment obviously requires personnel trained for this skill. This has been done in EEG based sleep classification as well as ECG human readings. As for the EHG components are concerned, worldwide few experts are identified. This re-enforces the need for automated detector algorithms, which, in turn should be tested against the human classification golden standards. This “catch-22” situation is still patent in the EHG case. In this work enough know-how was gathered to catalogue the remaining of the Iceland data-base, and this is future work.

8.3 Future Work

- Once a database of considerable dimension has been established it is suggested as future work to perform unsupervised clustering for class definition using the following methodologies:

    - Linkage using frequency peaks.
    - Mahalanobis and Itakura-Saito Spectral distances are suggested, as they have provided interesting results in sleep classification [112][119] and voice recognition [120].
    - Linkage using the EHG component Scalograms (2D data) should be used for distance evaluation, which puts a challenge: the size of the matrices is variable. This method has been used for classifying earthquake, mining and nuclear test

vibration data [121]. This is a promising technique since the Scalograms are unique representations.

- Once this work has been achieved unsupervised EHG component detection methods such as Neural Networks should be used, thus reducing the dependence on the expert classification and dramatically improving classification speed-up. This will be a decisive step for the Pre-Term risk evaluation based on the EHG.

- Study of the EHG components and how they relate to each other and propagate:

    - Relationship between the fetal movements and the contractions.
    - Influence of the Alvarez waves in pre-term birth.
    - Propagation Studies based on the EHG components rather than on the generic phase signal.

References

[1] M. Hassan, B. Karlsson, and C. Marque, “Interactions between Uterine EMG at Different Sites Investigated Using Wavelet Analysis : Comparison of Pregnancy and Labor Contractions,” *EURASIP J. Adv. Signal Process.*, vol. 2010, no. 1, p. 9, 2010.

[2] R. E. Garfield, H. Maul, W. Maner, C. Fittkow, G. Olson, L. Shi, and G. R. Saade, “Uterine Electromyography and Light-Induced Fluorescence in the Management of Term and Preterm Labor,” *J. Soc. Gynecol. Investig.*, vol. 9, no. 5, pp. 265–275, 2002.

[3] D. Devedeux, C. Marque, S. Mansour, and G. Germain, “Current Development Uterine electromyography: A critical review,” pp. 1636–1653, 1993.

[4] D. Alamedine, M. Khalil, and C. Marque, “Comparison of Different EHG Feature Selection Methods for the Detection of Preterm Labor,” *Comput. Math. Methods Med.*, vol. 2013, p. 9, 2013.

[5] M. S. Jóhannsdóttir, “The Effect of Different Electrode Design on the Electrohysterogram Signal The Effect of Different Electrode Design on the Electrohysterogram Signal.”

[6] “Nascimentos Pré-Termo.” [Online]. Available: http://impns.dgs.pt/nascer-com-saude/nascimentos-pre-termo. [Accessed: 19-Sep-2015].

[7] R. WE, M. JC, H. C, and W. WL, “The incidence of preterm labor and specific risk factors,” *Obstet. Gynecol.*, vol. 76, p. 85S–89S, 1990.

[8] E. Roberts, G. Perry, F. Washburne, J. C. Morrison, and W. N. Iii, “The irritable uterus : A risk factor for preterm birth ?”

[9] M. HASSAN, “Analysis of the propagation of uterine electrical activity applied to predict preterm labor,” Reykjavik University, 2011.

[10] K. Horoba, J. Jezewski, J. Wrobel, and S. Graczyk, “Algorithm for Detection of Uterine Contractions from Electrohysterogram,” in *Proceedings of the 23rd Annual EMBS International Conference*, 2001, p. 3.

[11] J. Alberola-Rubio, G. Prats-Boluda, Y. Ye-Lin, J. Valero, a. Perales, and J. Garcia-Casado, “Comparison of non-invasive electrohysterographic recording techniques for monitoring uterine dynamics,” *Med. Eng. Phys.*, vol. 35, no. 12, pp. 1736–1743, 2013.

[12] K. Horoba, A. Matonia, J. Jezewski, T. Kupka, and A. Gacek, “ANALYSIS OF UTERINE CONTRACTION ACTIVITY USING,” 2006.

[13] H. ALVAREZ and R. CALDEYRO, “Contractility of the human uterus recorded by new methods.,” *Surg. Gynecol. Obstet.*, vol. 91, no. 1, p. 13, 1950.

[14] A. Csapo and J. Sauvage, “The evolution of uterine activity during human pregnancy.,” *Acta Obstet. Gynecol. Scand.*, vol. 47, pp. 181–212, 1968.

[15] O. Bode, “Das elektrohysterogramm,” *Arch. Gyndk*, vol. 28, pp. 123–128, 1931.

[16] S. D. Larks, “THE HUMAN ELECTROHYSTEROGRAM: WAVE FORMS AND IMPLICATIONS.,” in *Proceedings of the National Academy of Sciences of the United States of America*, 1958, vol. 44, no. 8, pp. 820–824.

[17] C. Marque, J. Gondry, J. Rossi, N. Baaklini, and J. Duchene, “Surveillance des grossesses à risque par électromyographie utérine,” *RBM - Rev. Eur. Technol. Biomed.*, vol. 17, no. 1, pp. 25–31, 1995.

[18] C. Marque, H. Leman, M. L. Voisine, J. Gondry, and P. Naepels, “Traitement de l’électromyogramme utérin pour la caractérisation des contractions pendant la grossesse,” *RBM-News*, vol. 21, no. 9, pp. 200–211, 1999.

[19] M. Khalil, J. Duchêne, and C. Marque, “Uterine EMG processing : dynamic detection associated with multiscale classification of events,” in *Proceedings of the First Joint BMES/EMBS Conference*, 1999, p. 1.

[20] M. Khalil and J. Duchêne, “Uterine EMG analysis: a dynamic approach for change detection and classification.,” *IEEE Trans. Biomed. Eng.*, vol. 47, no. 6, pp. 748–756, 2000.

[21] M. Khalil, Marwa Chendeb, M. Diab, C. Marque, and J. Duchêne, “Uterine EMG Analysis: Time-Frequency Based Techniques for Preterm Birth Detection,” in *Advanced Biosignal Processing*, 2009, pp. 245–266.

[22] M. Chendeb, M. Khalil, D. Hewson, and J. Duchêne, “Classification of non stationary signals using multiscale decomposition,” *J. Biomed. Sci. Eng.*, vol. 3, pp. 193–199, 2010.

[23] C. Rabotti, “Characterization of uterine activity by electrohysterography,” Technishe Universiteit Eindhoen, 2010.

[24] “Anatomy and physiology of the uterus - Canadian Cancer Society.” [Online]. Available: http://www.cancer.ca/en/cancer-information/cancer-type/uterine/anatomy-and-physiology/?region=bc. [Accessed: 02-Mar-2015].

[25] H. Maul, W. L. Maner, G. R. Saade, and R. E. Garfield, “The physiology of uterin contractions,” *Clin Perinatol*, vol. 30, pp. 665–676, 2003.

[26] S. Martens, “Extraction of the fetal ECG and the uterine contraction EMG from simulated abdominal recordings by principal component analysis,” Technische Universiteit Eindhoven, 2003.

[27] “Pregnancy.” [Online]. Available: http://medical-dictionary.thefreedictionary.com/Pregnancy. [Accessed: 03-Mar-2015].

[28] J. XU, “Dynamics and synchronization in biological excitable media,” Université de Lyon, 2012.

[29] “Uterine Muscle.” [Online]. Available: https://stratog.rcog.org.uk/tutorial/physiology-and-biochemistry/uterine-muscle-4877. [Accessed: 02-Mar-2015].

[30] P. S. La Rosa, H. Eswaran, H. Preissl, and A. Nehorai, “Multiscale forward electromagnetic model of uterine contractions during pregnancy.,” *BMC Med. Phys.*, vol. 12, no. 4, p. 16, 2012.

[31] D. Devedeux, C. Marque, S. Mansour, G. Germain, and J. Duchêne, “Uterine electromyography: a critical review.,” *Am. J. Obstet. Gynecol.*, vol. 169, no. 6, pp. 1636–1653, 1993.

[32] T. Chard and J. G. Grudzinskas, *The Uterus*. Cambridge University Press, 1994.

[33] “Fundal Dominance.” [Online]. Available: https://stratog.rcog.org.uk/tutorial/physiology-and-biochemistry/fundal-dominance-4884. [Accessed: 02-Mar-2015].

[34] “Maternal Hormones.” [Online]. Available: https://stratog.rcog.org.uk/tutorial/physiology-and-biochemistry/maternal-hormones---progesterone-4880. [Accessed: 02-Mar-2015].

[35] “Estrogen.” [Online]. Available: https://stratog.rcog.org.uk/tutorial/physiology-and-biochemistry/estrogen-4881. [Accessed: 02-Mar-2015].

[36] R. E. Garfield and W. L. Maner, “Physiology and electrical activity of uterine contractions,” *Semin. Cell Dev. Biol.*, vol. 18, no. 3, pp. 289–295, 2007.

[37] “Cervical Effacement.” [Online]. Available: http://www.webmd.com/baby/cervical-effacement. [Accessed: 02-Mar-2015].

[38] R. E. Garfield, G. Saade, C. Buhimschi, I. Buhimschi, L. Shi, S. Q. Shi, and K. Chwalisz, “Control and assessment of the uterus and cervix during pregnancy and labour,” *Hum. Reprod. Update*, vol. 4, no. 5, pp. 673–695, 1998.

[39] A. T. Evans, *Manual of Obstetrics*. Lippincott Williams & Wilkins, 2007.

[40] “Pregnancy.” [Online]. Available: https://en.wikipedia.org/wiki/Pregnancy. [Accessed: 13-Sep-2005].

[41] “A Guide to Pregnancy Complications.” [Online]. Available: http://health.howstuffworks.com/pregnancy-and-parenting/pregnancy/complications/a-guide-to-pregnancy-complications-ga.htm. [Accessed: 19-Aug-2015].

[42] “Miscarriage.” [Online]. Available: https://en.wikipedia.org/wiki/Miscarriage. [Accessed: 20-Sep-2015].

[43] “Antepartum Haemorrhage.” [Online]. Available: http://patient.info/doctor/antepartum-haemorrhage. [Accessed: 20-Sep-2015].

[44] L. Lange, A. Vaeggemose, P. Kidmose, E. Mikkelsen, N. Uldbjerg, and P. Johansen, “Velocity and Directionality of the Electrohysterographic Signal Propagation,” *PLoS One*, vol. 9, no. 1, p. 6, 2014.

[45] F. Lam and P. Gill, “Inhibition of Preterm Labor and Subcutaneous Terbutaline Therapy,” in *Multiple Pregnancy: Epidemiology, Gestation, and Perinatal Outcome*, 2005, pp. 601–619.

[46] R. B. Newman, P. J. Gill, S. Campion, and M. Katz, “Antepartum Ambulatory Tocodynamometry: The Significance of Low-Amplitude, High-Frequency Contractions,” *Obstetrics and gynecology*, vol. 70, no. 5. pp. 701–705, 1987.

[47] M. Chendeb, “Détection et classification des signaux non stationnaires par utilisation des ondelettes. Application aux signaux électromyographiques utérins,” Universite de Technologie de Troyes, 2006.

[48] J. Nagel and M. Schaldach, “The non-invasive assessment of uterine activity,” in *Non-Invasive measurements:2*, 1983, pp. 103–129.

[49] Á. Alexandersson, “Conceiving , compiling , publishing and exploiting the ‘ Icelandic 16-electrode EHG database ,’” Reykjavik University, 2015.

[50] H. Maul, W. L. Maner, G. Olson, G. R. Saade, and R. E. Garfield, “Non-invasive transabdominal uterine electromyography correlates with the strength of intrauterine pressure and is predictive of labor and delivery.,” *J. Matern. Neonatal Med.*, vol. 15, pp. 297–301, 2004.

[51] R. E. Garfield and W. L. Maner, “Biophysical methods of prediction and prevention of preterm labor: uterine electromyography and cervical light-induced fluorescence - new obstretrical diagnostic techniques,” in *Preterm Birth*, 2007, pp. 131–144.

[52] D. Schlembach, W. L. Maner, R. E. Garfield, and H. Maul, “Monitoring the progress of pregnancy and labor using electromyography,” *Eur. J. Obstet. Gynecol. Reprod. Biol.*, vol. 144, pp. S33–S39, 2009.

[53] J. Alberola-Rubio, J. Garcia-Casado, Y. Ye-Lin, G. Prats-Boluda, and A. Perales, “Recording of Electrohysterogram Laplacian Potential,” in *Proceedings of the Annual International Conference of the IEEE Engineering in Medicine and Biology Society, EMBS*, 2011, pp. 2510–2513.

[54] A. Matonia, K. Horoba, J. Jezewski, and T. Kupka, “Monitoring of contraction activity of uterine muscle by the use of abdominal electrohysterography,” *Acta Bioeng. Biomech.*, vol. 8, no. 2, p. 9, 2006.

[55] Y. Ye-Lin, J. Garcia-Casado, G. Prats-Boluda, J. Alberola-Rubio, and A. Perales, “Automatic Identification of Motion Artifacts in EHG Recording for Robust Analysis of Uterine Contractions,” *Comput. Math. Methods Med.*, vol. 2014, p. 11, 2014.

[56] A. Alexandersson, T. Steingrimsdottir, J. Terrien, C. Marque, and B. Karlsson, “The Icelandic 16-electrode electrohysterogram database,” *Sci. Data*, vol. 2, p. 150017, 2015.

[57] P. Aelen, “Determination of the Intra Uterine Pressure with electrodes on the abdomen.” p. 30, 2005.

[58] S. Snowden, N. a Simpson, and J. J. Walker, “A digital system for recording the electrical activity of the uterus.,” *Physiol. Meas.*, vol. 22, no. 4, pp. 673–9, 2001.

[59] J. Jezewski, K. Horoba, A. Matonia, and J. Wrobel, “Quantitative analysis of contraction patterns in electrical activity signal of pregnant uterus as an alternative to mechanical approach.,” *Physiol. Meas.*, vol. 26, no. 5, pp. 753–67, 2005.

[60] J. Vrhovec and A. M. Lebar, “An Uterine Electromyographic Activity as a Measure of Labor Progression,” in *Applications of EMG in Clinical and Sports Medicine*, InTech, 2012, pp. 243–268.

[61] C. Rabotti, M. Mischi, J. O. E. H. van Laar, G. S. Oei, and J. W. M. Bergmans, “Inter-electrode delay estimators for electrohysterographic propagation analysis.,” *Physiol. Meas.*, vol. 30, no. 8, pp. 745–761, 2009.

[62] R. E. Garfield, W. L. Maner, L. B. MacKay, D. Schlembach, and G. R. Saade, “Comparing uterine electromyography activity of antepartum patients versus term labor patients,” *Am. J. Obstet. Gynecol.*, vol. 193, no. 1, pp. 23–29, 2005.

[63] M. Lucovnik, W. L. Maner, L. R. Chambliss, R. Blumrick, J. Balducci, Z. Novak-Antolic, and R. E. Garfield, “Noninvasive uterine electromyography for prediction of preterm delivery,” *Am. J. Obstet. Gynecol.*, vol. 204, no. 3, pp. 228.e1–228.e10, 2011.

[64] W. L. Maner, R. E. Garfield, H. Maul, G. Olson, and G. Saade, “Predicting Term and Preterm Delivery With Transabdominal Uterine Electromyography,” *Am. Coll. Obstet. Gynecol.*, vol. 101, no. 6, pp. 1254–1260, 2003.

[65] M. Lucovnik, R. J. Kuon, L. R. Chambliss, W. L. Maner, S. Q. Shi, L. Shi, J. Balducci, and R. E. Garfield, “Use of uterine electromyography to diagnose term and preterm labor,” *Acta Obstet. Gynecol. Scand.*, vol. 90, no. 2, pp. 150–157, 2011.

[66] W. L. Maner and R. E. Garfield, “Identification of Human Term and Preterm Labor using Artificial Neural Networks on Uterine Electromyography Data,” *Ann. Biomed. Eng.*, vol. 35, no. 3, pp. 465–473, 2007.

[67] B. Vasak, E. M. Graatsma, E. Hekman-Drost, M. J. Eijkemans, J. H. Schagen Van Leeuwen, G. H. Visser, and B. C. Jacod, “Uterine electromyography for identification of first-stage labor arrest in term nulliparous women with spontaneous onset of labor,” *Am. J. Obstet. Gynecol.*, vol. 209, no. 3, pp. 232.e1–232.e8, 2013.

[68] E. Mikkelsen, P. Johansen, A. Fuglsang-Frederiksen, and N. Uldbjerg, “Electrohysterography of labor contractions: propagation velocity and direction,” *Acta Obstet. Gynecol. Scand.*, vol. 92, no. 9, pp. 1070–1078, 2013.

[69] C. Rabotti and M. Mischi, “Two-dimensional estimation of the electrohysterographic conduction velocity,” *IEEE Trans. Biomed. Eng.*, vol. 57, no. 9, pp. 4262–4265, 2010.

[70] M. J. Rooijakkers, C. Rabotti, S. G. Oei, R. M. Aarts, and M. Mischi, “Low-complexity intrauterine pressure estimation using the Teager energy operator on electrohysterographic recordings.,” *Physiol. Meas.*, vol. 35, no. 7, pp. 1215–28, 2014.

[71] M. Mischi, C. Rabotti, L. J. Vosters, S. G. Oei, and J. M. Bergmans, “Electrohysterographic conduction velocity estimation.,” in *31st Annual International Conference of the IEEE EMBS*, 2009, vol. 2009, pp. 6934–6937.

[72] P. Fergus, P. Cheung, A. Hussain, D. Al-Jumeily, C. Dobbins, and S. Iram, “Prediction of Preterm Deliveries from EHG Signals Using Machine Learning,” *PLoS One*, vol. 8, no. 10, p. 16, 2013.

[73] M. P. G. C. Vinken, C. Rabotti, M. Mischi, J. O. E. H. van Laar, and S. G. Oei, “Nifedipine-Induced Changes in the Electrohysterogram of Preterm Contractions: Feasibility in Clinical Practice.,” *Obstet. Gynecol. Int.*, vol. 2010, p. 8, 2010.

[74] S. Somarajan, N. Muszynski, C. Obioha, W. Richards, and L. Bradshaw, “Biomagnetic and bioelectric of gastric slow wave activity in normal human subjects - a correlation study,” *Physiol. Meas.*, vol. 33, no. 7, pp. 1171–1179, 2012.

[75] J. C. Erickson, C. Obioha, A. Goodale, L. A. Bradshaw, and W. O. Richards, “Detection of Small Bowel Slow Wave Frequencies from Noninvasive Biomagnetic Measurements,” *IEEE Trans. Biomed. Eng.*, vol. 56, no. 9, pp. 2181–2189, 2009.

[76] H. Krammer and M. V. Singer, *Neurogastroenterology - From the Basics to the Clinics*. Springer Science & Business Media, 2000.

[77] T. Koch, *Colonic Diseases*. Springer Science & Business Media, 2003.

[78] E. Marani and W. F. R. M. Koch, “Smooth Muscle Electromyography of Bladder and Uterus,” in *The Pelvis: Structure, Gender and Society*, Springer Science & Business Media, 2014, p. 558.

[79] A. M. Holschneider and P. Puri, *Hirschsprung’s Disease and Allied Disorders*, 3rd ed. Springer Science & Business Media, 2007.

[80] Z. Xu and S. Xiao, “Digital filter design for peak detection of surface EMG.,” *J. Electromyogr. Kinesiol.*, vol. 10, no. 4, pp. 275–281, 2000.

[81] A. Moreno-Muñoz, *Power Quality: Mitigation Technologies in a Distributed Environment*. Springer, 2007.

[82] J. D. Bronzino, *Medical Devices and Systems*, 3rd ed. Taylor & Francis Group, 2006.

[83] M. Sandsten, “Time-Frequency Analysis of Non-Stationary Processes.” p. 89, 2013.

[84] F. Auger, P. Flandrin, P. Gonçalvès, and O. Lemoine, “Time-Frequency Toolbox For Use with MATLAB.” p. 150, 1996.

[85] R. X. Gao and R. Yan, “From Fourier Transform to Wavelet Transform: A Historical Perspective,” in *Wavelets :Theory and Applications for Manufacturing*, Springer, 2011, pp. 17–32.

[86] V. K. V.R and A. B. P, “Features of Wavelet Packet Decomposition and Discrete Wavelet Transform for Malayalam Speech Recognition,” *Int. J.*, vol. 1, no. 2, pp. 93–96, 2009.

[87] B. Nascimento, “MicroECG: An Integrated Platform For The Cardiac Arrythmia Detection And Characterization,” Faculdade de Ciências e Tecnologia da Universidade Nova de Lisboa, 2009.

[88] B. Manresa, “Lecture 2 The Wigner-Ville Distribution.” p. 40, 2011.

[89] M. Sandsten, “Time-Frequency Analysis.” p. 12, 2013.

[90] D. Marques, “Análise Espectral com Wavelets do ECoG em Crises Epilépticas,” Faculdade de Ciências e Tecnologia da Universidade Nova de Lisboa, 2012.

[91] P. Stoica and R. Moses, *Introduction to Spectral Analysis*. Prentice-Hall Inc., 1997.

[92] J. L. Semmlow, *Biosignal and Biomedical Image Processing MATLAB-Based Applications*. Marcel Dekker Inc., 2004.

[93] G. Heinzel, A. Rüdiger, R. Schilling, and T. Hannover, "Spectrum and spectral density estimation by the Discrete Fourier transform (DFT), including a comprehensive list of window functions and some new flat-top." p. 84, 2002.

[94] A. Shradhanjali, S. Chowdhury, and N. Kumar, "Power Spectral Density Estimation of EMG Signals Using Parametric and Non-Parametric Approach," *J. Eng. Technol. Innov.*, vol. 2, no. 4, pp. 111–117, 2013.

[95] G. V Tcheslavski, "Lecture 09 : Spectrum estimation – parametric." p. 20, 2009.

[96] F. Castanié, *Spectral Analysis Parametric and Non-Parametric Digital Methods*, 1st ed. John Wiley & Sons, 2011.

[97] M. Akay, *Biomedical Signal Processing*. Academic Press, 1994.

[98] "Matlab help." [Online]. Available: http://www.mathworks.com/help/signal/ug/parametric-methods.html?searchHighlight=Minimizes the forward and backward prediction errors in the least squares sense%2C with the AR coefficients constrained to satisfy the L-D recursion. [Accessed: 07-May-2015].

[99] G. Hearn and M. Andrew, *Spectral Analysis in Engineering Concepts and Cases*. Elsevier Inc, 2004.

[100] W. Emery and R. Thomson, *Data Analysis Methods in Physical Oceanography*, Second. Elsevier.

[101] L. Dactron, "Application Note: Understanding FFT Windows." p. 7, 2003.

[102] "Bandwidth (signal processing)." [Online]. Available: https://en.wikipedia.org/wiki/Bandwidth_(signal_processing). [Accessed: 05-Sep-2015].

[103] "Bandwidth." [Online]. Available: http://www.sengpielaudio.com/calculator-cutoffFrequencies.htm. [Accessed: 05-Sep-2015].

[104] "Occupied Bandwidth (obw)." [Online]. Available: http://www.mathworks.com/help/signal/ref/obw.html. [Accessed: 05-Sep-2015].

[105] F. Auger, P. Flandrin, P. Gonçalvès, and O. Lemoine, *Time-Frequency Toolbox For Use with MATLAB Reference Guide*. 1996.

[106] "Energy vs Power." [Online]. Available: http://cnx.org/contents/22e7ef31-128f-4119-85a2-ac5ae6e668e0@11/Signal_Energy_vs._Signal_Power. [Accessed: 06-Jul-2015].

[107] D. Sundararajan, *A Practical Approach To Signals and Systems*. 2008.

[108] M. J. Rooijakkers, C. Rabotti, S. G. Oei, R. M. Aarts, and M. Mischi, "Low-complexity intrauterine pressure monitoring by Teager energy estimation," in *International Conference of the IEEE EMBS*, 2013, pp. 7424–7427.

[109] “Crest Factor.” [Online]. Available: https://en.wikipedia.org/wiki/Crest_factor. [Accessed: 20-Jul-2015].

[110] C. DE BOOR, *A Pratical Guide to Splines*. New York: Springer-Verlag, 1978.

[111] “Matworks: NFFT.” [Online]. Available: http://www.mathworks.com/help/matlab/ref/nextpow2.html. [Accessed: 21-Aug-2015].

[112] N. Fernandes, “SleepLab V.2.o: Plataforma Integrada de Teste de Algoritmos para Classificação Não Supervisionada do Sono,” FCT-UNL, 2011.

[113] M. Murray, *Antepartal and intrapartal fetal monitoring*, 3rd ed. Springer Publishing Company, 2006.

[114] B. Moslem, M. Hassan, M. Khalil, C. Marque, and M. O. Diab, “Monitoring the progress of pregnancy and labor using electromyography,” in *Proceedings of 2009 International Symposium On Bioelectronics & Bioinformatics*, 2009, vol. 144, no. SUPPL 1, pp. 160–163.

[115] B. Moslem, M. Khalil, C. Marque, and M. O. Diab, “Complexity analysis of the uterine electromyography.,” *Conf. Proc. IEEE Eng. Med. Biol. Soc.*, vol. 2010, pp. 2802–2805, 2010.

[116] B. Moslem, M. Khalil, C. Marque, and M. O. Diab, “Energy Distribution Analysis of Uterine Electromyography Signals,” *J. Med. Biol. Eng.*, vol. 30, no. 6, p. 361, 2010.

[117] C. Buhimschi, M. B. Boyle, and R. E. Garfield, “Electrical Activity of the Human Uterus During Pregnancy as Recorded from the Abdominal Surface,” *Obstet. Gynecol.*, vol. 90, pp. 102–111, 1997.

[118] C. Torrence and G. P. Compo, “A Practical Guide to Wavelet Analysis,” *Bull. Am. Meterological Soc.*, vol. 79, no. 1, pp. 61–78, 1998.

[119] E. Cardoso, A. Batista, R. Rodrigues, M. Ortigueira, C. Bárbara, C. Martinho, and R. Rato, “A contribution for the automatic sleep classification based on the Itakura-Saito spectral distance,” *IFIP Adv. Inf. Commun. Technol.*, vol. 314, pp. 374–381, 2010.

[120] F. Ebrahimi, M. Mikaili, E. Estrada, and H. Nazeran, “Assessment of Itakura Distance as a valuable feature for computer-aided classification of sleep stages,” in *Conf Proc IEEE Eng Med Biol Soc.*, 2007, pp. 3300–3.

[121] R. H. Shumway, “Time-frequency clustering and discriminant analysis,” *Stat. Probab. Lett.*, vol. 63, no. 3, pp. 307–314, 2003.